UNDERSTANDING FATIGUE THROUGH HIGH ENERGY X-RAY DIFFRACTION STUDIES

A Dissertation

Presented to the Faculty of the Graduate School

of Cornell University

in Partial Fulfillment of the Requirements for the Degree of

Doctor of Philosophy

by

Mark Obstalecki

August 2017

UNDERSTANDING FATIGUE THROUGH HIGH ENERGY X-RAY DIFFRACTION STUDIES

Mark Obstalecki, Ph.D.

Cornell University 2017

Understanding fatigue crack initiation in ductile metals remains a significant challenge for engineers despite decades of research. In this work, high energy x-ray diffraction techniques and analysis methods are implemented to nondestructively monitor structural changes within grains of polycrystals during fatigue loading conditions. First, experimental results are presented from a fully reversed incremental step test performed on a copper alloy containing precipitates. Crystal plasticity modeling results are compared to the experiments to identify similarities and differences in structural heterogeneity across four target grains. Next, a pure copper sample is examined, and x-ray diffraction-based metrics are developed to characterize the heterogeneity of orientation and strain across each grain. Hundreds of grains within the pure copper and copper alloy samples are compared though these metrics to reveal significant differences in the character of their grain-scale deformation during cycling. Finally, a pure copper sample is tested to a relatively large number of cycles. The experimentally measured heterogeneity metric values for each grain are superimposed onto a three-dimensional grain map to provide insight into the spatial distribution of deformation across the aggregate.

BIOGRAPHICAL SKETCH

Mark Obstalecki was born in 1987, the son of Polish immigrants Jan and Janina Obstalecki. He attended the University of Illinois at Urbana-Champaign and became a first generation college graduate upon completing his Bachelor's degree in Mechanical Engineering. Subsequently he pursued a Master's degrees at the University of Illinois under the guidance of Prof. Armand J. Beaudoin. During his Master's work Mark drank from the synchrotron x-ray diffraction fire hose and decided to pursue a Ph.D. at Cornell under the guidance of Prof. Matthew P. Miller. Mark started collecting coins at a young age; his fascination with numismatics continues to this day.

To all students struggling through their doctoral degree programs.

ACKNOWLEDGEMENTS

I would like to thank my committee for shaping this work into its current form. A special thank you is extended to my chairman, Prof. Matthew P. Miller. Matt has molded me both as a researcher and an individual over the last few years. I wouldn't be here today without him. Thank you also to Prof. Paul R. Dawson for serving as a second adviser and providing valuable technical insights into crystal plasticity modeling. Committee members Prof. S. Phoenix and Prof. J. Williams deserve special recognition for providing technical support throughout my time at Cornell.

Special thanks goes out to my colleague and friend, Dr. Darren Pagan, who spent many hours and nights supporting beamtimes. Thank you also to current and former students and post-docs of DPLab: Dr. Jun-Sang Park, Dr Su-Leen Wong, Dr. Euan Wielewski, Christopher Budrow, Robert Carson, and Timothy Long. I wish you all the best in your future careers.

The beamline scientists at both APS and CHESS require acknowledgment. I'd like to thank Dr. Ulrich Lienart, Dr. Peter Kenesie, Dr. Darren Dale, and Dr. Peter Ko for taking the time to train me and support my experiments. The entire CHESS staff has been incredibly supportive.

I couldn't have gotten through this period of my life without my extracurricular activities. Thank you to Marc Murphy for usually showed up to lift in the mornings at IHF. I'll never forget our days of cross-fit. Numismatists Tom Krawczyk and Robert Lisk deserve acknowledgment for keeping me distracted with their insights into the nuances of coin collecting. Thank you to the Cornell Running Club for challenging me to stay fit and enabling me to run my first marathon.

Special thank you to Lesley Middleton for her unwavering support. She kept

the household together when I was too busy. Love you!

Finally, I would like to thank my parents for enabling me to reach my current level of academic achievement.

TABLE OF CONTENTS

LIST OF TABLES

LIST OF FIGURES

CHAPTER 1

INTRODUCTION

1.1 Project motivation

Accurately predicting the fatigue life of a component remains a challenging task for engineers. The quantification of fatigue life is still largely driven by empirical equations, which typically lead to the over-designing of structural components to prevent fatigue failure. Generally fatigue life is divided into three stages: fatigue crack nucleation, slow crack growth, and finally rapid crack growth leading to eventual component failure. The crack nucleation stage typically represents the longest portion of a component's fatigue life, but unfortunately the current understanding of the micromechanical processing leading to fatigue crack nucleation is limited. A comprehensive theory capable of predicting fatigue crack initiation in ductile metals has not been formulated after many decades of research.

Previous research has pointed towards the important correlation between heterogeneous deformation and fatigue crack initiation in ductile metals. Much of the early research into fatigue crack initiation focused on persistent slip bands (PSBs) in single crystals aligned for single slip. Researches observed these PSBs on the surface of the single crystals and connected them to plastic slip on the slip system with the highest resolved shear stress [73]. After polishing away these bands, they reappeared after continued mechanical loading. They ”persisted” in the same region, which implied that the material's state was altered in these regions. Research identified these PSBs as precursors to microcracks in single crystals. The observation of extrusions and intrusions where these PSBs meet

the surface of the sample motivated crack initiation theories around the same time [25, 55, 88].

Advances in experimental capabilities are often tied to new understanding of fatigue processes. Research showed that PSBs do not form in all fatigue specimens, thus PSBs do not always serve as precursors to cracks [49]. Post mortem transmission electron microscopy (TEM) enabled researchers to observe dislocations structures and the initiation of microcracks within cyclically deformed materials [5, 6, 32]. In addition to TEM studies, dislocation densities have been estimated through x-ray diffraction line broadening experiments [82]. A large body of work has focused on pure copper which exhibits a propensity to cross slip and form dislocation cells. Observed x-ray diffraction peak asymmetry was explained by differences in the dislocation density between the cell walls and the cell interiors [57, 75]. Just like the observation of PSBs, the observation of dislocation cells and other dislocation structures through TEM and x-ray measurements provided further evidence that deformation is largely heterogeneous at the crystal scale.

Despite the significant advances provided by microscopy techniques during previous decades, they do have limitations in their capabilities. For example, TEM often focuses on small foils extracted from small regions of samples. We currently cannot predict the location where a fatigue crack will form, thus it is difficult to correlate the dislocation structures observed in TEM foils to regions where crack may eventually form. Other techniques, such as Scanning Electron Microscopy (SEM), can probe larger areas, but the technique is limited to the surfaces of samples. Serial sectioning is possible but necessitates sample destruction, thus subsequent mechanical testing is not possible. Another lim-

itation of traditional microscopy is the inability to quantify the stress state of the material. The general inability to quantify grain scale stresses has prevented much of the fundamental work performed on single crystals from translating over to polycrystals, which typically experience multiaxial, spatially nonuniform stress states due to the anisotropic mechanical properties of the individual crystals.

Decades of research has shown us that fatigue crack initiation is inherently a dynamic process. During cyclic plastic loading of a polycrystal, researches have observed the formation of features such as PSBs, formation and evolution of complex dislocation structures, and nonuniform deformation across both individual crystals and the aggregate. This nonuniform deformation at the subcrystal scale is intimately linked with fatigue crack initiation in ductile metals. The ability to dynamically observe these changes in structure at the crystal scale could provide valuable insight into the conditions, which lead to the formation of a crack in a ductile metal.

TEM and SEM can provide us with two-dimensional snapshots of the mechanical state of a material, but high energy x-ray diffraction (HEXD) techniques provide the ability to nondestructively monitor the state of every crystal within a polycrystal *during* deformation. The high energy and high flux nature of synchrotron sources provides sample penetration on the order of millimeters, such that hundreds or even thousands of crystals can be interrogated simultaneously. The so called far-field experimental geometry provides a means of measuring the average orientation and full lattice strain tensor for every grain within the diffraction volume. With the lattice strain tensor, the stress tensor is readily calculated through Hooke's law. Additionally, detailed analysis of deformation-

induced diffraction peak shape changes enables us to quantitatively measure heterogeneity of lattice orientation and lattice plane spacing within each grain. This ability to simultaneously monitor the stress and heterogeneity of the crystal lattice provides an unparalleled ability to investigate the microplasticity processes leading to the formation of a fatigue crack.

Despite the powerful capabilities provided by HEXD techniques, they still only provide grain averaged information. Ideally for a problem focusing on nonuniform deformation at the sub-grain scale, we would ideally like three dimension maps of this deformation. Spatial information within grains is lacking from the experimental data alone, but the results can be coupled with crystal plasticity finite element simulations to provide approximations of the spatial deformation fields. In addition to quantities such as stress and orientation, the model also proves a wealth of knowledge such as the effective plastic deformation rate and slip system activity. These data could be effectively mined beyond the information provided from the experiments alone.

Comparisons of experimental results to simulations can also inform modeling efforts to better capture the deformation behavior of individual crystals within a polycrystal. Further development of these models could eventually create a truly predictive capability for identifying regions where cracks are likely to form.

The synergistic interaction between the high energy x-ray diffraction experiments and the crystal plasticity model is implemented and tested in this work to build a broader understanding of the microplasticity processes which progress during fatigue loading conditions.

1.2 Dissertation outline

This dissertation is comprised of four chapters including the Introduction. Each subsequent chapter presents advances in experimental techniques, data reduction capabilities, modeling efforts, and scientific understanding in a chronological order. Provided below is a brief summary of each chapter to explain the progression of research throughout the project.

1.2.1 Chapter 2

Chapter 2 titled, 'Quantitative analysis of crystal scale deformation heterogeneity during cyclic plasticity using high-energy X-ray diffraction and finite-element simulation,' was published in Acta Materialia in 2014. This journal publication presents the results from the first fully-reversed cyclic experiment performed at a synchrotron light source. A novel compact load frame was designed and built specifically for this experiment. The material chosen for this study, Okegawa Mold Copper (OMC), is a precipitation strengthened copper alloy, which exhibits a much larger yield strength when compared to pure, annealed copper. The sample's high strength provides a larger signal to noise ratio, enabling higher fidelity in the measured lattice strains.

An incremental step test was performed on the sample at the synchrotron. The sample was first deformed at a strain amplitude of 0.3% for three cycles, and then an additional three cycles at 0.5% strain amplitude. X-ray diffraction measurements were performed at the tensile and compressive loop tips of each cycle. A total of four grains were interrogated during this first experiment. Ex-

perimental results revealed a strong compression bias in the azimuthal peak widths for every diffraction peak of all four grains. This larger peak width is interpreted as a sign of larger misorientation within the grains at the compressive loop tip as opposed to the tensile loop tip.

The experiment was simulated using a crystal-based finite element model. Experimental diffraction peaks were compared to synthetic diffraction peaks produced from the simulation data through the virtual diffractometer framework. Individual, simulated diffraction peaks revealed an asymmetry in azimuthal peak widths between tension and compression, however, did not capture the strong bias exhibited by every peak shown by the experimental data.

1.2.2 Chapter 3

Chapter 3 titled, "Observing structural heterogeneity within a polycrystal during cycling using high energy x-ray diffraction and the implications for crystal scale models," was submitted to Acta Materialia and is under revision. Within this work, pure copper is tested in addition to the OMC alloy. Rather than monitoring the changes in the shape of diffraction peak widths visually, x-ray diffraction based heterogeneity metrics for strain and orientation are developed. These metrics present a single scalar value for each grain, which can be monitored as the sample is cyclically deformed.

The work moves from monitoring a few targeted grains to monitoring every grain within a diffraction volume. Samples of both pure copper and OMC alloy are tested up to a total of 16 cycles at fixed strain amplitude. Comparisons of the two materials reveals drastic differences between the changes in structural

heterogeneity within the grains as the samples are cycled.

The crystal plasticity formulation is extended to incorporate latent hardening in an effort to capture the strong misorientation bias observed experimentally. The modified hardening law does alter the misorientation within the grains, however, does not capture the strong asymmetry observed in the experiments.

1.2.3 Chapter 4

Chapter 4 titled, "Correlating three-dimensional grain maps and structural heterogeneity across hundreds of cycles," presents currently unpublished work on pure copper. These experimental data is measured during two different beamtimes at the Cornell High Energy Synchrotron Source (CHESS). First, a volume of grains is scanned using the novel near-field, box beam technique. This technique places a small area detector approximately 5-10 mm from the sample, enabling the creation of a three-dimensional grain orientation map. A reference marker in the form of a platinum wire was adhered to the sample to track the experimental volume from one beamtime to the next. This same sample returned for a subsequent beamtime during which time the far-field geometry was implemented such that misorientation within the grains could be monitored during cycling. Samples were only cycled at fixed strain amplitude for up to 16 cycles during the previous experiment. This final experiment presents measurements up to a total of 256 cycles. Detailed x-ray measurements around the hysteresis loops are performed for cycle numbers 2 and 256.

A novel data reduction methodology is implemented to monitor the dis-

tribution of orientation within each grain as the sample is deformed. This final chapter describes the methodology to construct orientation ”clouds” in Rodrigues space for each grain. Generating these ”clouds” and analyzing their distribution provides a measure of the distribution of orientation (misorientation) within each grain and is equivalent to the orientation heterogeneity metric developed in the previous chapter. The misorientation within each grain is monitored and projected onto the three dimensional grain map. This data set serves as the first opportunity to combine spatial grain maps of the aggregate with the heterogeneity metrics measured in the far-field geometry.

CHAPTER 2

QUANTITATIVE ANALYSIS OF CRYSTAL SCALE DEFORMATION HETEROGENEITY DURING CYCLIC PLASTICITY USING HIGH ENERGY X-RAY DIFFRACTION AND FINITE ELEMENT SIMULATION

2.1 Abstract

Modern high energy, x-ray diffraction experiments coupled with a crystal-based finite element model employing forward projection of virtual x-rays through each element is applied to study cyclic plasticity. An Okegawa Mold Copper (OMC) specimen was cyclically deformed *in situ* at the Advanced Photon Source (APS). Strain amplitudes of the cyclic experiments reached well into the plastic regime and diffraction images were generated at the hysteresis loop tips at every cycle using a high energy x-ray diffraction (HEXD) methodology. Four grains within the bulk of a polycrystalline sample were tracked and interrogated with x-rays. Diffraction peak data were reduced to center of mass (COM) and full width at half maximum (FWHM) values in the detector coordinates 2θ (radial) and η (azimuthal). The peaks evolved with cycles and changed significantly when the plastic strain amplitude was increased. The peaks evolved during the course of one loading cycle with larger η FWHM values seen at the compressive end of the cycles. This trend was reversed when the sample was initially loaded in compression. Diffracted intensity distributions were also seen to change significantly from one grain to the next. Using a virtual diffractometer model, COM and FWHM values were computed from the modeling results by projecting x-rays through the finite element mesh and compared to the experimental data. The finite element polycrystal model serves as the final step in

the data reduction process, revealing significant spatial heterogeneity of orientation, stress and plastic strain rate distributions. Studying these distributions collectively will be necessary to fully understand the detailed elastic-plastic deformation behavior within each grain and to explore problems such as microcrack initiation hypotheses in polycrystalline metals.

2.2 Introduction

Fatigue remains one of the most prevalent forms of failure for many mechanical components, yet our understanding of plasticity-driven microcrack initiation in ductile polycrystalline metals like copper is entirely empirical. Based on single crystal research, we have a notion of how heterogeneous cyclic plasticity processes produce a microcrack during low cycle fatigue (LCF) conditions. True prediction of microcrack initiation in a polycrystal, however, will require us to deepen our understanding of crystal and sub-crystal cyclic plasticity processes. It entails linking heterogeneous stress, orientation and deformation fields produced during cyclic plasticity into a theory for material evolution and eventual damage initiation. In this paper, we describe a methodology designed to study and quantify cycle-by-cycle micromechanical changes that occur inside individual grains[1] within a polycrystal subjected to LCF conditions. Cyclic plasticity processes in a ductile metal like copper are the roots of microcrack initiation. Therefore, our focus is the creation of a method for studying the plasticity-driven evolution of individual metallic crystals within a cyclically loaded polycrystalline aggregate during the first few fatigue cycles - long before the appearance of a crack.

[1]Note: the words **crystal** and **grain** are used interchangeably throughout this paper.

We conduct high energy x-ray diffraction experiments with *in situ* cyclic mechanical loading designed to probe the state of individual crystals **during** fatigue conditions. In addition to extracting lattice strains, we explore the use of the three-dimensional broadening of the diffraction peaks collected on the detector as indicators of structural heterogeneity. We examine changes in diffracted intensity distributions that occur as a result of increases in the strain amplitude as well as due to changes after several cycles. Finally, we employ a crystal-based finite element model of the deforming aggregate to link the evolving distributions of diffracted intensity measured on the x-ray detector to the underlying material heterogeneity that produces the peak evolution and will ultimately produce a microcrack. Experimental detector images are directly linked to the model by projecting x-rays through the deforming finite element mesh onto a virtual detector and comparing the two side-by-side.

2.3 Background

Much of our understanding of cyclic plasticity and microcrack initiation processes in ductile metals like copper was gained through experiments using single crystal specimens oriented for single slip (SCSS) [37, 3, 80, 56, 24]. By strategically choosing the sample orientation in a SCSS experiment, all plasticity is accommodated with one slip system. This allowed researchers to investigate the detailed transition from spatially heterogeneous plasticity to strain localization associated with persistent slip bands (PSBs). For nearly a century, the PSB has often been observed during cyclic plasticity and had been empirically linked to microcrack initiation [23, 73]. The SCSS research established the connection of PSBs with the ”threshold” region in the cyclic stress-strain curve for

copper and evidence was provided for hypotheses linking PSBs to the initiation of microcracks cf. [56, 71]. However, beyond the basic premise that fatigue crack initiation is intimately linked to the heterogeneity of cyclic plastic deformation, the SCSS results have not been used to build specific understanding of polycrystalline cyclic plasticity leading to microcracks. Slip in a crystal embedded within a polycrystal now may occur on multiple slip systems and will usually evolve as the state of the crystal (and the states of the crystals around it) evolves. While PSBs are often observed forensically within polycrystalline samples, they can no longer be linked directly to stress-induced slip process. So, in a polycrystal, the PSB itself appears to no longer be the ubiquitous pre-crack structure. However, the evolving spatial heterogeneity of slip within each crystal comprising a polycrystalline aggregate must still play a major role in fatigue crack initiation. This paper describes a new set of tools designed to track the evolution of each crystal during elastic-plastic cyclic deformation as a means for understanding the evolution of this heterogeneity.

2.3.1 Tools for Studying Cyclic Plasticity and Fatigue

Transmission electron microscopy (TEM) has been used for decades to understand the evolution of dislocation structures during cyclic plasticity and fatigue conditions cf. [5, 32, 29]. The SCSS work included TEM studies [56, 58, 42], which produced significant understanding of the dislocation structures associated with cyclic plasticity and the development of theories of cyclic strain hardening and softening, development of PSBs and eventually microcrack initiation cf. [48, 7]. In some cases, special methods using TEM [35, 9] and SEM [11] have been employed to image the juxtaposition of the PSBs and the microcracks.

X-ray diffraction has played a slightly less dominant but important role in studying fatigue. In a step towards delineating high cycle fatigue (HCF) from LCF, Wood observed that initially "sharp" diffraction peaks from a brass sample broadened into almost complete Debye-Sherrer rings at large strain amplitudes but varied little at lower strain amplitudes [90, 89]. Unlike Wood's x-ray data, which was limited to surface grains and required long exposures, the enormous flux at a synchrotron light source enables us to collect diffraction patterns from individual grains deep within the interior of a test specimen. In our modern versions of Wood's experiments, we make many diffraction measurements per second while cycling the specimen *in situ* - gathering data on every grain within the diffraction volume at many stages of material evolution cf. [65, 46]. Diffraction techniques have been developed to measure the spatial position, lattice orientation, topology, and lattice strains for grains within polycrystals [61, 13], enabling the collection of vast amounts of data from deforming polycrystals.

2.3.2 High energy x-ray diffraction (HEXD) experiments

This work focuses on the patterns that diffracted x-rays produce on real and virtual detectors. To properly describe these patterns and their connections to the underlying material, a very basic introduction to diffraction is provided here. Much more comprehensive descriptions are found elsewhere [38, 17, 18, 2]. The transmission HEXD experiment we conduct is shown schematically in Figure 3.2. Within the volume illuminated by the beam (diffraction volume) every individual grain (crystal) containing a family of planes, an *hkl*, satisfying Bragg's law will diffract, producing a peak of diffracted intensity on the detector. Bragg's law relates the lattice spacing for a particular family of planes, d_{hkl},

and diffraction angle, θ_{hkl}, to the x-ray wavelength, λ.

$$\lambda = 2d_{hkl} \sin \theta_{hkl} \tag{2.1}$$

In our experiments, the size of the grains relative to the diffraction volume is such that the diffraction peaks from individual grains can be delineated. The goal of the experiments is to connect each diffraction peak to a particular *hkl* in a particular grain, then describe the location and topology of each diffraction peak. This requires the introduction of reciprocal space and a more sophisticated vector-based diffraction model, the Laue equation.

The crystal lattice is described using a set of basis vectors. The magnitudes of the basis vectors define the edge lengths of the unit cells, while the angles between vectors define its shape. Our material is a face centered cubic (fcc) copper alloy so our discussion is restricted to cubic symmetry. The basis vectors for the cubic unit cell in the crystal coordinate system are defined as,

$$\mathbf{a}_1 = a[1,0,0],\ \mathbf{a}_2 = a[0,1,0],\ \mathbf{a}_3 = a[0,0,1] \tag{2.2}$$

where a is the lattice constant. The reciprocal basis vectors are defined as:

$$\mathbf{b}_1 = \frac{\mathbf{a}_2 \times \mathbf{a}_3}{\mathbf{a}_1 \cdot \mathbf{a}_2 \times \mathbf{a}_3},\ \mathbf{b}_2 = \frac{\mathbf{a}_3 \times \mathbf{a}_1}{\mathbf{a}_1 \cdot \mathbf{a}_2 \times \mathbf{a}_3},\ \mathbf{b}_3 = \frac{\mathbf{a}_1 \times \mathbf{a}_2}{\mathbf{a}_1 \cdot \mathbf{a}_2 \times \mathbf{a}_3} \tag{2.3}$$

Now a reciprocal lattice vector, $\mathbf{G}_{hkl}$, which identifies a point in reciprocal space can be defined using the reciprocal basis vectors and the Miller indices of a lattice plane, *hkl*, as

$$\mathbf{G}_{hkl} = h\mathbf{b}_1 + k\mathbf{b}_2 + l\mathbf{b}_3 \tag{2.4}$$

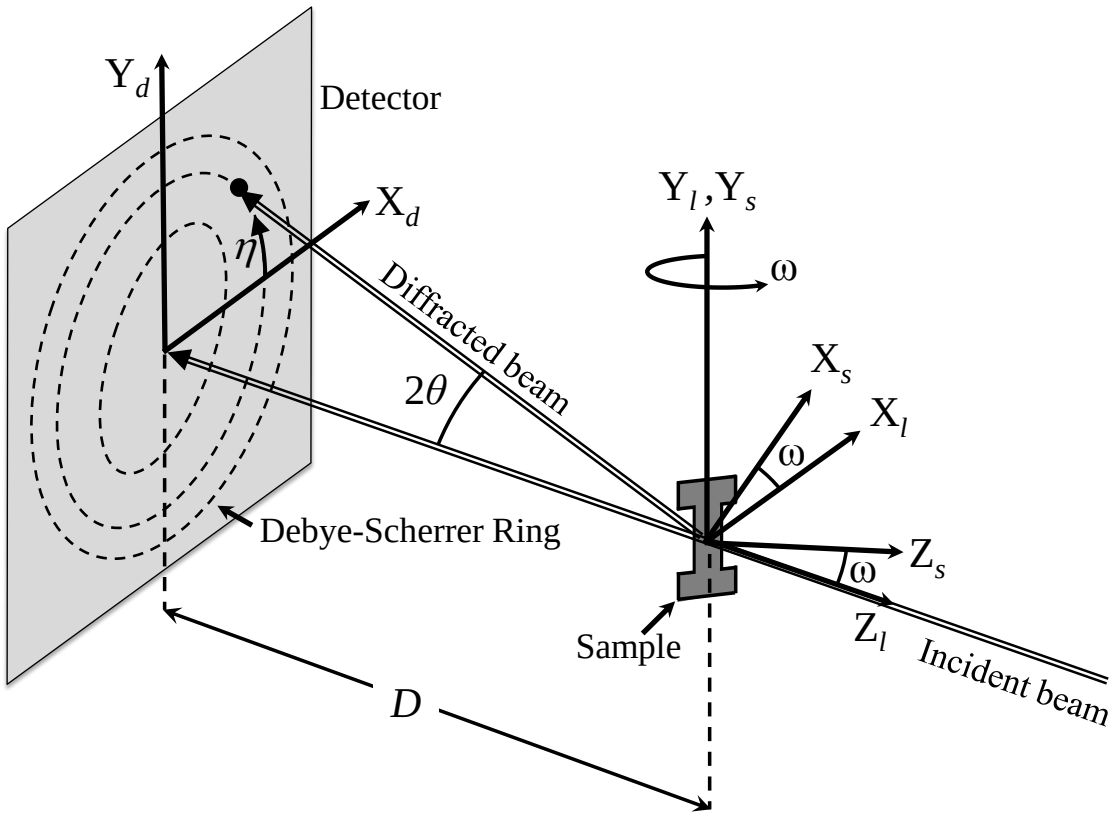

Figure 2.1: Schematic of the HEXD experimental setup. The laboratory coordinate system, $\{\mathbf{X}_l, \mathbf{Y}_l, \mathbf{Z}_l\}$, is fixed and the sample coordinate system, $\{\mathbf{X}_s, \mathbf{Y}_s, \mathbf{Z}_s\}$, rotates about the loading axis with defined angle, ω. Points on the detector can be described using its rectangular coordinate system, $\{\mathbf{X}_d, \mathbf{Y}_d\}$ or a "polar" coordinate system, $\{2\theta, \eta\}$. The angle 2θ corresponds to the Bragg angle in Equation 2.1 and the azimuthal angle, η, is measured as shown. The sample to detector distance is D.

A scattering vector, $\mathbf{Q}$, associated with the incident beam is defined as

$$\mathbf{Q} \equiv \frac{\mathbf{s}_o - \mathbf{s}_i}{\lambda} \tag{2.5}$$

where $\mathbf{s}_i$ and $\mathbf{s}_o$ are unit vectors in the directions of the incident and outgoing (diffracted) x-ray beams, respectively, the Laue condition for diffraction to occur in the $\mathbf{s}_o$ direction from a particular set of planes is simply $\mathbf{Q} = \mathbf{G}_{hkl}$.

Again, the structure of reciprocal space means $\mathbf{G}_{hkl}$ is normal to the hkl set of

lattice planes and by enforcing equivalence of Bragg's law and the Laue equation, it is straight-forward to show that for a cubic crystal,

$$d_{hkl} = \frac{1}{\|\mathbf{G}_{hkl}\|} = \frac{a}{\sqrt{h^2 + k^2 + l^2}} \tag{2.6}$$

In the experiment, the sample is rotated around the loading axis, $\mathbf{Y}_l$, while illuminating the diffraction volume with x-rays (Figure 3.2). During the rotation (given by the variable, ω) the $\mathbf{G}_{hkl}$ vectors come into and out of alignment with scattering vectors ($\mathbf{Q}$'s) so diffraction peaks turn on and off. Typically, we rotate the specimen continuously, truncating data collection on the detector at small values of $\Delta\omega$. Each peak on the detector can be parameterized with a triplet of angles (2θ, η, ω), where 2θ and η, correspond to the radial and azimuthal position of the peak, respectively, and ω is the average angular position of the diffractometer when the data were collected (during a particular $\Delta\omega$).

2.3.3 Interpretation of peaks

The distance from the sample to the x-ray detector largely determines the type of information that can be extracted directly from the experimental peaks [65]. Experimental configurations are often grouped into three categories: *near field*, *far field*, and *very far-field*. If the detector is placed very near the sample, on the order of millimeters, the diffracted intensity appearing on the detector takes on the shape of the crystal and its position on the detector will be related to the position of the crystal within the aggregate. A *near field* diffraction geometry increases the spatial sensitivity at the expense of 2θ resolution [44, 72, 47]. The near field geometry is useful for generating spatial orientation maps of crystal aggregates. As opposed to such *near field* experiments, the experiments described in

this work are termed *far field* in the diffraction lexicon because at the typical sample to detector distances used in these studies (D≈1m), the shape of the peak on the detector and its location are sensitive to internal crystal structure and orientation. Volume averaged grain orientations and elastic strain tensors along with grain positions can be measured in this geometry [65, 13]. The detector is moved even further away from the sample for the *very far field* experimental configuration. Single diffraction peaks are interrogated on a detector with very high angular resolution. These types of measurements enable the construction of reciprocal space maps [64, 33].

Using the $(2\theta, \eta, \omega)$ values from all peaks associated with the unstrained crystal, the crystal orientation can be determined. Straining or rotating the crystal will produce shifts in the peaks and changes in $(2\theta, \eta, \omega)$. As can be discerned from Bragg's law (Equation 2.1) and Figure 3.2, changes in the radial position of a peak (2θ) are related to changes in d_{hkl} or, equivalently, the normal lattice (elastic) strain associated with that particular scattering vector. Shifts in η and ω are, in general, related to crystal reorientation [2].

A crystal within a plastically deforming polycrystal is loaded by the other crystals at its boundary, producing internal lattice strain and orientation gradients. These intragrain gradients produce a distribution of $\mathbf{G}_{hkl}$ vectors within the material, which will coincide with slightly different scattering vectors when diffraction conditions are satisfied and expand the distribution of diffracted intensity measured on the detector. The once sharp[3] peak of the undeformed crys-

[2]This is a somewhat imprecise statement. Considering the 2θ, η, ω parameterization of the unit cell geometry, changes in each can be related to distortion or reorientation [13]. In the case of metallic systems where the elastic strains are small, associating changes in 2θ with lattice strain and changes in η and ω with changes in orientation is a valid approximation.

[3]The size and shape of the intensity distribution on a far field detector from an unstrained nearly perfect crystal will be dominated by effects from the instrument: energy band width, detector attributes, pixel size etc., not the material state. Our focus is more on changes that

tal now shifts and spreads in three dimensions (2θ, η and ω) consistent with the deformation-induced distribution of $\mathbf{G}_{hkl}$ ($\mathbf{Q}$) vectors[4] as depicted in Figure 2.2, which shows that the individual diffraction peaks expand or broaden significantly in the azimuthal (η) direction and, less noticeably, in the radial (2θ) direction when the material is plastically deformed. The radial broadening is primarily a result of an increase in the lattice strain heterogeneity within a grain, while the azimuthal broadening is related to an increase in the orientation heterogeneity. Broadening in ω is manifest as peaks "appearing" on the detector from the deformed specimen. As can be seen in Figure 2.2, the orientation spread associated with plastic deformation causes the Debye-Scherrer rings to become more densely populated as the diffraction peaks spread in ω. Once peaks begin to overlap, it becomes difficult to separate the information contained within each individual peak.

2.4 Experimental Method

HEXD experiments employing *in situ* cyclic mechanical loading were performed at the 1-ID-C experimental station at the Advance Photon Source (APS) at the Argonne National Laboratory. Details of the material and experimental methods are presented below.

occur in the peaks upon loading. Barring changes in the x-ray conditions, these changes will all be due to material evolution.

[4]Note: By virtue of the Laue equation $\mathbf{G}_{hkl}$ and $\mathbf{Q}$ are equivalent when diffraction conditions are met. This is the only condition relevant in this paper; hence, one could interchange the symbols for these vectors with no loss of arithmetic correctness, which we do here.

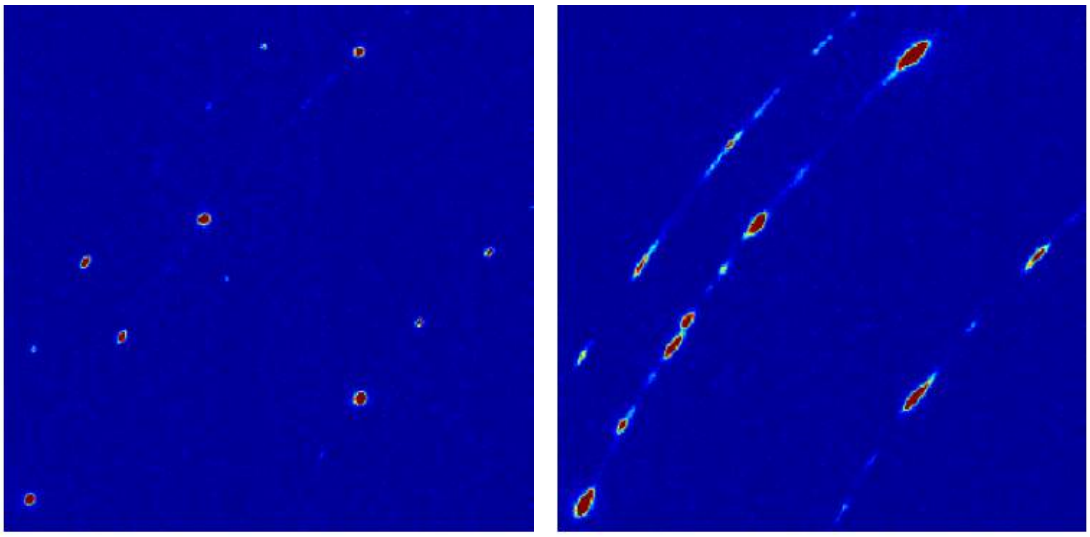

Undeformed Plastically Deformed

Figure 2.2: (Left) One portion of a detector frame gathered downstream from an OMC copper sample in an undeformed state and (Right) at 1% macroscopic strain. Each image was taken over the same ω range.

2.4.1 Material

For many reasons, copper has been a model material for studying cyclic plasticity and fatigue processes including microcrack initiation in ductile materials. Precipitation-strengthened Okegawa Mold Copper (OMC) (0.5 wt% Cr, 0.02 wt% Zr), was chosen for this research due to its relatively high yield strength of around 245-295 MPa as compared to elemental copper. The precipitation reaction completely depletes the Cu matrix of Cr and Zr, however, so the OMC material should have stacking fault energies and moduli comparable to high purity copper. The polycrystalline material was found to have a uniform orientation distribution and an average grain size of 60 microns through electron backscatter diffraction (EBSD) measurements

2.4.2 *In situ* mechanical loading

OMC copper samples were deformed in a custom-designed compact uniaxial load frame. Experimental samples had a 9 mm long gauge section with a 2×2 mm square cross-sectional area within the gauge length. A cyclic incremental step test was conducted; the stress-strain history is shown in Figure 2.3. Loading began in tension with the strain amplitude increasing from 0.3% to 0.5% after three cycles. Three additional cycles were then performed at the 0.5% amplitude. Deformation was halted at various points during cycling to perform the HEXD measurements. Prior to each HEXD measurement (labeled with markers in Figure 2.3), the load was reduced in magnitude by 10% to move the stress away from the yield surface and to minimize microstructural evolution during diffraction measurements. The first marker resides at the origin and corresponds to the undeformed state. Four clusters of points are located at the tensile and compressive "tips" of the stress-strain loop at both strain amplitudes. Each cluster contains three markers, corresponding to the three cycles performed at each strain amplitude. The stress-strain response of the finite element simulation is included for comparison and will be discussed later.

2.4.3 X-ray diffraction

A monochromatic x-ray beam with energy, E, of 80.725 keV was utilized with $\Delta E/E = 5 \times 10^{-3}$. A beam size of 400 μm x 400 μm was employed so that each target grain was entirely illuminated by the x-ray beam. The x-ray beam was centered onto each target grain prior to conducting diffraction measurements on that grain. A high speed area detector, the GE Revolution 41RT, with an

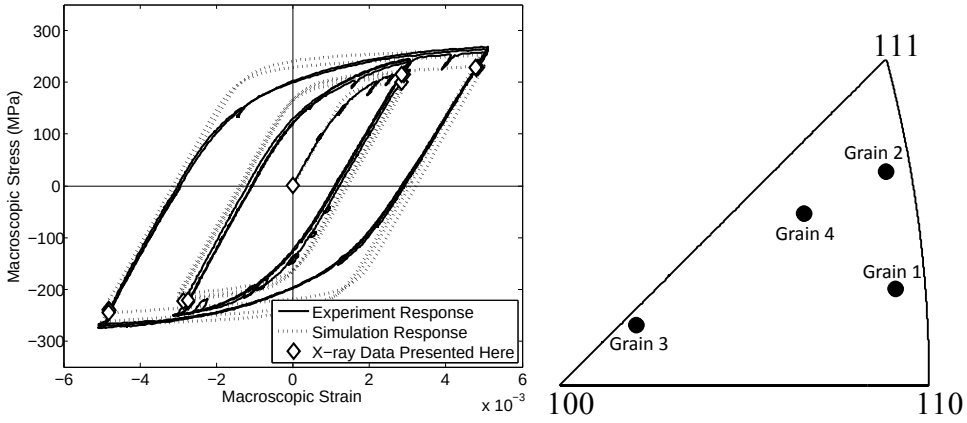

Figure 2.3: (Left) Macroscopic stress-strain curve from the cyclic incremental step test on OMC copper. Both experiment and simulation are depicted. The HEXD measurement locations are highlighted. (Right) Cubic stereographic triangle depicting the preloading orientation of the tensile axis with respect to the orientations of the four target grains at the beginning of the experiment.

active area of 41 × 41 cm^2 with a 200 × 200 μm^2 pixel size was employed to gather diffraction patterns. Detector center and tilts relative to the beam and the sample to detector distance (1.122 m) were calibrated using a CeO2 powder [70]. During diffraction measurements, detector frames containing diffraction peaks from several Debye-Scherrer rings were acquired as the sample was rotated through a total of 300° in ω. The rotation was discretized into 0.25° $\Delta\omega$ steps. The experimental geometry and the range of rotation angles results in the ability to capture over 100 diffraction peaks for each grain.

Indexing the diffraction data involves associating the coordinates (2θ, η and ω) of each measured peak with a particular grain. We indexed our data using the HEXRD software package [13]. After indexing and locating each grain in the aggregate at zero load, we chose to track four particular OMC copper grains within four diffraction volumes centered on each crystal. Figure 2.3 provides the initial location of the tensile axis for the four target grains chosen to be tracked

during the experiment within the cubic fundamental triangle. The spread over the stereographic triangle was purposely chosen to examine orientation effects.

2.5 Data analysis

The section below describes the manner in which the diffracted intensity distribution associated with each peak is quantified and represented. We begin by describing how intensity related to one peak is integrated over multiple detector frames (ω integration) then describe the process of finding the centroid (COM) and full width at half maximum (FWHM) values of the distribution relative to the 2θ and η (radial and azimuthal, respectively) detector coordinates. This process is depicted schematically in Figure 2.4.

A broadened peak can extend across several $\Delta\omega$'s so to consistently account for the full distribution of diffracted intensity, we integrated across all frames containing intensity from that peak. This process, which basically consists of adding the intensity values from each pixel across multiple detector frames, is depicted for a typical broadened peak in the left hand side of Figure 2.4. Fitting in the radial and azimuthal directions begins by mapping pixel intensities from the rectangular coordinates to the (2θ, η) "polar coordinates", which serve as a more natural coordinate system for the present diffraction geometry [70]. As depicted in Figure 2.4, first the peak was integrated in η and fit as a function of 2θ, and then the peak was integrated in 2θ and fit as a function of η using a pseudo-Voigt function. The COM and FWHM of each distribution become the measures of position and spread, respectively, in 2θ and η.

Using the COM values for each peak associated with a grain, a "grain-

averaged" lattice orientation and lattice strain tensor can be defined. Employing an engineering definition of strain and using the unstrained lattice spacing (d^o_{hkl}) as the "gage length", changes in the 2θ COM for a particular peak can be converted to changes in d_{hkl} using Bragg's law, which can then be used to calculate the "grain-averaged" normal lattice strain component associated with that particular *hkl* and scattering vector, **Q**, i.e.

$$\varepsilon_{QQ} = \frac{d_{hkl} - d^o_{hkl}}{d^o_{hkl}} = \frac{\|\mathbf{G}^o_{hkl}\| - \|\mathbf{G}_{hkl}\|}{\|\mathbf{G}_{hkl}\|} \tag{2.7}$$

The ε_{QQ} component of strain can be related to the grain-averaged lattice strain tensor, ε, using the tensor transformation equation,

$$\varepsilon_{QQ} = \hat{\mathbf{Q}}\, \varepsilon \cdot \hat{\mathbf{Q}} \tag{2.8}$$

with $\hat{\mathbf{Q}} = \mathbf{Q}/\|\mathbf{Q}\| = \mathbf{G}_{hkl}/\|\mathbf{G}_{hkl}\|$. Since, lattice strains are elastic, the grain-averaged stress tensor can be computed using Hooke's law, $\sigma = \hat{\mathbf{C}}\varepsilon$, where $\hat{\mathbf{C}}$ is the fourth order tensor of single crystal elastic moduli.

2.6 Simulations

In many traditional approaches, modeling and experimental results are compared and either the model or the experiment is deemed "validated" or "calibrated". Our approach is instead to employ the finite element model of the deforming diffraction volume as the key component in our diffraction data reduction process. As we will show in Section 2.7, the COM and FWHM data from the *in situ* experiments have significant potential for providing indicators

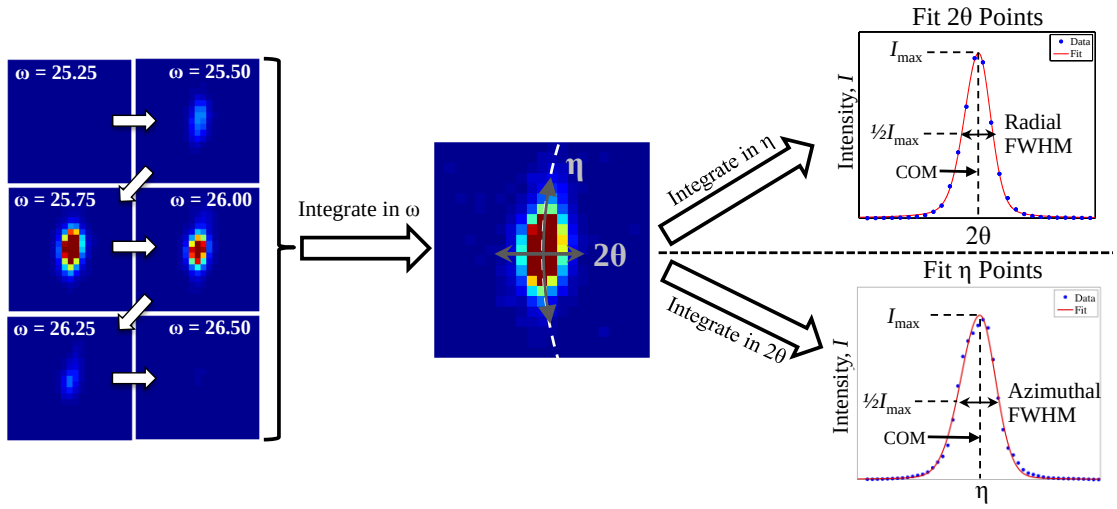

Figure 2.4: Schematic portraying the process of converting the intensity distribution data from the detector for a single diffraction peak into center of mass (COM) and full width at half maximum (FWHM) values in the polar coordinates, 2θ and η. (Left) The peak is first integrated in ω over all detector frames ($\Delta\omega$) containing nonzero intensity values related to that peak. A central $\Delta\omega$ is identified and its midrange is termed the ω COM. (Upper Right) The ω-integrated peak is integrated azimuthally and fit radially for the 2θ COM and FWHM values and (Lower Right) the peak is integrated radially and fit azimuthally to obtain the η values of COM and FWHM.

of the effects of cyclic plasticity on the internal structure of an individual grain. The key element to the construction of the model - the way that the model and experiment are brought into coincidence - is through a comparison of the experimental COM and FWHM data to values derived from the model using a digital representation of the diffraction experiment, a virtual diffractometer. In this section we first introduce the crystal-based representation of the mechanical response of the specimen, and then we provide a description of the x-ray diffraction model: the virtual diffractometer.

2.6.1 Crystal-based finite element model

The model employed here represents the elastic-plastic deformation behavior of each crystal using anisotropic elasticity and restricted-slip viscoplasticity [50, 51, 28]. Each crystal is discretized using many finite elements and the polycrystalline aggregate is assembled to resemble the diffraction volume of the experiment. The kinematics employed in the model allows for motions with large strains and arbitrary rotations in a fully three-dimensional framework. Within each crystal, slip can occur on any of the twelve {111} <110> slip systems available to FCC crystals, with the shearing rate on the α-slip system, $\dot{\gamma}^{\alpha}$, expressed as

$$\dot{\gamma}^{\alpha} = \dot{\gamma}_0 \cdot \left[\frac{\tau^{\alpha}}{g^{\alpha}}\right]^{1/m} \mathrm{sgn}(\tau^{\alpha}) \tag{2.9}$$

where $\dot{\gamma}_0$ and m are material constants, τ^{α} is the resolved shear stress on the α-slip system and g^{α} is the slip system strength of the α-slip system. The model utilizes one strength for every slip system in the crystal ($g^{\alpha} = g$), which evolves according to

$$\dot{g} = h_0 \left(\frac{g_s(\dot{\gamma}) - g}{g_s(\dot{\gamma}) - g_0}\right) f \tag{2.10}$$

where h_0 and g_0 are material constants and

$$g_s(\dot{\gamma}) = g_{s0}(\dot{\gamma}/\dot{\gamma}_{s0})^{m'} \tag{2.11}$$

Here g_{s0}, $\dot{\gamma}_{s0}$ and m' are also material constants. The parameter f, defined as

$$f = \sum_{\beta=0}^{n_a} \mid \dot{\gamma}^{\beta} \mid \tag{2.12}$$

is used to capture the amplitude-dependent strain hardening behavior observed in the macroscopic stress-strain data shown in Figure 2.3 [74]. The shearing rate on a particular slip system only contributes to the total (n_{α}) if the shear strain accumulated on the slip system since the last reversal in shearing direction reaches

Table 2.1: Single crystal elastic constants (copper) employed in the simulation (GPa) [30], along with the visco-plasticity model constants used for the OMC copper.

C_{11}	C_{12}	C_{44}	h_0(MPa)	g_0(MPa)	g_{s0}(MPa)	m	m′	$\dot{\gamma}_0(s^{-1})$	$\dot{\gamma}_{s0}(s^{-1})$	a	b
164	122	75	800	85	285	0.01	0.0	1.0	5×10^{10}	0.3	4.0

a critical value, $\Delta\gamma_{crit}$, defined as

$$\Delta\gamma_{crit} = a[g/g_s]^b \tag{2.13}$$

Here a and b are material constants. The model parameters for the OMC copper were determined by fitting the macroscopic stress-strain data. The single crystal elastic moduli of copper were employed for the OMC copper. All model constants are given in Table 2.1.[5]

The initial volume of the virtual sample was chosen as 0.5 mm×0.5 mm×0.5 mm, which is slightly larger than the beam size used in the experiment. The orientations and centroid locations of the four target grains, which were obtained from the HEXD experiment, were replicated in the virtual sample. The orientations of the remaining crystals within the diffraction volume were taken from the measured orientation distribution function (ODF) of the OMC material. Based upon the average grain size of the material, the sample domain was discretized into 100 individual grains using Neper, a crystal generation and meshing program that uses a Voronoi tessellation scheme. Neper has a meshing algorithm that produces irregularly shaped grains with a high quality, robust finite element mesh [67, 66]. As we have shown in previous work, the crystallographic neighborhood has a bearing on the response of an individual crystal

[5]The fact that $m' = 0$ implies that the evolution equation is rate independent.

[87]. However, since the shape of the grains and the exact details of their neighborhoods are not known from the experiment, no attempt was made to replicate these attributes of the physical specimen. Each grain is assumed to be one orientation and initially strain free and is finely discretized into 1000's of 10-node tetrahedral elements. With the discretization used, gradients of stress, orientation and inelastic strain rate are well represented across each crystal.

2.6.2 Virtual diffractometer

The virtual diffractometer uses a "forward projection" of the x-ray beam through the virtual diffraction volume to simulate the diffraction experiment. The chief advantage of employing the virtual diffractometer is the ability to compare to the experimental results in their most fundamental state - with a minimum amount of "processing". Within its framework, the x-ray beam is assumed to be perfectly collimated, and the energy bandwidth from the actual instrument is employed. Using the deformation information stored within each element, a $\mathbf{G}_{hkl}$ is calculated. As the virtual sample is rotated, each element is checked to see if it satisfies a diffraction condition ($\mathbf{G}_{hkl} = \mathbf{Q}$). If the resulting $\mathbf{s}_o$ intersects the virtual detector, it is projected onto the virtual detector and the detector point spread function is applied [45]. A more detailed description of the virtual diffractometer can be found in [86].

2.7 Results

The results, including raw COM and FWHM data from the experiments and those determined using the virtual diffractometer model and the simulation data are presented along with examples of the stress, orientation and plastic strain rate fields derived from the simulation. The results are discussed in Section 2.8.

2.7.1 Experimental results

As an example, the positions of the peaks obtained for grain 4 at the beginning of the test (zero load) are depicted in Figure 2.5. Even though nearly 100 peaks can be identified for each grain, peak quality due to issues such as overlap reduced the list to 30-50 "acceptable" values for each grain.

Figure 2.6 contains components of the lattice strain tensor for all four grains at the tensile and compressive endpoints of the macroscopic stress-strain curve. All strain components are presented using sample coordinates, with the y-axis corresponding to the loading axis. The evolution of the radial FWHM magnitude during cycling reflects changes in the strain heterogeneity within a grain. Figure 2.7 presents this evolution for the four grains during cycling. The first row corresponds to the undeformed state and subsequent steps correspond to measurements made at points alternating between the tension and compression endpoints of the stress-strain history. Table 2.2 connects the rows in Figure 2.7, 2.8 and 2.10 to the strain value and cycle number where the associated HEXD experiment was conducted. Figure 2.8 displays the evolution the azimuthal (η)

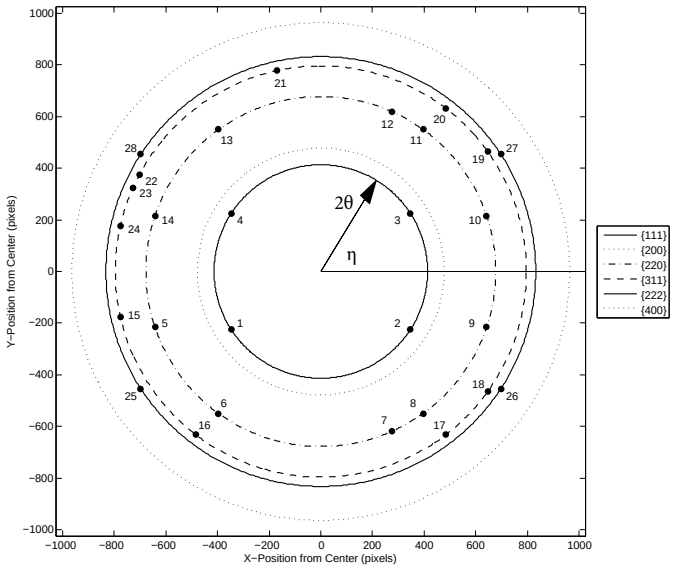

#	(h k l)	2θ	η	ω
1	(-1 -1 1)	4.22	-146.97	39.08
2	(-1 -1 1)	4.22	-33.03	-145.95
3	(1 1 -1)	4.22	33.03	34.05
4	(1 1 -1)	4.22	146.97	-140.92
5	(0 -2 2)	6.89	-161.40	4.18
6	(0 2 2)	6.89	-125.80	-111.17
7	(-2 0 2)	6.89	-66.11	-130.63
8	(0 2 2)	6.89	-54.20	57.08
9	(0 -2 2)	6.89	-18.60	176.92
10	(0 2 -2)	6.89	18.60	-3.08
11	(0 -2 -2)	6.89	54.20	-122.92
12	(2 0 -2)	6.89	66.11	49.37
13	(0 -2 -2)	6.89	125.80	68.83
14	(0 2 -2)	6.89	161.40	-175.82
15	(-1 3 -1)	8.08	-167.12	-177.40
⋮	⋮	⋮	⋮	⋮
25	(-2 -2 2)	8.44	-146.90	41.59
⋮	⋮	⋮	⋮	⋮
28	(2 2 -2)	8.44	146.90	-138.41

Figure 2.5: (Left) Approximate $(2\theta, \eta)$ positions of the centroids (COM) of the diffraction peaks as they appeared on the detector for grain 4 before deformation. Every peak from all values of ω are placed on this single image. (Right) The diffraction peaks for grain 4 listing the (hkl) and the COM values of the angles (2θ, η and ω) at the beginning of the experiment. Peak numbers correspond to columns. They also correspond to the columns for grain 4 in Figure 2.7 and Figure 2.9.

Table 2.2: Connection between the rows of data in Figure 2.7, 2.8 and 2.10 and strain value and cycle number (load step) where the associated HEXD experiment was conducted.

Row Number	1	2	3	4	5	6	7	8	9	10	11	12	13
Macro. Strain (%)	0	+0.3	-0.3	+0.3	-0.3	+0.3	-0.3	+0.5	-0.5	+0.5	-0.5	+0.5	-0.5
Cycle Number	0	1	1	2	2	3	3	1	1	2	2	3	3

FWHM of each peak for the four experimental target grains in the same manner as Figure 2.7.

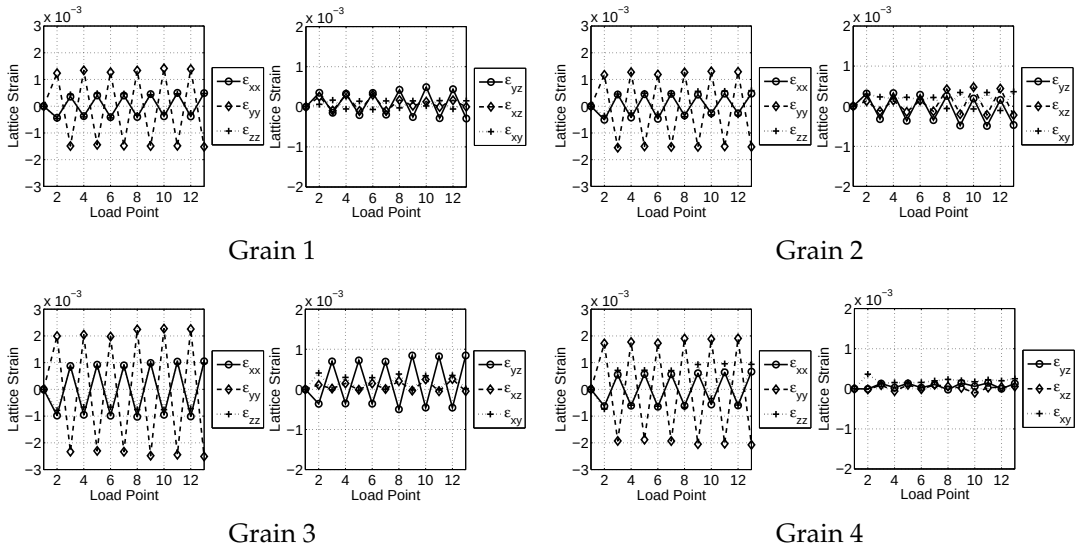

Figure 2.6: Experimental elastic strains for the four target grains. Load point 1 corresponds to the undeformed material and subsequent load points present data alternating between the tensile and compressive tips of the stress-strain history. The sample was loaded along the y-axis. Points are connected with lines merely to serve as a visual aid.

2.7.2 Simulation results

We illustrate the simulation results by showing results from grain 2 only. The simulated and measured lattice strain tensors for grain 2 are shown in Figure 2.9. Figure 2.10 provides a comparison of the radial and azimuthal FWHM values for the experiment and simulation for grain 2. The data are presented in the same manner as in Figure 2.7 and 2.8, where rows correspond to individual diffraction measurements and columns correspond to diffraction peaks.

The spatial variation of the lattice orientation, stress and plastic strain rate within grain 2 as computed by the model are illustrated in Figure 2.11 at +0.5% macroscopic strain in the final cycle. Lattice orientation variation is illustrated with a plot of the angular deviation away from the average. To illustrate the

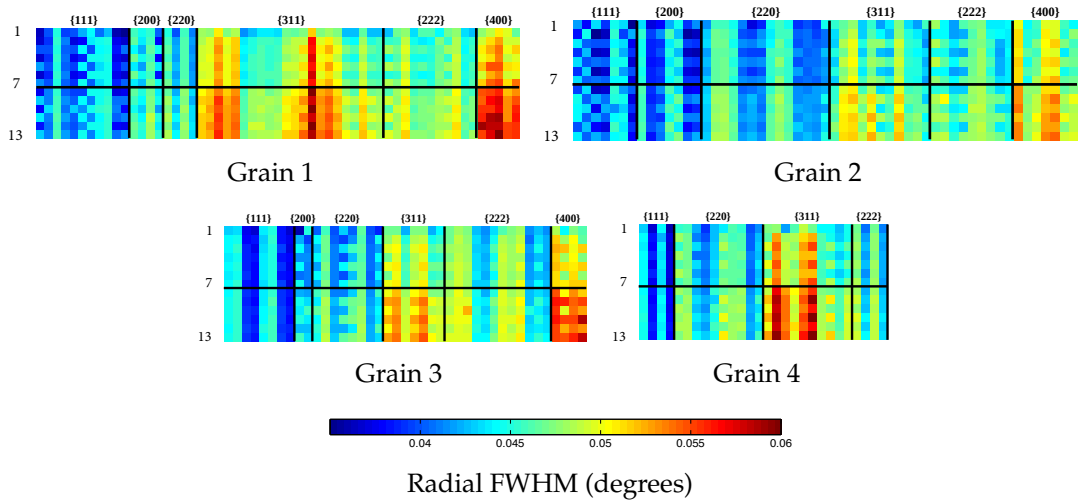

Figure 2.7: Radial (2θ) FWHM of four target grains from the experiment. The color of each "pixel" in the grid corresponds to the experimentally measured magnitude of the FWHM. Each row corresponds to a load step (a macroscopic strain value and cycle number) associated with a particular HEXD experiment. Table 2.2 connects the load step information to the rows of FWHM data. Each column contains the data from an individual peak. The peaks are sorted to help distinguish trends in the data. They are first grouped according to lattice plane family, {hkl}, and then by increasing azimuthal angle, η, within each family from -180° to 180°. Each peak is associated with a distinct ω-value. The bold horizontal line below row 7 indicates an increase in the macroscopic strain amplitude from 0.3% to 0.5%.

variation of stress, we plot the von Mises effective stress, $\bar{\sigma}$, over grain 2. The effective stress is computed from the full stress tensor, σ, as:

$$\bar{\sigma} = \sqrt{\frac{3}{2}\sigma' : \sigma'} \qquad \text{where} \qquad \sigma' = \sigma - \frac{1}{3}\text{tr}(\sigma)\mathbf{I} \tag{2.14}$$

where σ' is the deviatoric stress and $\mathbf{I}$ is the identity tensor. Similarly, we calculate the plastic work rate conjugate of $\bar{\sigma}$ as an effective plastic strain rate, $\bar{D}^{\text{p}}$, using the plastic rate of deformation tensor,

$$\bar{D}^{\text{p}} = \sqrt{\frac{2}{3}\mathbf{D}^{\text{p}} : \mathbf{D}^{\text{p}}} \tag{2.15}$$

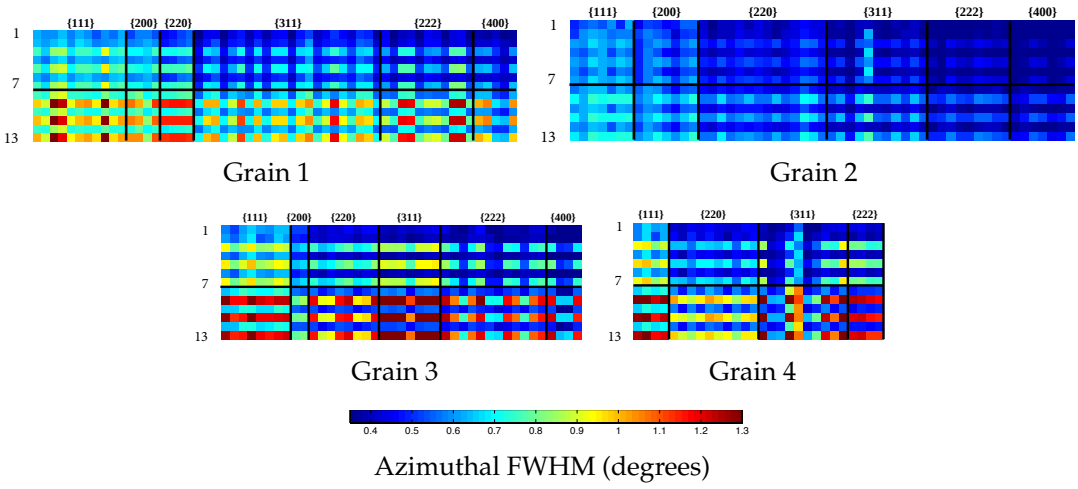

Figure 2.8: Azimuthal (η) FWHM values for the four grains depicted in an identical format as used in Figure 2.7 and described in Table 2.2.

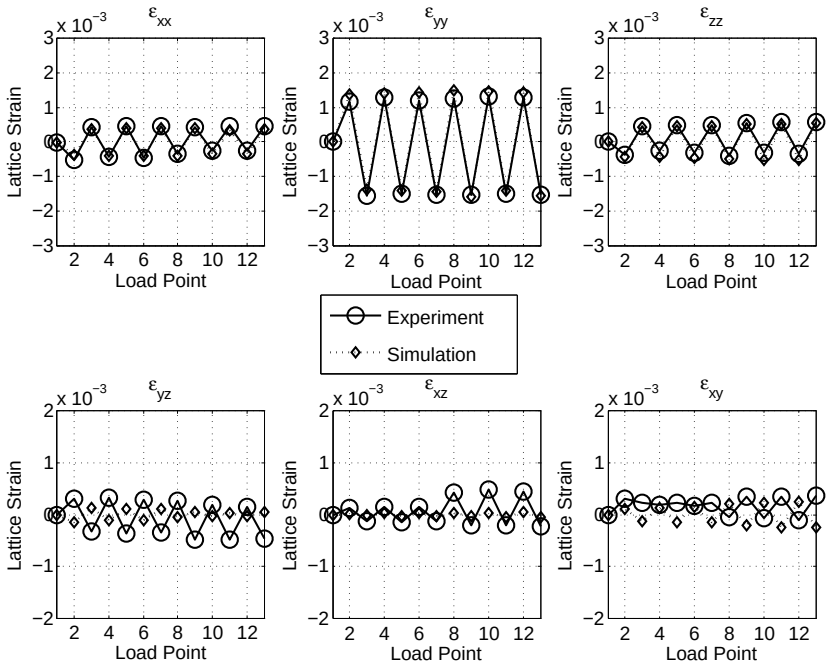

Figure 2.9: Grain-averaged components of the lattice strain tensor for grain 2 from experiment and simulation.

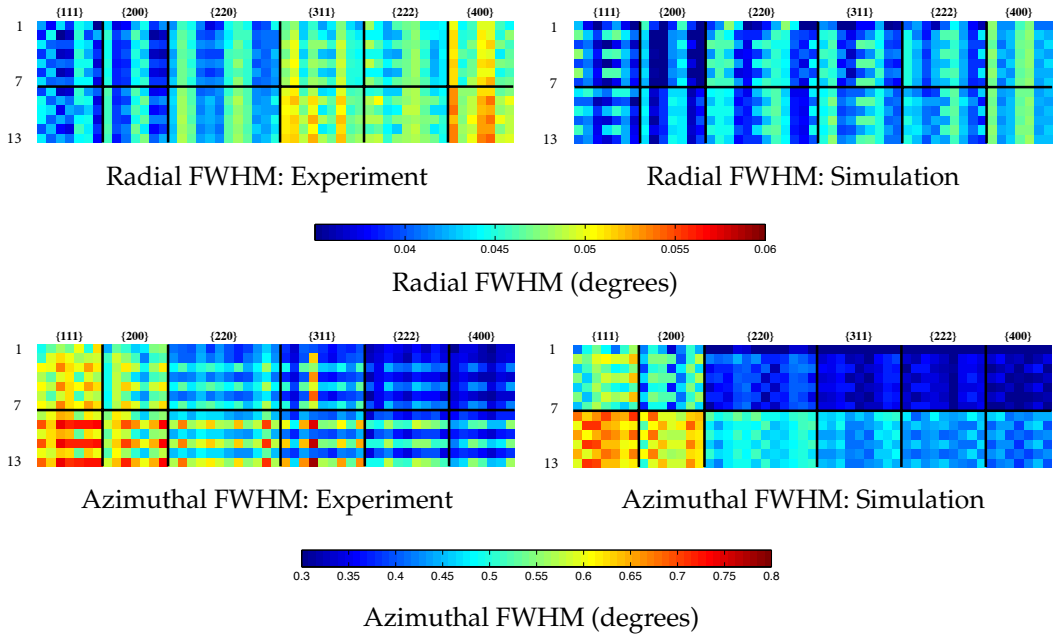

Figure 2.10: Radial and azimuthal FWHM values for grain 2 from the experiment and simulation. Each set of data is presented in the same format as that used in Figure 2.7 and described in Table 2.2

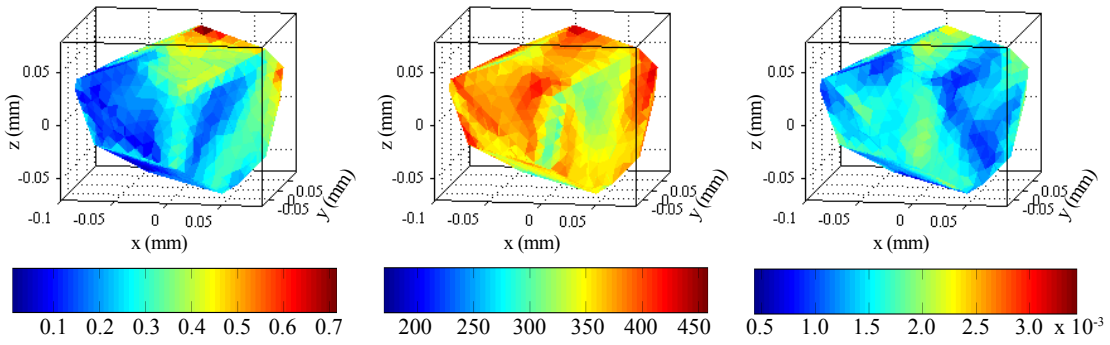

(a) Misorientation (degrees) (b) von Mises stress (MPa) (c) Effective plastic strain rate (s^{-1})

Figure 2.11: Distributions of lattice orientation (left), von Mises effective stress (middle) and effective plastic strain rate (right) on the surface of grain 2 on the final cycle (+0.5% macroscopic strain on Cycle 3) from the finite element model.

2.8 Discussion

This discussion begins with some general observations regarding the experimental data. We then discuss the way we link these data to our finite element representation of the individual grains to quantify intragrain distributions of stress, misorientation and plastic strain rate.

2.8.1 Diffraction-based data

Each diffraction peak captured on the x-ray detector contains a "snapshot" of the internal structure of a deforming grain. Given its underlying connection to plastic deformation, one could contend that the detector image in Figure 2.2 is a "picture" of plasticity comparable to a TEM micrograph of dislocation structures. Much more importantly, the COM and FWHM data derived from the peaks and presented in Figure 2.6 – Figure 2.8 are REAL mechanical testing data from **individual grains** deforming within an OMC polycrystalline sample subjected to the loading presented in Figure 2.3. While we have illustrated the potential of these experiments by showing data from only 4 grains, we obtained data from every grain within the diffraction volume. Since the loading conditions vary from grain to grain, the HEXD experimental methodology literally has allowed us to turn a fatigue specimen into a **testbed** of cyclic plasticity experiments on individual grains within a polycrystalline aggregate.

The lattice strain tensor for each grain is presented in Figure 2.6. As might be expected, the lattice strain in the loading direction, ε_{yy}, for each grain dominates. The transverse strains, ε_{xx} and ε_{zz}, are nearly identical and oscillate in

the opposite straining direction to ε_{yy}. The values of the normal strains vary from one grain to another and there appears to be slight differences in Poisson's ratio between the grains. The slight increase seen in ε_{yy} in each grain as the strain amplitude increases from 0.3% to 0.5% is consistent with the small elevation of macroscopic stress in the loading direction seen in Figure 2.3. With all of its shear strain components remaining near zero, the sample coordinate system would appear to be aligned with the principal lattice strain directions of grain 4.

The radial FWHM values are shown in Figure 2.7, providing an indication of how lattice strains are distributed across the grains and how the distribution changes with deformation. Some slight row to row oscillations can be seen in some of the FWHM values in Figure 2.7, indicating changes in the radial (2θ) spread from tension to compression. In some cases, the FWHM is larger in tension, in others it is larger in compression. The oscillations mean that a peak is spreading radially at one end of the cycle, then contracting back when returning to the other end. X-rays and classical line broadening analysis have been used in the past to study cyclic plasticity and how radial broadening differs with respect to monotonic loading [83]. However, these real-time measurements of the tension/compression oscillations observed in Figure 2.7 should create questions regarding a strong link between the radial FWHM and dislocation density during cyclic plasticity conditions; can dislocation density truly increase then decrease cycle after cycle? Increases can also be seen in the radial FWHM values for many peaks when the strain amplitude is increased to 0.5%. However, some peaks don't seem to change at all with loading "direction" or strain amplitude (e.g. grain 4, reflection #4). There are definite differences in the radial FWHM trends with *hkl*. Some of these have to do with the radial geometry of

diffraction, in general, others could be a result of real *hkl*–related differences i.e. decrease in the intensity of higher ordered peaks. We only accumulated three cycles at each strain amplitude so it will be important to understand the appearance of these distributions with many more cycles.

The azimuthal (η) FWHM values for each reflection at each load step are shown in Figure 2.8. These values are closely related to the spread of orientation across each of the grains; the azimuthal FWHM of each *hkl* can be thought of as a projection of the ODF within the grain. There is a distinct difference between the data from the 0.3% strain amplitude tests compared to those at 0.5%. The tension / compression differences are again apparent in these data - especially at 0.5%. However, all of the peaks in each grain experience a greater value of FWHM at the compressive end of the cycle. This results in each data set appearing "striped" as opposed to the checkered patterns observed in Figure 2.7.

To check the importance of loading "direction" on the azimuthal FWHM evolution, we conducted a subsequent 0.5% strain amplitude test on an identical OMC copper specimen beginning the loading in compression instead of tension. The question was, would the compression / tension azimuthal FWHM asymmetry persist with the loading reversed? A total of eight cycles were performed at a strain amplitude of 0.5%. In contrast to the tension-first experiment, the compression-first experiment exhibited larger azimuthal FWHM values in tension, not compression. The observation implies that the direction of initial loading (tension or compression) influences the FWHM oscillations at least in the first eight cycles. Questions that need to be addressed include: does this asymmetry shake down with increased number of cycles; are these effects the result of some initial condition in the material; if these asymmetries persist, are

they important to fatigue life?

2.8.2 Orientation, stress and plastic strain rate fields

Extracting the internal structure from the data is a fundamental challenge of diffraction data reduction and requires a model of the material - an estimate of the material structure based on the acquired diffraction data. Bragg's law and the Laue equation are examples of some of the earliest and certainly the most influential models of material structure based on diffraction. The work in this paper is motivated by the desire to understand the important details of the evolving grain scale micromechanical state that will eventually produce a fatigue crack within a cycling polycrystal. Crack initiation is strongly related to various manifestations of heterogeneity. We choose a crystal-based finite element model that is capable of very accurately representing the structural heterogeneity within a polycrystal but, more importantly, contains the constitutive fidelity to describe the evolving heterogeneity of micromechanically relevant fields such as stress, lattice orientation and plastic strain rate. The forward model or virtual diffractometer is the method we employ for comparing the experiment to the model. Once satisfactory agreement is established between the experimental data and model results, the finite element representation becomes a powerful hypothesis generation tool for extrapolating far beyond what is possible experimentally.

As an example of the comparisons that can be made between simulations and experiments, results from grain 2 are presented. Figure 2.9 presents components of the lattice strain tensor from grain 2. The normal components show

good comparison, while the shear strains show some deviation. Figure 2.10 provides radial and aziumthal FWHM data from grain 2. The values are close in magnitude and many of the general trends seen in the experimental data also appear in the simulation results. With the link between the azimuthal FWHM and slip-driven crystal re-orientation, this is a very important result. It basically demonstrates a level of consistency in the complex slip processes represented in the model and those responsible for the azimuthal broadening in the material. The model also predicts differences between tension and compression FWHM values for both radial and azimuthal distributions and we see the checkered patterns in the radial FWHM results similar to the experimental data. The striped pattern observed in the azimuthal FWHM experimental data are not present in the simulated data, however. Looking row by row, it appears that the azimuthal FWHM are well captured in tension by the model, but the higher values for every peak seen in the experimental data in compression are not captured in the simulation. There appears to be asymmetry in each simulated FWHM value, but some *hkl* s are biased towards tension, others toward compression. The underlying cause of the azimuthal FWHM tension-compression asymmetry requires further investigation as does the differences between the model and experiment. Examining Figure 2.3, we see differences between the macroscopic stress-strain data from the model and the experiment at the reverse yield points in each cycle; the macroscopic yield asymmetry and elastic-plastic transition that is a characteristic in many hysteresis loops is not well-captured by the model. Such loading path dependent behavior is often modeled phenomenologically on the macroscale using kinematic hardening and/or multi-surface plasticity models [52, 53]. Such a model could be implemented rather simply by introducing a "backstress" in addition to the slip system hardening equation (Equation 2.13)

[16]. However, other options more directly related to the actual shearing rates experienced by the slip systems within each crystal can now be explored using the FWHM data. The more important point to emphasize here is that the FWHM results represent fundamentally **new** cyclic plasticity data from every crystal within the aggregate and the virtual diffractometer represents a fundamentally **new** method for comparing model results to experimental data to improve our understanding of crystal scale plasticity processes.

The lattice orientation, von Mises effective stress and the effective plastic strain rate fields, as calculated from the finite element data, for grain 2 at +0.5% on the final cycle are shown in Figure 2.11. From an experimental perspective, these data are the result of the final step in the data reduction process. The heterogeneity in these fields is immediately obvious. There are regions in grain 2 that remain at the initial orientation and there are other regions that have rotated almost one degree. This is all during straining that never exceeded 0.5%. Most of the large values occur near the grain boundary but some interior regions with large misorientations exist as well. The fact that these rotations are reasonable is verified by examining the comparison between the azimuthal FWHM values in Figure 2.10. With the connection between lattice (elastic) strain and the crystal stress, the accuracy of the von Mises stress computed for each crystal is directly related to the radial FWHM comparison in Figure 2.10. Highly stressed regions occur on the boundary and within the interior and the large values of stress may or may not coincide with regions of high plastic strain rate. This makes sense in that regions within a grain that experience large stresses may be constrained in a way that prevents plastic flow. In the end, it will take the simultaneous examination of all three fields (and possibly some others) locally within a grain to understand the processes that lead to the initiation of a microcrack.

2.9 Summary / Conclusions

A methodology for understanding material evolution under cyclic plasticity conditions related to fatigue was presented. A coupled approach was developed, which employs a combination of high energy x-ray diffraction (HEXD) data and finite element simulation results to create a comprehensive picture of the deformation processes occurring within individual grains inside a deforming polycrystalline aggregate. The experimental data consists of diffracted intensity distributions obtained from individual crystals during cyclic deformation of a polycrystalline sample. The centroids (COM) and full width at half maximum (FWHM) values relative to the detector coordinates 2θ and η, were used to illustrate the richness of the diffraction data and its potential. Changes in 2θ and η for a peak are known to be related to the evolution of the strain and orientation distributions, respectively, within the crystal producing that peak.

An OMC copper specimen was cycled at two strain amplitudes, 0.3% and 0.5%. Four crystals with orientations spread over the stereographic triangle were analyzed by conducting HEXD experiments at several points during the loading history. Each crystal exhibited distinct behaviors. The 2θ and η COM values are related to the evolving grain-averaged lattice strain tensor and average lattice orientation within each grain, respectively. Both evolved significantly between tension and compression portions of the cycles. The FWHM values of 2θ and η, which are related to heterogeneity of lattice strain and orientation, respectively, also evolved with cycling, having different values in tension as compared to compression. The FWHM values measured for η were consistently larger at the compression end of the cycles for all grains. This trend switched when the cyclic loading was initiated in compression instead of tension.

The finite element results for one grain were compared to the experimental COM and FWHM data using the virtual diffractometer methodology. It was seen that key aspects of the complex slip mechanisms that take place within the crystal were consistent between experiment and model. The model predicted the tension/compression asymmetry of the FWHM values seen in the data but didn't always agree with the larger azimuthal FWHM values seen in the experimental data in compression. The source of the tension/compression asymmetries is not well understood, nor is its longevity with cycling or importance to the microcrack initiation process. Finally, the stress, orientation and plastic strain rate fields within one grain as predicted by the finite element model were shown. Significant heterogeneity was observed in all three fields with interesting points of mutual maximum and minimum values also observed. These results demonstrate the utility of the methodology for understanding heterogeneous nature of grain-scale deformation. The application of the research and its ultimate goal is a theory for microcrack initiation in ductile polycrystals.

CHAPTER 3

OBSERVING STRUCTURAL HETEROGENEITY WITHIN A POLYCRYSTAL DURING CYCLING USING HIGH ENERGY X-RAY DIFFRACTION AND THE IMPLICATIONS FOR CRYSTAL SCALE MODELS

3.0.1 Abstract

Developing a fundamental understanding of the early stages of fatigue crack initiation within ductile metals will require novel experimental tools capable of monitoring changes in structural heterogeneity during deformation. Emerging synchrotron high-energy x-ray diffraction (HEXD) techniques coupled with advanced data analysis approaches provide *in situ* quantitative measures of grain scale orientation and strain heterogeneity from a deforming polycrystalline aggregate. HEXD measurements were collected from oxygen free high conductivity copper and a copper alloy containing precipitates as they were cycled at fixed strain amplitude. The data revealed non-intuitive micro-mechanical behavior during cycling, along with drastic differences in the response of the two materials. The crystal plasticity formulation, initially not capturing the intricate micro-mechanical response or each grain, was extended to incorporate an anisotropic slip system hardening model. Results from the newly implemented hardening model reveal closer agreement with experimental data, however, further material-dependent enhancements may be warranted if grain scale comparison is desired between experiment and simulations.

3.1 Introduction

Fatigue crack initiation generally represents the longest, yet most poorly understood portion of a component's fatigue life. While a robust fatigue crack initiation theory has not emerged, some important trends have surfaced from crack initiation experiments conducted over the past century. Within the low-cycle fatigue regime, heterogeneous plasticity has consistently played a role in microcrack initiation within ductile metals. Ewing observed that deformation was concentrated within 'slip-bands' of cyclically loaded polycrystalline Swedish iron and that cracks would eventually develop within these bands if material cycling continued [23]. Thompson studied single crystal samples oriented for single slip (SCSS) and popularized persistent slip bands (PSBs): regions of localized slip which remain visible even after electropolishing [73]. The simple, uniaxial crystal stress state that produced slip primarily on one slip system allowed researchers to formally connect the location of PSBs to crack initiation sites in SCSS specimens [25, 55, 5, 29, 56, 58, 43, 8, 4]. Investigations of polycrystalline samples challenged the concise model of crack initiation for SCSS specimens, where crystal scale anisotropic properties combined with the need to simultaneously satisfy compatibility and equilibrium produce nonuniform, multiaxial stress states across grains [20, 46, 85].

The early work employing optical microscopy, to track the appearance of heterogeneous structure on the surfaces of samples, lacked the ability to observe internal microstructural evolution [25, 88, 5]. The development of transmission electron microscopy (TEM) allowed researchers to study the formation of dislocation structures within cyclically deformed materials and has enabled the development of theories of cyclic strain hardening, PSB formation, and microcrack

initiation [36, 10, 6]. Nonetheless, the bulk of TEM micrographs are made from post-mortem thin foils from small regions within individual crystals. Due to its inability to study bulk samples *in situ*, TEM's potential for enabling the kind of understanding that is necessary for a comprehensive fatigue crack initiation theory is on its own limited.

During the last decade, advances in high energy X-ray diffraction (HEXD) techniques [65] have redefined the way structural materials are characterized [54]. Modern x-ray techniques provide an opportunity to observe the non-homogeneous deformation within each grain of a polycrystal using *in situ* loading. In earlier work we showed that diffraction peaks continuously increased in size as a copper sample was deformed monotonically into the plastic regime [86]. This increasing peak size was connected to the growing inhomogeneity of orientation and lattice strain within each grain. Throughout the rest of this work "structural heterogeneity" references the deformation induced heterogeneity of lattice plane orientation and lattice strain.

In contrast to the monotonic loading experiment, the size of diffraction peaks does not continually increase with additional inelastic deformation during fully-reversed cyclic loading. The diffraction peaks actually *contract* during the excursion from one end of the hysteresis loop to the other, meaning that the underlying distributions of lattice orientation and strain become *less heterogeneous* with non-zero elastic-plastic straining [60]. The experimentally measured azimuthal full width at half maximum (FWHM) of diffraction peaks were consistently larger in compression when compared to tension when cycled under fixed strain amplitude. Simulations coupled with a virtual diffractometer captured the observed asymmetry in peak size between tension and compression,

however, not every diffraction peak indicated larger heterogeneity of orientation and strain in compression as observed experimentally [85].

The current work examines samples of a copper alloy containing precipitates and oxygen free high conductivity (OFHC) copper. The two materials are similar in terms of grain size and orientation distribution, however, their strain hardening behaviors differ due to presence of precipitates in the copper alloy. These two materials serve as prime examples to investigate the correlation between slip system hardening and deformation induced grain-scale heterogeneity of orientation and strain. Each material is cyclically deformed between tension and compression while performing HEXD measurements. A portion of the copper alloy experiment is simulated using an elasto-viscoplastic crystal plasticity model. The simple, isotropic slip system hardening assumption is extended to incorporate anisotropic slip system hardening into the formulation, i.e., the 12 primary slip systems of are allowed to harden at different rates. Variations of the anisotropic hardening model are implemented to investigate their effect on the development of intragrain heterogeneous deformation during plastic cycling. The experimental and simulation data are then discussed within the context of the kinematics and governing equations.

3.2 Experimental Methods

3.2.1 High energy x-ray diffraction experiments

Copper is a well studied, ductile metal generally accompanied with a relatively simple initial microstructure. Polycrystalline samples made from oxygen free

high conductivity (OFHC) copper and Okegawa mold copper (OMC) were mechanically cycled at the Advanced Photon Source 1-ID beamline. OMC is copper alloy containing precipitates composed of chromium (0.5 wt.%) and zirconium (0.02 wt.%), exhibiting a relatively high yield strength. OFHC copper, on the other hand, begins in an annealed state, exhibiting a low strength prior to strain hardening. Both materials display a uniform orientation distribution function and an average grain size of about 60 - 70 μm as shown in the electron backscatter diffraction (EBSD) orientation maps of Figure 3.1. Samples had a 9 mm long gage section with a 2 mm x 2 mm square cross-section within the gage region.

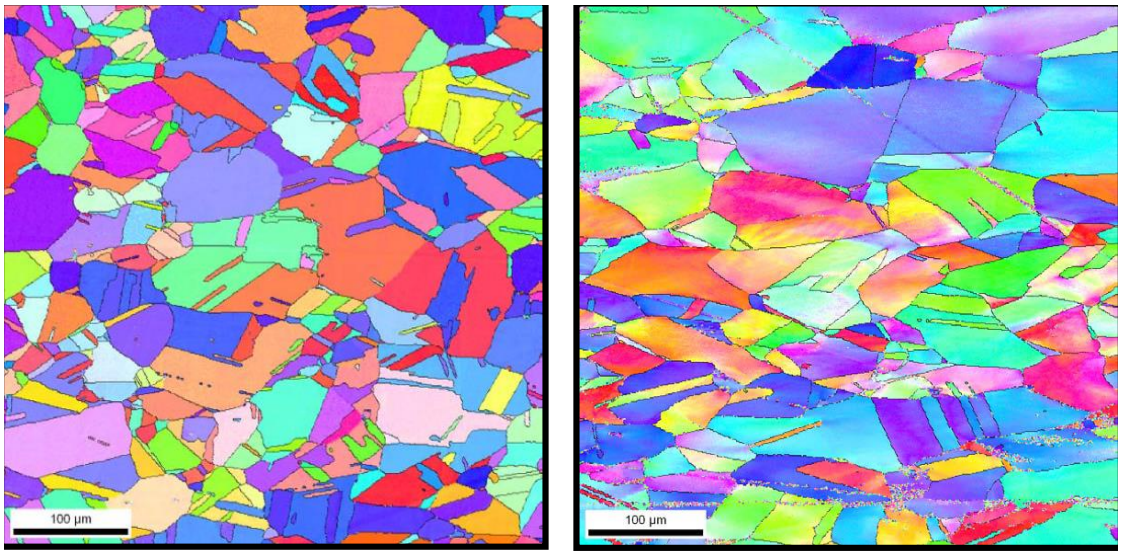

Figure 3.1: EBSD orientation maps for the (Left) OMC alloy and (Right) OFHC copper. Different colors represent unique orientations.

The HEXD rotating crystal method, coupling the far-field[1] experimental geometry and the GE area detector is depicted in Figure 3.2. Combining a monochromatic x-ray beam (80.725 keV) with the far-field geometry provides crystal strain and orientation resolution. During an x-ray measurement, the en-

[1]The sample to detector distance is on the order of 1 meter during a far-field experiment.

tire sample is rotated about the loading axis to bring various lattice planes into the diffraction condition. Meanwhile, the GE area detector is synchronized with the rotation such that each detector image records the integrated intensity for an increment of rotation, $\Delta\omega$. The macroscopic load is reduced to 90% of the peak load during HEXD measurements to minimize microstructural evolution during data acquisition. The x-ray beam had a size of 400 x 400 microns during each experiment.

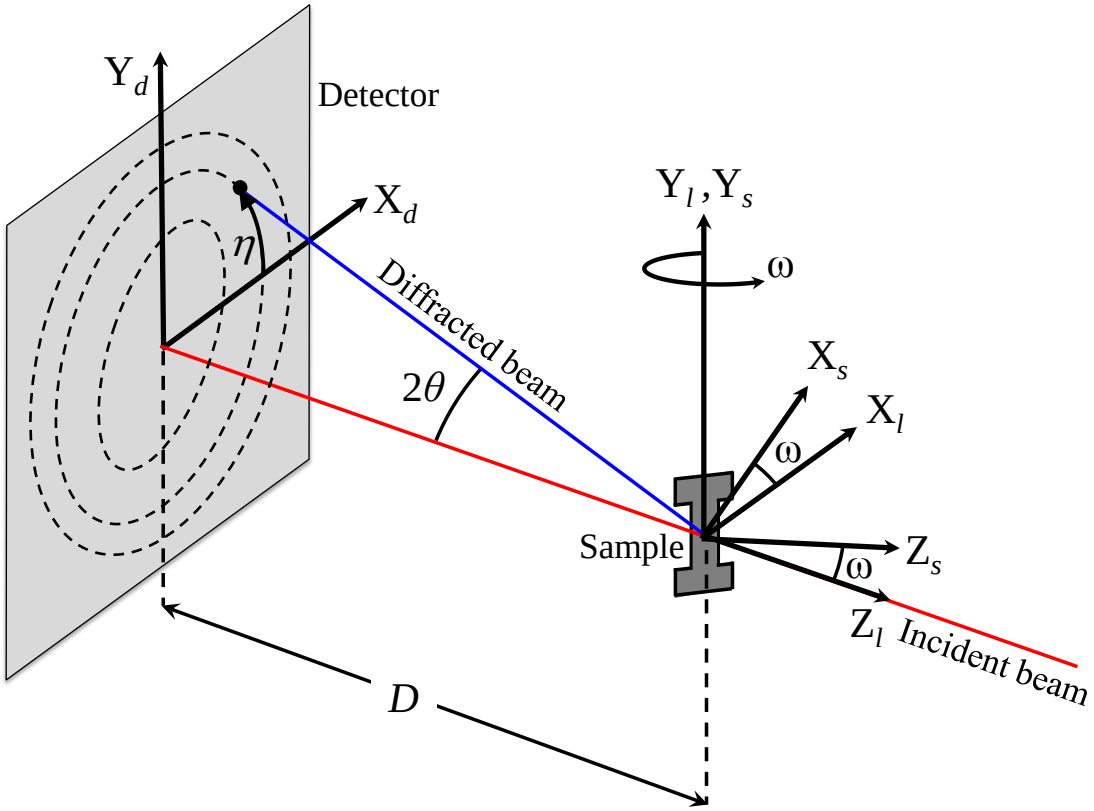

Figure 3.2: Schematic of the HEXD experimental setup. The laboratory coordinate system, $\{\mathbf{X}_l, \mathbf{Y}_l, \mathbf{Z}_l\}$, is fixed while the sample coordinate system, $\{\mathbf{X}_s, \mathbf{Y}_s, \mathbf{Z}_s\}$, rotates about the loading axis by angle ω. Points on the detector can be described using its rectangular coordinate system, $\{\mathbf{X}_d, \mathbf{Y}_d\}$ or a "polar" coordinate system, $\{2\theta, \eta\}$. The angles 2θ and η correspond to the Bragg angle and the azimuthal angle respectively. The sample to detector distance, D, was about 1 m for each experiment.

3.2.2 Connecting diffraction peak spreading with structural heterogeneity

Plastic deformation of a polycrystal generally results in heterogeneous deformation fields across each grain [20, 46, 85]. Introducing spatial gradients of lattice plane spacing (strain) and orientation into individual grains causes the diffraction peaks to spread on an area detector. This connection between distributions of x-ray diffracted intensity and plastic deformation is well-documented for both monochromatic and polychromatic x-ray measurements [34, 40, 59, 81, 78, 84, 76, 77, 79]. Just as nonlinearity in the macroscopic stress-strain response serves as a sign of plastic deformation of a macroscopic sample, diffraction peak shape change serves as the microscopic indicator of heterogeneous structure within grains. Some peaks spread significantly, others very little, depending on the orientation of the lattice planes associated with the peak (*hkl*) relative to the active plastic slip plane(s) [62, 63]. Azimuthal spreading on the detector is dominated by the plastically-generated heterogeneity of orientation within a crystal, while radial spreading is the result of heterogeneous straining of a crystal [85].

3.2.3 Diffraction peak analysis

Roughly 100 diffraction events intersect the detector plane for each grain throughout the full rotation of the sample. The orientations of grains within the sample are unknown a priori, so data reduction begins by indexing - associating the various diffraction peaks with unique grain orientations within the diffraction volume [13]. Once indexed, diffraction peak fitting proceeds as depicted in

Figure 3.3. Each peak is integrated twice, first in the radial direction and then, in a separate operation, the azimuthal direction [60]. The integration collapses a peak into two, two-dimensional profiles: 1) intensity versus azimuthal angle, η, and 2) intensity versus radial angle, 2θ. Each of these two-dimensional profiles is fit using a split pseudo-Voigt function to determine the center of mass (COM) and the full width at half maximum (FWHM) values. Collectively, the 2θ COM values for each grain are utilized to calculate the grain's average lattice (elastic) strain tensor, a procedure documented in [13].

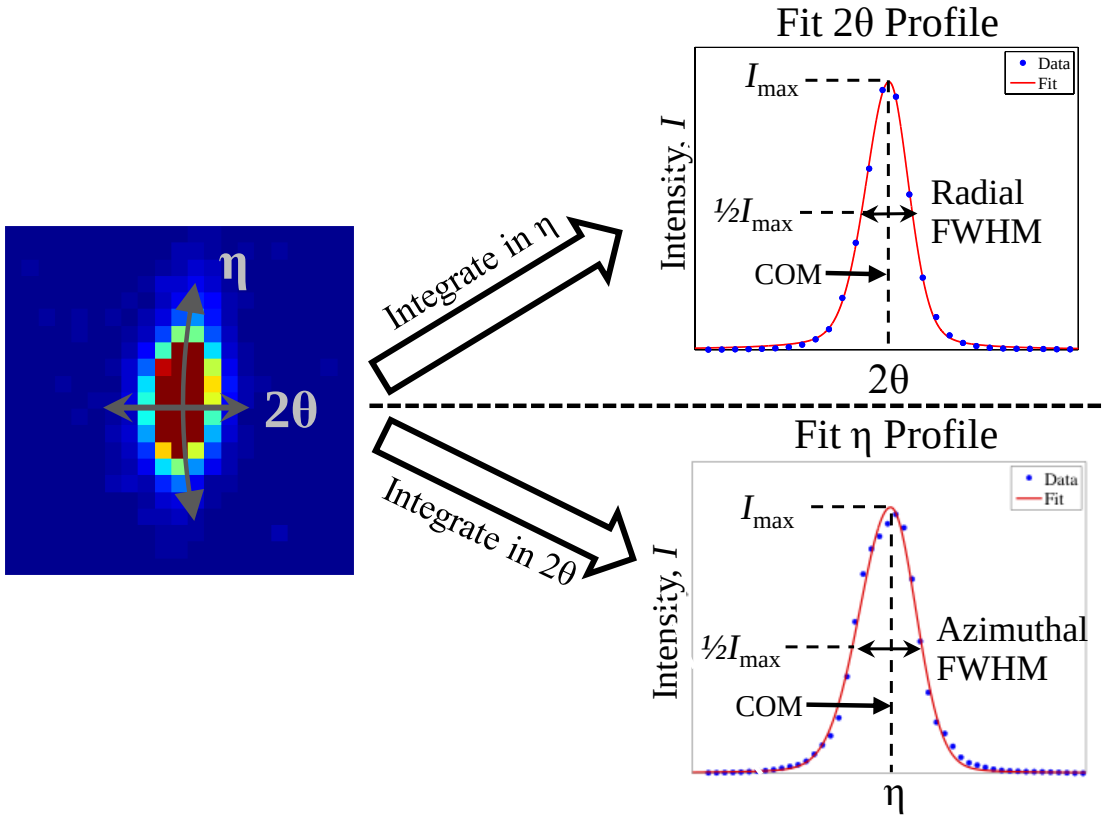

Figure 3.3: Schematic of the diffraction peak fitting procedure used to measure the radial and azimuthal COM and FWHM values of each peak [60].

Increases in the heterogeneity of orientation within a grain (misorientation)

are directly captured within its azimuthal peak widths, therefore, we develop an x-ray diffraction based misorientation metric. The azimuthal FWHM value at the first x-ray measurement corresponding to the undeformed state, $(\eta_0^{FWHM})_n$, is subtracted from the i^{th} measurement, $(\eta_i^{FWHM})_n$, for each diffraction peak n of a grain.

$$(\Delta\eta_i^{FWHM})_n = (\eta_i^{FWHM})_n - (\eta_0^{FWHM})_n \tag{3.1}$$

These differences are then averaged across all of a grain's, N, diffraction peaks.

$$\zeta = \frac{1}{N}\sum_{n=1}^{N}(\Delta\eta_i^{FWHM})_n \tag{3.2}$$

The misorientation metric, ζ, effectively collapses the collective information contained within all peaks for *one* grain. This calculation is repeated for every grain at each x-ray measurement point during the experiment. Similarly a metric is developed for the radial, 2θ, broadening of diffraction peaks characterizing the distribution of lattice plane spacing (strain) within each grain.

$$(\Delta 2\theta_i^{FWHM})_n = (2\theta_i^{FWHM})_n - (2\theta_0^{FWHM})_n \tag{3.3}$$

$$\Theta = \frac{1}{N}\sum_{n=1}^{N}(\Delta 2\theta_i^{FWHM})_n \tag{3.4}$$

Increases in ζ and Θ indicate growing misorientation and strain heterogeneity respectively, while decreases can be interpreted as a return towards the initial state. Condensing all of the diffraction peaks from each grain into two quantities, ζ and Θ, ignores the individual character inherent in a diffraction peak, since each peak is itself a unique projection of the structure within a grain [62].

Homogenizing all of the peaks and presenting a single scalar value neglects the true depth of available data, but allows us to simultaneously compare the behaviors of numerous grains across multiple HEXD measurements. The lattice heterogeneity metrics, ζ and Θ, enable a grain by grain comparison of every grain within the diffraction volume.

3.3 Simulation Methods

This section outlines the anisotropic, elasto-viscoplastic crystal-scale finite element formulation. We focus our attention on the hardening equations within the crystal plasticity constitutive model to determine the impact of various slip system hardening assumptions on the resulting structural heterogeneity. Simulations incorporating both isotropic and anisotropic hardening conditions are investigated. A detailed description of the crystal plasticity model is found within [19, 51, 50].

3.3.1 Crystal Kinematics and Slip Kinetics

Motion of a material point is described through a decomposition of the deformation gradient, $\mathbf{F}$, into plastic slip, $\mathbf{F}^p$, a rigid body rotation, $\mathbf{R}^*$, and an elastic stretch, $\mathbf{V}^e$.[2]

$$\mathbf{F} = \mathbf{V}^e \, \mathbf{R}^* \, \mathbf{F}^p \tag{3.5}$$

[2]Vectors and second-order tensors are indicated with bold face lower and upper case letters, respectfully. The vector outer product of two vectors, $\mathbf{a}$ and $\mathbf{b}$, is indicated as $\mathbf{a} \otimes \mathbf{b}$ while the trace of a second order tensor $\mathbf{A}$ is denoted as tr($\mathbf{A}$).

The kinematic decomposition of $\mathbf{F}$ is expressed schematically in Figure 3.4. Each portion of the decomposition moves the material point to a new configuration, starting from the reference configuration $\mathcal{B}^0$ through to the current configuration, $\mathcal{B}$. The intermediate configuration, $\hat{\mathcal{B}}$ represents a stress-free configuration. The velocity gradient, $\mathbf{L}$, calculated as the time-rate-of-change of $\mathbf{F}$, is written as,

$$\mathbf{L} = \dot{\mathbf{F}}\,\mathbf{F}^{-1}. \tag{3.6}$$

Further decomposition expresses $\mathbf{L}$ as the sum of the rate of deformation, $\mathbf{D}$, (symmetric portion of $\mathbf{L}$) and the spin, $\mathbf{W}$ (skew portion of $\mathbf{L}$).

$$\mathbf{L} = \mathbf{D} + \mathbf{W} \tag{3.7}$$

The model assumes small elastic strains, $\mathbf{e}^e$, allowing the elastic stretch to be rewritten as,

$$\mathbf{V}^e = \mathbf{I} + \mathbf{e}^e \tag{3.8}$$

where $\mathbf{I}$ is the identity matrix. The elastic response is governed by Hooke's law.

$$\tau = \mathbf{C}(\mathcal{R})\,\mathbf{e}^e \tag{3.9}$$

The stiffness matrix, $\mathbf{C}$, is a function of the crystal orientation, $\mathcal{R}$. Substitution of Equation 3.5 into Equation 3.6 and separating out the deviatoric portion yields:

$$\mathrm{tr}(\mathbf{D}) = \mathrm{tr}(\dot{\mathbf{e}^e}) \tag{3.10}$$

and

$$\dot{\mathbf{e}^e} = \mathbf{D}' - (\hat{\mathbf{D}}^{p\prime} + \mathbf{e}^{e\prime}\hat{\mathbf{W}}^p - \hat{\mathbf{W}}^p\mathbf{e}^{e\prime}) \tag{3.11}$$

where primes ($'$) indicate the deviatoric portion of the tensor they accompany. The plastic spin is expressed as:

$$\hat{\mathbf{W}}^p = \mathbf{W} - (\mathbf{e}^{e\prime}\hat{\mathbf{D}}^{p\prime} - \hat{\mathbf{D}}^{p\prime}\mathbf{e}^{e\prime}) \tag{3.12}$$

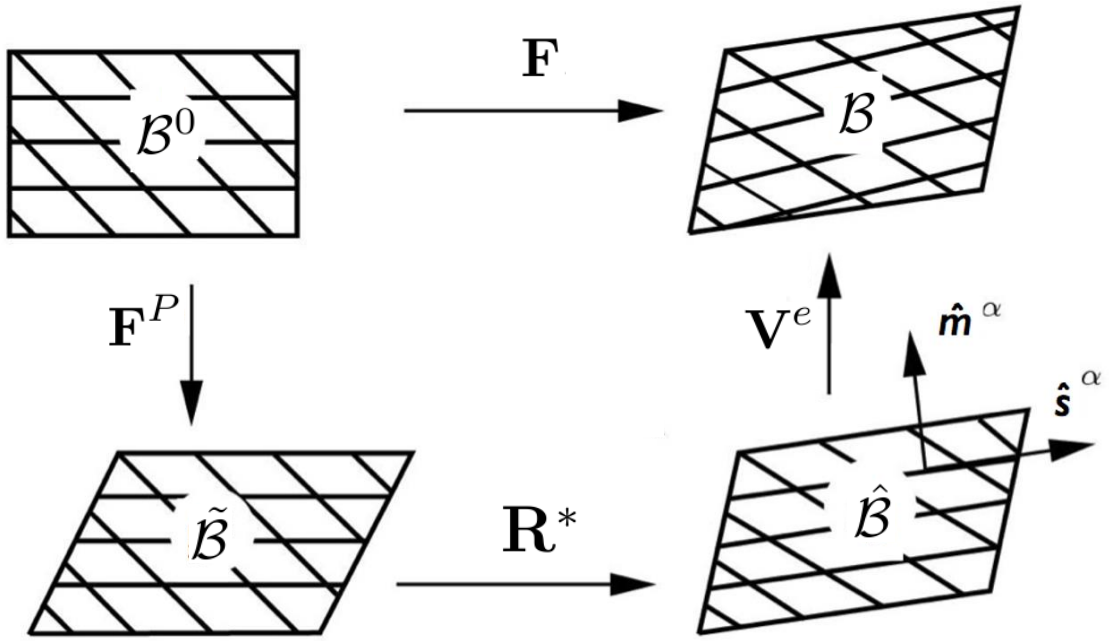

Figure 3.4: Kinematic decomposition of the deformation gradient, **F**, into plastic slip $\mathbf{F}^P$, lattice rotation, $\mathbf{R}^*$, and elastic stretch, $\mathbf{V}^e$. The material point advances from the reference configuration, $\mathcal{B}^0$, through the intermediate configurations, $\tilde{\mathcal{B}}$ and $\hat{\mathcal{B}}$, to the current configuration, $\mathcal{B}$.

where the plastic spin, $\mathbf{W}^p$, and the plastic deformation rate, $\mathbf{D}^{p\prime}$, are mapped to $\hat{\mathbf{W}}^p$ and $\hat{\mathbf{D}}^{p\prime}$ using $\mathbf{R}^*$ in accordance with Figure 3.4.

Plastic deformation is accommodated through slip on the twelve {111}<110> crystal slip systems. The plastic shearing rate on the j^{th} slip system, $\dot{\gamma}_j$, is expressed in a power law form:

$$\dot{\gamma}_j = \dot{\gamma}_0 \left(\frac{\tau_j}{g_j} \right)^{1/m} \operatorname{sgn}(\tau_j) \tag{3.13}$$

where $\dot{\gamma}_0$ and m are material constants, τ_j is the resolved shear stress, and g_j is the

slip system strength of the j^{th} slip system. Slip system strengthening equations are provided in Section 3.3.2.

The plastic deformation rate is a function of the slip system shearing rates and the symmetric portion of the Schmidt tensor.

$$\hat{\mathbf{D}}^{p'} = \sum_{\alpha=1}^{12} \dot{\gamma}^{\alpha} (\hat{\mathbf{s}}^{\alpha} \otimes \hat{\mathbf{m}}^{\alpha})_S \tag{3.14}$$

The lattice orientation, $\mathbf{R}^*$, is updated as follows,

$$\dot{\mathbf{R}}^* = \Big(\hat{\mathbf{W}}^P - \sum_{\alpha=1}^{12} \dot{\gamma}^{\alpha} (\hat{\mathbf{s}}^{\alpha} \otimes \hat{\mathbf{m}}^{\alpha})_A \Big) \cdot \mathbf{R}^* \tag{3.15}$$

where $(\hat{\mathbf{s}}^{\alpha} \otimes \hat{\mathbf{m}}^{\alpha})_A$ is the antisymmetric (skew) portion of the Schmidt tensor.

3.3.2 Slip System Hardening

The simplicity of implementing an anisotropic hardening model into an already existing isotropic framework is quite appealing, since the need to solve additional global solutions or an expanded boundary value problem is not required. Anisotropic hardening is incorporated through a modification of the Voce hardening law,

$$\dot{g}_i = h \Big(\frac{g_s(\dot{\gamma}) - g_i}{g_s(\dot{\gamma}) - g_0} \Big)^n \sum_{j=1}^{12} \hbar_{ij} \mid \dot{\gamma}_j \mid \tag{3.16}$$

where $\hbar$ is the interaction matrix and i denotes slip systems. The saturation strength is defined as,

$$g_s(\dot{\gamma}) = g_{s0} \Big(\frac{\sum \| \dot{\gamma}_j \|}{\dot{\gamma}_{s0}} \Big)^{m'} \tag{3.17}$$

where g_{s0}, $\dot{\gamma}_{s0}$, and m' are material constants.

The interaction matrix was first defined by Kocks in [39] to include slip interactions among any of the primary slip systems of an FCC crystal. The matrix is

simplified here to only allow interactions between coplanar slip systems. Coefficients for all other slip interactions are equal to zero and left blank in $\hbar$ below.

$$[\hbar] = \begin{bmatrix} d & h & h & & & & & & & & & \\ h & d & h & & & & & & & & & \\ h & h & d & & & & & & & & & \\ & & & d & h & h & & & & & & \\ & & & h & d & h & & & & & & \\ & & & h & h & d & & & & & & \\ & & & & & & d & h & h & & & \\ & & & & & & h & d & h & & & \\ & & & & & & h & h & d & & & \\ & & & & & & & & & d & h & h \\ & & & & & & & & & h & d & h \\ & & & & & & & & & h & h & d \end{bmatrix} \tag{3.18}$$

Within the interaction matrix, d is the diagonal coefficient and h is the slip family coefficient. Hardening of a slip system due to its own straining is termed *direct* hardening, while hardening of a slip system due to straining of another slip system is termed *latent* hardening. Setting d equal to one or zero turns direct hardening on or off respectively. Making h nonzero will invoke latent hardening of the coplanar slip systems, where the magnitude of h can be either larger or smaller than unity. Populating the entire interaction matrix with ones, including blank values, would result in isotropic hardening.

Comparing the anisotropic hardening model provided in Equation 3.16 to the isotropic hardening equation below highlights the differences between the

hardening assumptions.

$$\dot{g} = h\Big(\frac{g_s(\dot{\gamma}) - g}{g_s(\dot{\gamma}) - g_0}\Big)^n \sum_{j=1}^{12} |\dot{\gamma}_j| \tag{3.19}$$

Every slip system, j, within the isotropic formulation shares the same strength ($g_j = g$) and slip system hardening rate ($\dot{g}_j = \dot{g}$).

This brief summary of the crystal plasticity model is by no means comprehensive. Rather the goal is to highlight the deformation kinematics and the equations governing crystallographic slip and rotation of each element. The slip system strengths, g_j, and the lattice orientation, $\mathbf{R}^*$ are the two state variables updated at every element during deformation. Azimuthal diffraction peak broadening originates from nonuniform rotation of the crystal lattice, i.e., a distribution of $\mathbf{R}^*$ values across a single grain, while radial broadening is the result of nonuniform strain, $\mathbf{e}^e$. Equation 3.15 reveals that $\dot{\mathbf{R}}^*$, the rate of rotation of the crystal lattice, is coupled to the slip system shearing rates, $\dot{\gamma}_j$. The strengthening rate of each slip system, $\dot{g}_j$, is also a function of $\dot{\gamma}_j$. Modification of the hardening assumption will inherently alter the resulting lattice rotation of each element. This connection between lattice rotation and the slip system hardening equation, guides us to study the sensitivity of hardening assumptions on the resulting structural heterogeneity.

3.3.3 Simulation of Cyclic Loading Experiments

During our previous experiments, we tracked four specifically chosen grains within the polycrystal [60]. We shift our focus to the aggregate by experimentally tracking a volume of material containing hundreds of grains. The virtual cube with 1 mm side lengths contains 500 grains, so that the nominal grain

size within the simulations mimicked the OMC alloy. The finite element mesh was instantiated through the Poisson-Voronoi tessellation algorithm within the Neper software package [67]. Every grain is discretized into thousands of elements such that spatial variation of orientation and strain is captured across each grain. The material exhibits little texture, therefore, each grain was assigned an orientation by sampling a random distribution of orientations. Slip system parameters were determined by matching the simulation macroscopic stress-strain response with the experimental curve [85]. Table 3.1 compiles all of the slip system parameters for OMC, and the single crystal elastic constants for copper [31]. Each simulation deformed the virtual aggregate at a strain amplitude of 0.3% for one tension-compression cycle.

C_{11}	C_{12}	C_{44}	h_0 (MPa)	g_0 (MPa)	g_{s0} (MPa)	m	m′	$\dot{\gamma}_0$ (s^{-1})	$\dot{\gamma}_{s0}$ (s^{-1})
164	122	75	800	85	285	0.01	0.0	1.0	5×10^{10}

Table 3.1: Single crystal elastic constants for copper employed in the simulations in units of GPa, along with the elasto-viscoplastic model constants used for OMC copper. Values for h and d are provided in Table 3.2

Experimental studies have attempted to determine the relative strengths of interactions amongst slip systems [39, 26, 91]. Approaches utilizing dynamic dislocation simulations have sought the same goal [22, 21]. Three independent simulations with different interaction matrices are summarized in Table 3.2. Simulation 1 populates the entire interaction matrix with ones, invoking isotropic hardening. Simualation 2 sets d, the diagonal coefficient, to unity and h, the slip family coefficients, equal to 1.4. Selecting a value of h greater than unity makes coplanar slip systems strengthen at a faster rate than the active slip system. The choice of $h = 1.4$ falls in line with the experimental

Simulation	Description	d	h
1	Isotropic hardening	1	1*
2	Latent w/ direct hardening	1	1.4
3	Latent w/o direct hardening	0	1.4

*Note: The entire interaction matrix is populated with ones for isotropic hardening including blank values in Equation 3.18.

Table 3.2: Summary of finite element simulations and values for the diagonal coefficient, d, and the slip family coefficient, h, in the interaction matrix, $\hbar$, defined by Equation 3.18

measurements of Kocks [39]. The final simulation, Simulation 3 invokes latent hardening with no direct hardening. The parameters for the three simulations were chosen to span three extreme hardening assumtions within the anisotropic hardening framework.

3.3.4 Virtual diffractometer

HEXD measurements can be examined relative to crystal plasticity simulation results by juxtaposing the experimental results with synthetic diffraction data produced using a virtual diffractometer [86, 60, 85]. The finite element framework stores the state of each finite element as the sample is virtually deformed, including three dimensional fields of elastic strain and lattice orientation within each grain. Our goal is to compare to the experimentally measured x-ray diffraction metrics, ζ and Θ, to the simulated spatial strain and orientation fields. Unfortunately, the experimental data cannot be inverted to extract the spatial distribution of strain and orientation, however, we can projcect the simulation results through the virtual diffractometer. Each material point, having its own orientation and strain, serves as a unique diffraction volume to collectively produce synthetic detector images [86]. The diffraction peaks contained within

these synthetic images are analyzed using the same peak fitting procedure as the experimental images described in Section 3.2.3. Using this methodology, simulation and experimental diffraction peaks are directly compared using the diffraction metrics, ζ and Θ.

3.4 Results

In this current work, we observe the progression of deformation heterogeneity within OFHC copper and an OMC alloy during plastic cycling. The experimental results present similarities and differences between the two materials through the structural heterogeneity metrics, ζ and Θ, defined in Section 3.2.3. A series of crystal plasticity simulations are compared to the experiments via the virtual diffractometer. The simulations aim to identify the impact of anisotropic slip system hardening on the grain scale deformation heterogeneity.

3.4.1 Incremental step test on OMC alloy

An incremental step test was performed on an OMC alloy sample. The sample was first cycled at a 0.3% strain amplitude for three cycles and then an additional three cycles at a 0.5% strain amplitude as seen in Figure 3.5. Figure 3.5 plots the grain misorientation and strain distribution metrics, ζ and Θ, for every grain as the material is cycled between tension and compression for all six cycles. Every grain exhibits a compression asymmetry in misorientation, ζ, meaning grains contain more misorientation in compression when compared to tension. Collectively the grains produce a compression bias in misorientation

which begins on the first cycle and endures through all six cycles. A majority of the grains also exhibit a compression bias in strain distribution, Θ.

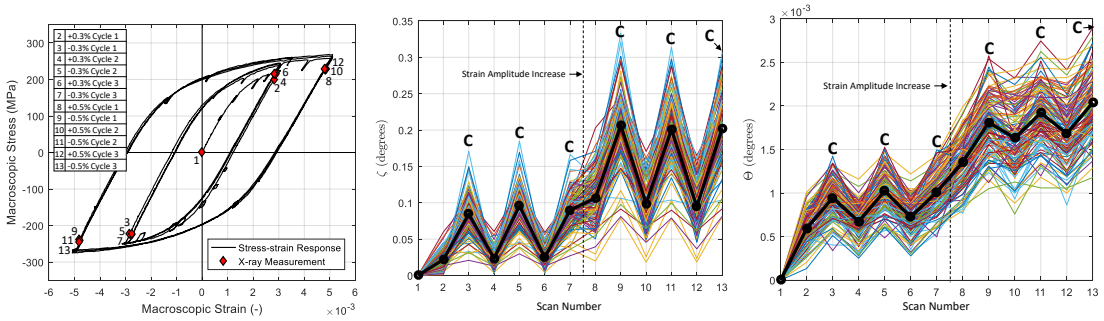

Figure 3.5: (Left) Stress-strain history for OMC alloy incremental step test. Sample was cycled for three cycles at 0.3% strain amplitude and then an additional three cycles at 0.5% strain amplitude. X-ray measurements points are labeled at the unloaded state and the tension and compression loop tips of each cycle. (Center) Misorientation metric, ζ, and (Right) strain distribution metric, Θ, plotted for each x-ray measurement point. Each line represents a unique grain, while the thicker line represents the grain-averaged value.

3.4.2 Reversing the cyclic loading direction

The compression biased misorientation and strain distribution observed during the incremental step test poses several questions: 1) will the compression bias reverse if loading begins in compression instead of tension and 2) will the bias disappear after a ”large” number of cycles? The incremental step test was repeated on a new but metallurgically ”identical” OMC alloy sample with initial sample loading occurring in compression instead of tension. Similar to the first experiment, the sample was first loaded at a fixed strain amplitude of 0.3% for three cycles. Afterwards, the strain amplitude was increased to 0.5% for an additional 16 cycles as show Figure 3.7. The misorientation, ζ, and strain distribu-

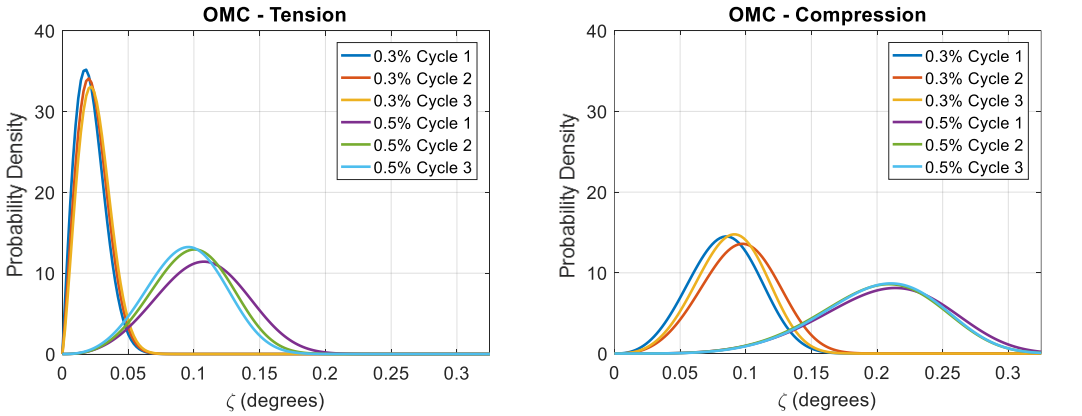

Strain Amplitude	Cycle #	Mean (degrees)	STD (degrees)
0.3%	Cycle 1	0.022	0.011
0.3%	Cycle 2	0.023	0.011
0.3%	Cycle 3	0.025	0.012
0.5%	Cycle 1	0.107	0.034
0.5%	Cycle 2	0.099	0.030
0.5%	Cycle 3	0.094	0.029

Strain Amplitude	Cycle #	Mean (degrees)	STD (degrees)
0.3%	Cycle 1	0.084	0.026
0.3%	Cycle 2	0.096	0.028
0.3%	Cycle 3	0.089	0.026
0.5%	Cycle 1	0.206	0.049
0.5%	Cycle 2	0.201	0.046
0.5%	Cycle 3	0.202	0.046

Figure 3.6: The misorientation metric, ζ, from each grain in Figure 3.5 has been replotted as Weibull distributions. Data measured at the tension tips of the hysteresis loops (Left) are plotted separately from the compression loop tips (Right). The accompanying mean and standard deviation of each distribution are provided.

tion, Θ, are plotted for each grain. Note that data are plotted for cycles 1 and 3 of the 0.3% strain amplitude and cycles 1, 8, and 16 of the 0.5% strain amplitude. Upon first glance, the plots of ζ in Figures 3.5 and 3.7 look largely the same. Close inspection reveals that the compression bias seen in Figure 3.5 has shifted to a tension bias in Figure 3.7. A majority of the grains now exhibit a tension bias in Θ as well after reversing the initial loading direction. The compression-first sample was cycled for 16 cycles at 0.5% strain amplitude instead of just three cycles for the tension-first sample, and consequently we observe more evolution in both ζ and Θ during cycling at the larger strain amplitude.

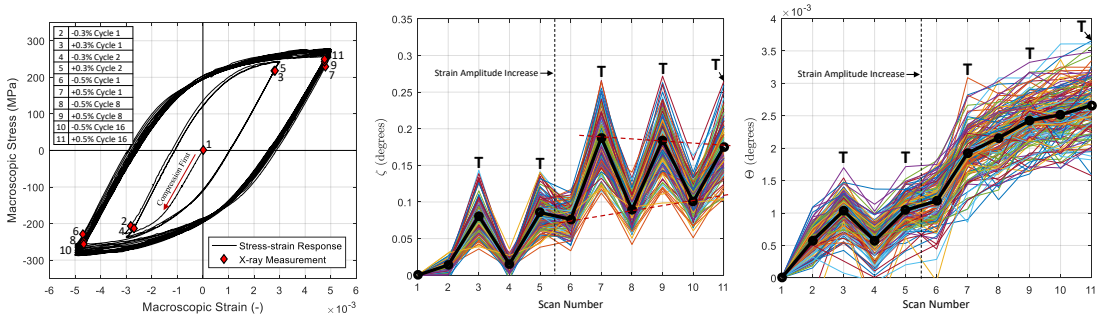

Figure 3.7: (Left) Stress versus strain history for the OMC alloy compression-first experiment. The sample was plastically cycled for three cycles at 0.3% strain amplitude and then for 16 cycles at 0.5% strain amplitude. X-ray measurements were taken at the loop tips on cycles one and three at 0.3% strain, and then on cycles 1, 8, and 16 at 0.5% strain amplitude. (Center) Misorientation metric, ζ_i, and (Right) strain distribution metric, ζ_i. Each individual line represents a unique grain, while the thicker line represents the average across all grains.

3.4.3 OFHC copper experiment

Focus is now redirected toward OFHC copper to make a comparison between the mechanical responses the of OFHC copper and OMC alloy. An OFHC copper sample was macroscopically loaded at a constant strain amplitude of 0.5% for 16 cycles as show in Figure 3.9. The evolution of misorientation, ζ, within the grains is plotted for cycles 1, 2, 4, 8, and 16. We see various amounts of tension/compression asymmetry, but unlike OMC alloy OFHC copper does not show a bias in misorientation between tension and compression during the first two cycles. Each grain individually exhibits an asymmetry in misorientation, but produces a value near zero when averaged across all grains. A distinct tension bias begins to develop after four cycles, and becomes clearly visible by cycle 16 when the material's strength is nearing saturation. The Θ plot depicts an increasing strain distribution within each grain as the sample is cycled. The deformation induced misorientation heterogeneity observed within the two ma-

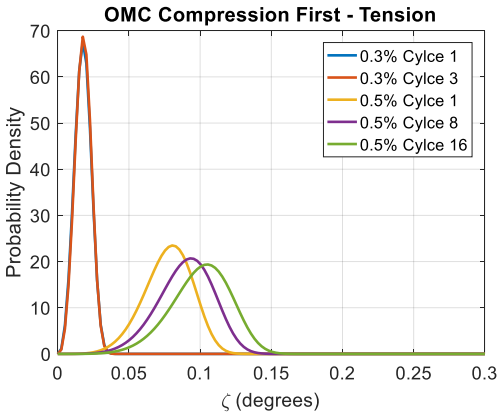

Strain Amplitude	Cycle #	Mean (degrees)	STD (degrees)
0.3%	1	0.018	0.006
0.3%	3	0.018	0.006
0.5%	1	0.077	0.017
0.5%	8	0.090	0.019
0.5%	16	0.100	0.021

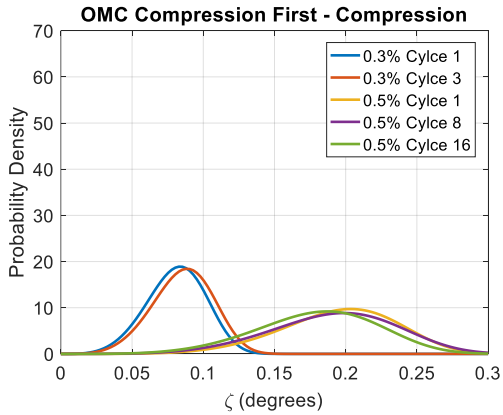

Strain Amplitude	Cycle #	Mean (degrees)	STD (degrees)
0.3%	1	0.081	0.021
0.3%	3	0.086	0.021
0.5%	1	0.195	0.041
0.5%	8	0.191	0.045
0.5%	16	0.180	0.043

Figure 3.8: The misorientation metric, ζ, from each grain in Figure 3.7 has been replotted as Weibull distributions. Data measured at the tension tips of the hysteresis loops (Left) are plotted separately from the compression loop tips (Right). The accompanying mean and standard deviation of each distribution are provided.

terials is drastically different in character. The OFHC copper eventually shows a tension biased misorientation while the OMC alloy showed a compression biased misorientation when loaded first in tension.

3.4.4 Impact of hardening assumptions

The misorientation bias is the focus of simulations due to its strong magnitude and direct link to slip activity. Additionally, the experimental data identified that the character of the misorientation bias was drastically different between the two materials. The simulations aim to test the sensitivity of the deformation induced misorientation heterogeneity, ζ, to the slip system hardening assump-

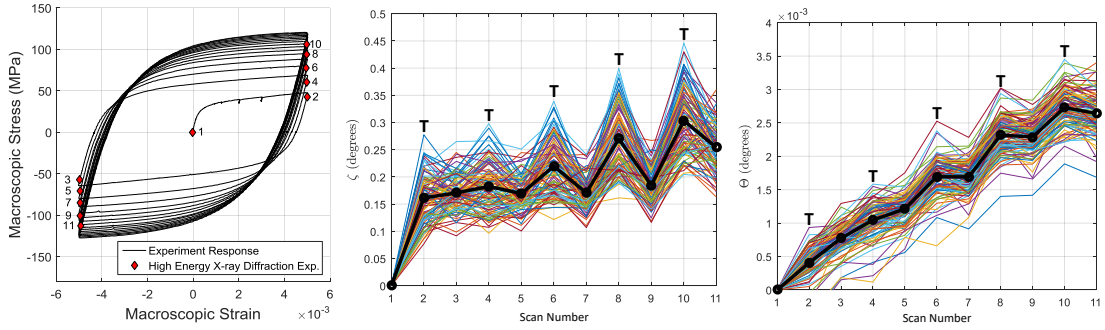

Figure 3.9: (Left) Stress versus strain history for the OFHC copper sample tested at fixed strain amplitude for 16 cycles. (Center) Misorientation metric, ζ_i, and (Right) strain distribution metric, ζ_i. Each individual line represents a unique grain, while the thicker line represents the average across all grains. X-ray measurements are labeled with points corresponding to the undeformed state and the tension-compression loop tips of cycles 1, 2, 4, 8, and 16.

tions. Figure 3.11 shows the stress-strain response for the three simulations described in Section 3.3 along with the first cycle of the incremental step test conducted on OMC alloy.

During the first cycle, several x-ray measurements were gathered in addition to the loop tips presented in previous plots. Points 1-9 depict the locations along the stress-strain response where data are available from both the experiment and simulations. Simulation data were postprocessed through the virtual diffractometer to generate synthetic detector images, and diffraction peaks were fit before calculating the misorientation metric, ζ. The results from this forward projection are plotted for the three simulations and for the OMC experiment in Figure 3.12.

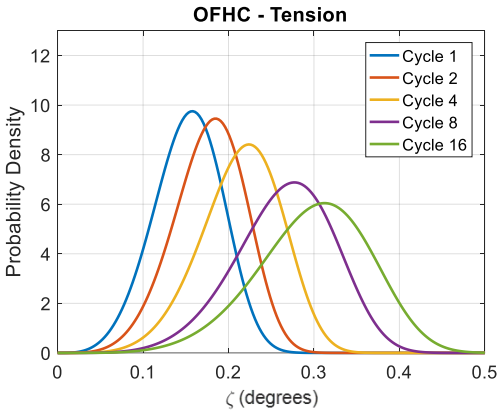

Strain Amplitude	Cycle #	Mean (degrees)	STD (degrees)
0.5%	1	0.153	0.040
0.5%	2	0.178	0.042
0.5%	4	0.215	0.047
0.5%	8	0.266	0.058
0.5%	16	0.299	0.066

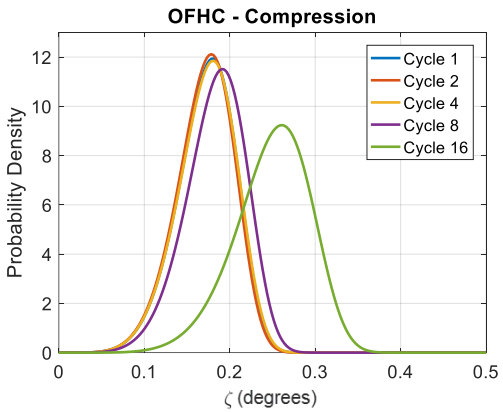

Strain Amplitude	Cycle #	Mean (degrees)	STD (degrees)
0.5%	1	0.172	0.034
0.5%	2	0.171	0.033
0.5%	4	0.173	0.034
0.5%	8	0.183	0.035
0.5%	16	0.249	0.044

Figure 3.10: The misorientation metric, ζ, from each grain in Figure 3.9 has been replotted as Weibull distributions. Data measured at the tension tips of the hysteresis loops (Left) are plotted separately from the compression loop tips (Right). The accompanying mean and standard deviation of each distribution are provided.

3.4.5 Grain-scale stress triaxiality and coaxiality

Stress multiaxiality plays a critical role in processes such as plasticity and fatigue, where deformation and failure criteria are often based upon the stress state. Many hypotheses regarding damage and crack nucleation identify regions of high stress or strain as potential initiation sites, especially in regions of high deformation heterogeneity [14]. We investigate the two materials further by examining the grain averaged strains extracted from the x-ray data. All strains are calculated relative to the initial state, and converted to stresses using Hooke's Law and the elastic constants shown in Table 3.1. Instead of presenting the six independent components of the stress tensor for each grain, we calculate two relevant metrics representing its magnitude and direction: the stress triax-

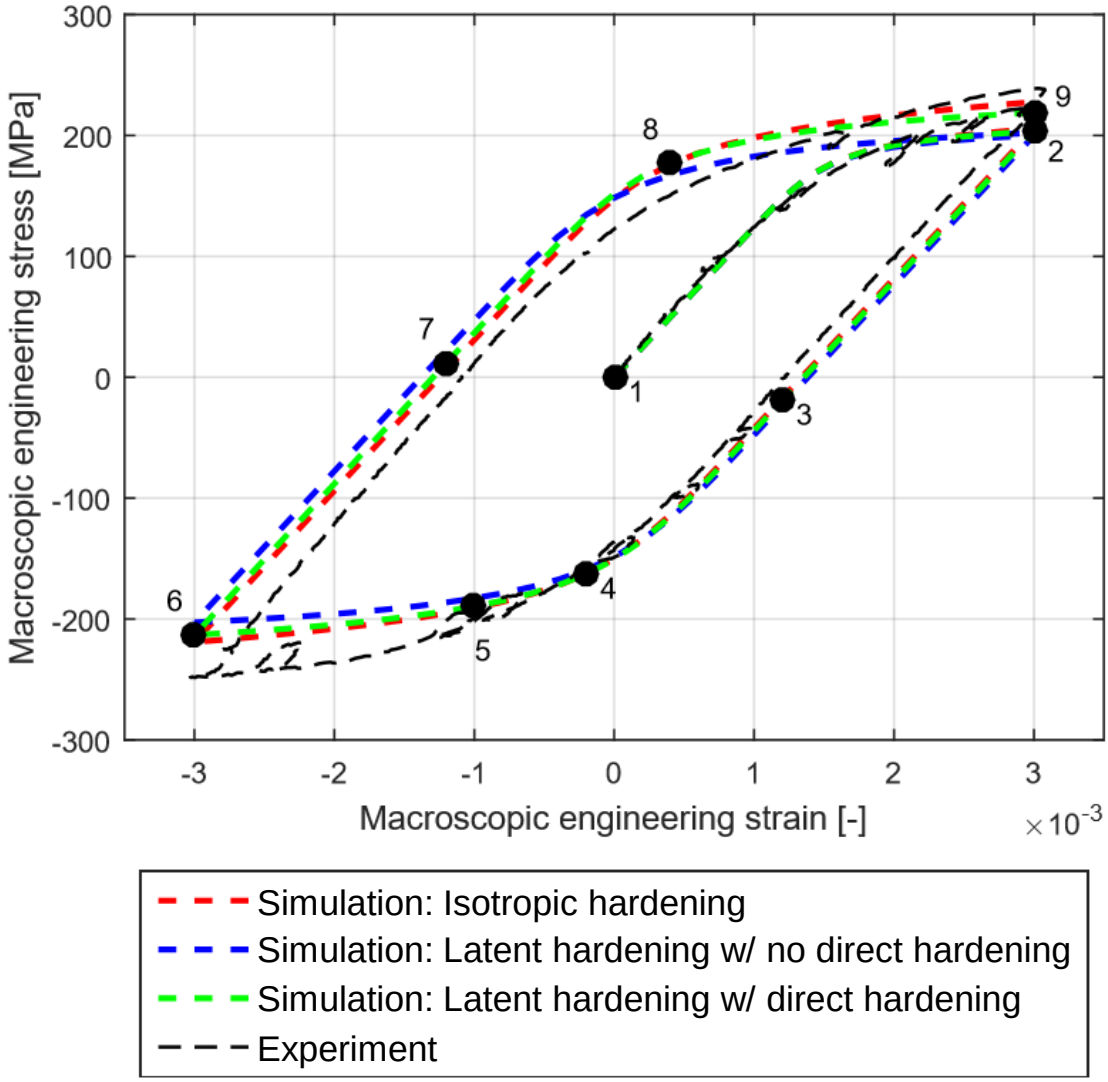

Figure 3.11: Macroscopic stress-strain response for the three simulations summarized in Table 3.2 along with the first cycle of the experimental stress-strain curve from the OMC incremental step test.

iality and coaxiality respectively. The stress coaxiality, β, is the angle between the macroscopic stress state and the crystal stress state: $\beta = \cos^{-1}(\boldsymbol{\sigma} \cdot \boldsymbol{S})/(||\boldsymbol{\sigma}||\,||\boldsymbol{S}||)$. Here $\boldsymbol{\sigma}$ is the measured crystal stress in the laboratory frame and $\boldsymbol{S}$ is the macroscopic stress. Triaxiality is defined as, $\chi = \frac{\sigma_{\mathrm{m}}}{\sigma_{\mathrm{eff}}}$, with mean stress, $\sigma_{\mathrm{m}} = \sigma_{ii}\backslash 3$, and

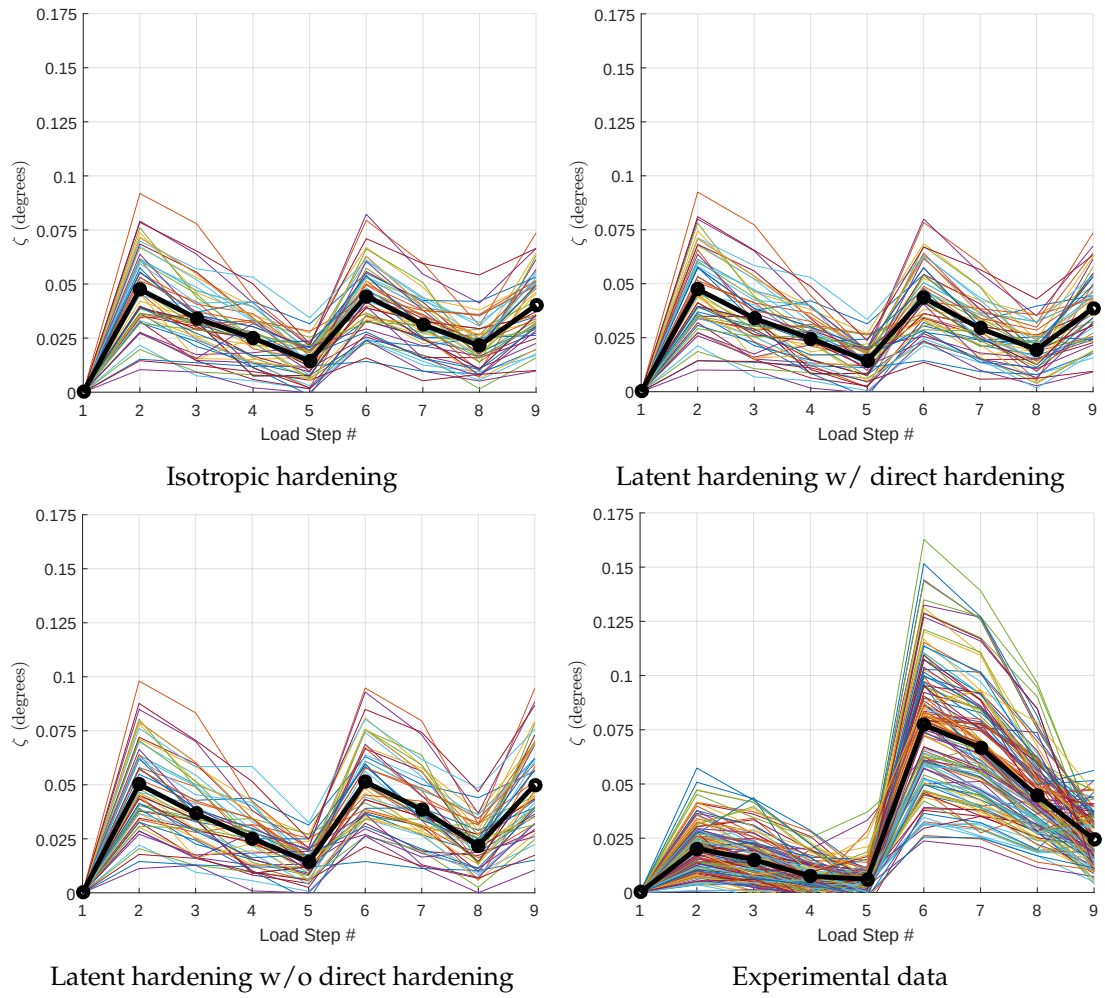

Figure 3.12: Misorientation metric, ζ, as the virtual sample is deformed for one cycle. Points correspond to locations labeled along the stress-strain responses in Figure 3.11.

effective stress, $\sigma_{\text{eff}} = \sqrt{\frac{3}{2}\boldsymbol{s} : \boldsymbol{s}}$ where $\mathbf{s} = \boldsymbol{\sigma} - \sigma_{\text{m}}\mathbf{I}$.

Figure 3.13 plots the stress coaxiality for OMC alloy and OFHC copper at the tension and compression loop tips as the materials are cycled. For purpose of visual aid, the grains for each material are sorted into two categories: larger average compression coaxiality and larger average tension coaxiality.

Regions of high stress triaxiality are linked with the propensity to accumu-

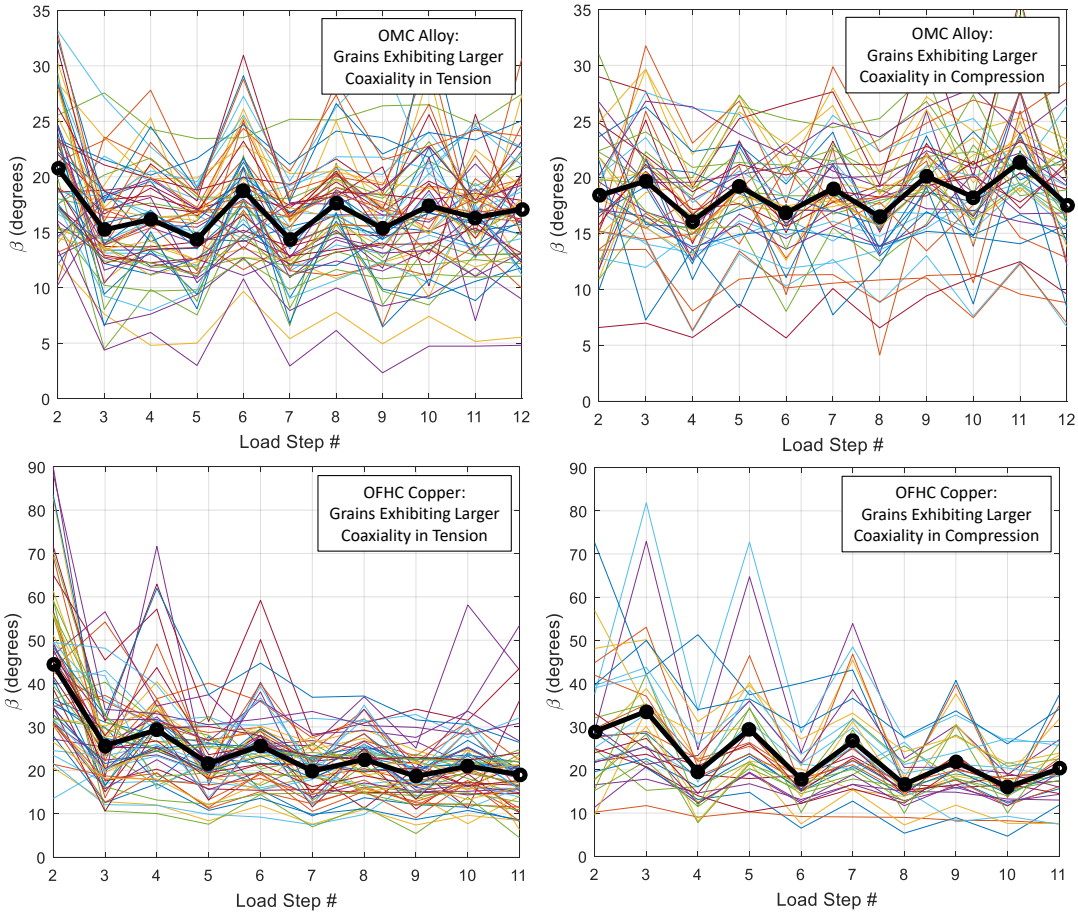

Figure 3.13: Stress coaxiality, β, plotted for the OMC alloy incremental step test and the OFHC copper at loop tips as the material was cycled between tension and compression. Grains were separated for each sample into tension biased and compression biased groups. The thicker line represents the grain-averaged value.

late damage in ductile metals [69, 15]. Figure 3.14 plots the triaxiality for the two materials. Little change is observed in the triaxiality within the OMC alloy during cycling. OFHC copper, on the other hand, shows a decreasing distribution of triaxiality among the grains between cycles 1 and 16.

The isotropic and latent hardening with no direct hardening simulations were each extended for an additional two cycles to compare the experimen-

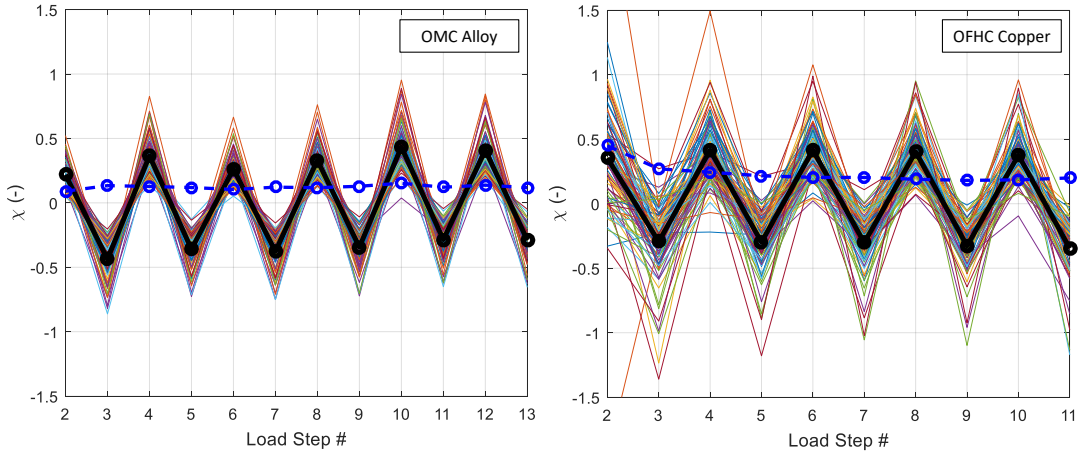

Figure 3.14: (Left) Stress triaxiality plotted for the OMC alloy incremental step test and (Right) the OFHC copper. The thicker line represents the average triaxiality. (remove blue line)

tally measured coaxiality during the first three cycles at 0.3% strain amplitude. Figure 3.15 plots the stress coaxiality, β, for the tension and compression loop tips for these two simulations.

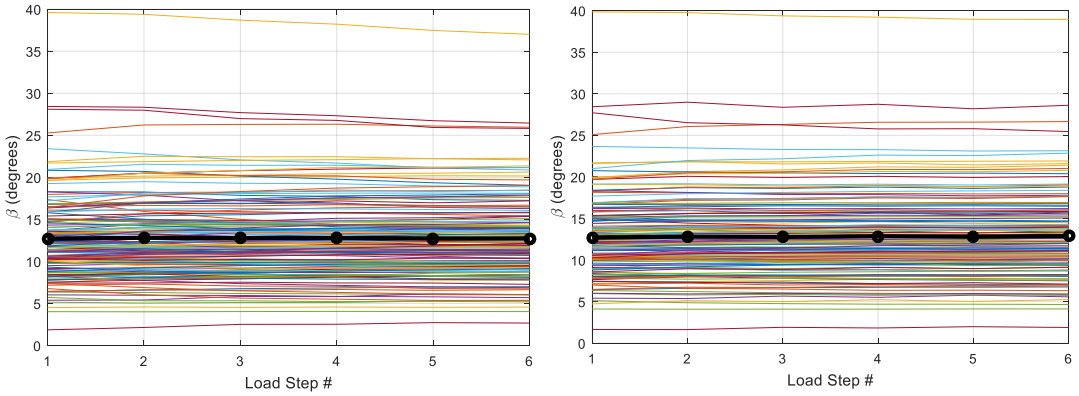

Figure 3.15: (Left) Stress coaxiality plotted for three tension-compression cycles of the isotropic simulation, (Right) the latent hardening simulation with no direct hardening

3.5 Discussion

The misorientation and strain distribution metrics, ζ and Θ, represent *in situ* mechanical testing data from individual grains within a deforming sample. Such data will aid mechanicians in understanding the development of deformation-induced heterogeneity at the grain scale, particularly for applications where capturing the appropriate heterogeneity within a model is vitally important. One such example motivating the present study is crack initiation within ductile metals, where past experiments have shown that plasticity tends to localize within grains and in some cases leads to cracks. The following discussion highlights the trends observed within the experimental data and discusses their significance with regards to the development of models capable of capturing the observed grain-scale heterogeneity within simulations.

3.5.1 Comparison of OMC alloy and OFHC copper

Experimental results displayed a drastic difference between the deformation induced misorientation and strain distributions within OFHC copper and OMC alloy under similar macroscopic loading conditions. Every grain interrogated within the OMC alloy exhibits a compression biased misorientation. On the other hand, the OFHC copper does not exhibit a bias during the first few cycles, but as cycling continues, the material develops a tension bias by cycle 16. The difference in the behavior of the two materials originates from the presence of precipitates within the OMC alloy. The finely dispersed precipitates impede dislocation motion, providing the OMC alloy with its high initial strength. Unlike the OMC alloy, the OFHC copper starts with a low strength and strain hardens

during cycling as defects accumulate within the crystals.

The coaxiality plots for OMC alloy and OFHC copper display a distinct asymmetry between tension and compression for each grain, meaning the crystal stress state is more closely alignment with the macroscopic stress state at one loop tip versus the other (tension vs. compression). The crystal stress states of the OFHC copper tend to become more aligned with the macroscopic stress state as the material is cycled - a trend not observed for the OMC. The stress states for OFHC copper also appear to become more homogeneous as the macroscopic stress approaches saturation. Decreasing coaxiality angles observed in the OFHC copper are consistent with the evolving single crystal yield surfaces of each grain. As the material strain hardens, the single crystal yield surface for each grain grows in stress space. Inherently this growth of the yield surface causes vertices to shift and crystal stress states to align more closely with the macroscopic stress state.

3.5.2 Reversing the cyclic loading direction

Two independent experiments were conducted using the OMC alloy, differing primarily by the direction of initial loading (tension vs. compression). Close inspection of Figures 3.5 and 3.7 reveals that tension-first loading produces larger misorientation in compression while compression-first loading generates larger misorientation in tension. The experimental data implies that the direction of initial loading defines the critical point during cycling where the misorientation is the largest. The strain distribution plots in Figure 3.5 and 3.7 reveal that, Θ, tends to oscillate from high to low in the same phase as the misorientation, ζ.

All the while the distribution of strain consistently increases in magnitude with each cycle, even though the macroscopic stress value remain largely unchanged.

Figure 3.7 shows that the average difference in ζ between tension and compression for cycles 1, 8, and 16 at 0.5% strain amplitude decreases in magnitude with added cycles, i.e., (ζ_{11} - ζ_{10}) < (ζ_9 - ζ_8) < (ζ_7 - ζ_6). This decreasing difference is graphically highlighted by the convergence of the two dotted lines superimposed onto Figure 3.7. We also note that (ζ_{11} - ζ_{10}) < (ζ_9 - ζ_8) in Figure 3.9. The difference in ζ for OFHC copper between tension and compression decreases between cycles 8 and 16 once the strength approaches saturation.

Traditional low-cycle fatigue models don't incorporate any information regarding initial direction of loading, yet the data show a distinct difference in the character of structural heterogeneity between samples loaded in tension first versus compression first. The decreasing bias in ζ between tension and compression observed in Figure 3.7 might imply that the magnitude of the bias becomes trivial after a significant number of cycles. Understanding the implications of these observations with regards to fatigue will require additional micromechanical measurements as a sample is cycled for a significant percentage of its life.

3.5.3 Structural heterogeneity during a cycle

The misorientation bias between the tension and compression loop tips presents an interesting cyclic plasticity phenomenon, which is further investigated by observing the evolution of ζ *during* a single cycle. For all of the simulations and the experiment in Figure 3.12, the value of ζ remains largely unchanged for

each grain from the beginning of one cycle (Point 2) to the end of the same cycle (Point 9). All of the simulation results in Figure 3.12 exhibit a minimum in misorientation near Points 5 and 8 of the macroscopic stress-strain curve. A similar minimum was observed within the experimental data in Figure 3.12 near Point 5. Unlike the simulation, Point 8 was not a local minimum of ζ in the experiment. Future experiments which acquire more measurement points along the elastic-plastic transition region to determine if a second minimum exist during the excursion from compression to tension. The observed minima of ζ in both the simulation and experiment highlights the ability of the crystallographic slip model to capture the reversible slip process during cycling.

Early SCSS experiments showed similar reversible plastic deformation, where a small volume within the crystal, the PSB, was accommodating all of the plasticity [73]. Visually the sample appeared unchanged between consecutive deformation cycles, but a large number of cycles lead to the formation of a crack and eventual failure. A similar analogy can be drawn for our polycrystalline samples when interrogated with high energy x-rays. Using ζ as our metric, it appears that the structure of each grain is largely unchanged from one cycle to the next, yet eventually a crack would form leading to sample failure if cycling continued. The nature of the reversible regions across the polycrystal have a completely different character than the PSBs observed in single crystals, since the plastic slip processes are no longer restricted to a single slip system.

3.5.4 Anisotropic Hardening Model

Interpreting the x-ray diffraction data from the perspective of a crystal plasticity model aids in understanding the connection between slip activity and structural heterogeneity. We specifically investigate the impact of the anisotropic slip system hardening assumption on the resulting orientation heterogeneity within each grain. Figure 3.12 plots the misorientation metric, ζ, for the three simulations and the experimental data during the first complete deformation cycle. The experimental data shows a much larger value of ζ in compression (Point 6) when compared to tension (Point 9). The isotropic hardening simulation shows values of ζ which are about equal between tension and compression, tension (Point 2) being slightly larger for a majority of the grains. Since slip system hardening is directly tied to reorientation within a grain, we might expect to see a large change once latent hardening is incorporated. Subfigures 3.12 (b) and (c) reveal that the latent hardening model does not drastically alter the resulting misorientation within each grain. The visible effects are a small overall increase in magnitude when direct hardening is turned off, along with a larger increase in ζ at the compression loop tip relative to the tensile loop tip. More grains show larger misorientation in compression instead of tension with direct hardening turned off. Regardless, incorporating the latent hardening model into the simulation did not generate the strong misorientation bias observed in the experimental data.

The simulation results in Figure 3.15 show very little difference in β between tension and compression. Most of the lines are nominally parallel across all three cycles. However, the experimental data shown in Figure 3.13 shows a distinct asymmetry in coaxiality for each grain between tension and compression.

The constant stress coaxiality angle implies that the tension and compression vertices of the single crystal yield surface evolve by the same amount during the simulations. The results identify a need to further study crystal plasticity framework that is based on the relatively simple kinematic decomposition shown in Figure 3.4.

3.5.5 Modeling Implications

Crystal plasticity models require mechanical testing data to fit coefficients associated with the internal state variables. Adding to the macroscopic stress-strain response, x-ray diffraction data provide a new level of detailed comparison between the experimental data and simulations. The observation of the tension-compression bias in experimental x-ray diffraction data guided the decision to explore the influence of hardening assumptions on the deformation induced heterogeneity within individual grains. Using such insight, modelers can make adjustments to crystal plasticity models to more closely match the experimental measurements.

The current modeling formulation does not explicitly model dislocation evolution nor incorporate their influence on deformation. Within the kinematic decomposition given by Equation 3.5, $\mathbf{F}^p$ assumes dislocations fully traverse the crystal lattice, i.e. the lattice remains unaltered after slip occurs. In reality, dislocations could produce both short-range and long-range interactions, and accounting for these interactions has been a topic of discussion in recent literature.

Acharya et. al. point out that lattice incompatibility is characterized by the skew-symmetric portion of the gradient of $\mathbf{F}^e$ and correlated this incompatibility

to Nye's dislocation tensor [1]. They then proposed an alteration to the slip system hardening rate (Equation 3.19) such that short-range interactions are incorporated, making the hardening rate a function of dislocation density in addition to the slip system shearing rates. In another approach, Gerkin et. al. incorporated the kinematics and stress effects of excess dislocations into the model by adding another term into the multiplicative decomposition of the deformation gradient [27]. The additional term accounted for long range strain due to the collective effects of excess dislocations. Another recent research direction includes higher-order strain gradient crystal plasticity models. Non-work conjugate formulations take into account a backstress resulting from the presence of geometrically necessary dislocations(GND) that are required to accommodate gradients of crystallographic slip [41, 12]. The approaches of Gerkin, Kuroda, and Bayley have the ability to address the Hall-Petch grain size dependence of flow stress, but require the introduction of a length scale which often lacks a physical basis. Regardless of the formulation, all of these approaches attempt to include the short or long range effects of dislocations into the crystal plasticity formulation. The x-ray diffraction data combined with the simulation results support the notion that alterations to the model beyond latent hardening are required to capture the behavior of the OMC alloy material system.

3.6 Summary and conclusions

A fatigue crack will form in a region which represents the weakest link within the material. The exact definition of this weakest link is still unknown, but is likely composed of a detrimental combination of stress and structural heterogeneity. Combining x-ray diffraction measurements and finite element simula-

tions serves as a novel approach to study problems where deformation heterogeneity plays a critical role such as fatigue crack initiation.

OMC alloy and OFHC copper were plastically cycled *in situ* at a synchrotron source using the high energy x-ray diffraction technique. The diffraction experiments provide a nondestructive means of probing the deforming aggregate and capturing the dynamic, heterogeneous nature of the crystal scale deformation. Crystal plasticity simulations were performed to provide insight into experimental observations of a bias in the magnitude of misorientation and strain heterogeneity between the tension and compression loop tips of the cyclic experiments. The traditional isotropic hardening assumption was extended to incorporate anisotropic slip system hardening. Below we summarize the conclusions drawn from this series of experiments and simulations.

- Unlike monotonic loading where plastically generated misorientation within individual grains of polycrystals continually increases with plastic straining, the misorientation during cyclic plasticity oscillates between two states (tension and compression) across multiple cycles, implying reversibility in the slip processes.
- Initial direction of loading determines whether larger misorientation and strain heterogeneity is observed within grains at the tensile or compressive loop tip during plastic cycling. The implications of this observation in terms of fatigue life requires further investigation and data suggests that the bias in misorientation between tension and compression may decrease with a large number of cycles.
- Drastic differences were observed in the bias of structural heterogeneity between tension and compression loop tips for OMC alloy and OFHC cop-

per. The presence of precipitates in the copper alloy provide OMC alloy with its strength and subsequently minimal changes in structural heterogeneity during cycling. OFHC copper strain hardens significantly during cycling resulting in significant changes in the structural heterogeneity between tension and compression.

- Simulations revealed that anisotropic slip system strengthening can both increase the overall level of structural heterogeneity across an aggregate and influence the misorientation bias. Introducing latent hardening into the crystal plasticity formulations did not produce the strong bias in misorientation observed experimentally. The crystal plasticity model based on a simplified kinematic decomposition may require further modification in conjunction with anisotropic slip system hardening to capture the grain-scale orientation heterogeneity if deemed critical for the problem under study. A few possible avenues to capture the tension-compression bias observed experimentally by capturing the effects of GNDs were discussed.

CHAPTER 4

CORRELATING THREE-DIMENSIONAL GRAIN MAPS AND STRUCTURAL HETEROGENEITY ACROSS HUNDREDS OF CYCLES

4.1 Introduction

Chapter 2 presented x-ray measurements using the first tension-compression capable load frame from the OMC alloy for a total of six cycles. Diffraction peak widths for all four grains interrogated during the experiment revealed a distinct compression bias of misorientation - misorientation was consistently larger at the compressive loop tips when compared to the tensile loop tips when the material was cycled under fixed strain amplitude. Prior to this observation monotonic loading experiments showed continually increasing misorientation within grains with the addition of inelastic strain. This first cyclic work revealed that inelastic strain can actually *reduce* the magnitude of misorientation within grains during fully-reversed cyclic loading.

Chapter 3 presents the first x-ray measurements conducted on commercially pure copper and presents additional results for the OMC alloy. Samples were cycled up to 16 cycles, and hundreds of grains from each sample were analyzed in contrast to the four grains presented in Chapter 2. Monitoring the diffraction peak widths for hundreds of grains presented a challenge, thus a metric to characterize the misorientation within each grain as a single scalar value was introduced. Comparing the changes in misorientation during cycling showed very different trends for the two materials. The misorientation bias observed in the OMC alloy appears at the very first cycle and persists for subsequent cycles. Unlike the OMC alloy, the pure copper does not show a sharp misorientation

bias for the first two cycles, but a strong bias develops after about four cycles.

Chapters 2 and 3 present advances in both experimental capabilities and methodology along with the development of data reduction tools, building towards the ability to track the mechanical response of every grain within a sample. This ability to monitor every grain is essential to advance our understanding of the microplasticity processes leading to the initiation of a crack. Using high-energy x-ray diffraction, we can now literally watch and structural heterogeneity evolve for every crystal while a sample is deformed.

This final chapter highlights a novel experimental technique to nondestructively measure three-dimensional orientation grain maps using high energy x-ray diffraction along with advanced data analysis methods to monitor the misorientation within each grain. Previous experiments only deformed the samples up to a total of 16 cycles. The micromechanical processes occurring at the subgrain scale which eventually lead to the initiation of a crack typically evolve over a much larger number of cycles. For this final experiment, loading of the sample is extended to a total of 256 tension-compression cycles. Since the spatial distribution of deformation proves important for a problem such as fatigue crack initiation, the misorientation measurements are combined with the spatial orientation map to gain understanding about the development of misorientation spatially across the aggregate.

4.2 Experimental methods

The experimental methods section describes the mechanical loading and x-ray measurements conducted on pure copper at the Cornell High Energy Syn-

chrotron Source. For this experiment, an orientation grain map was measured using the near-field x-ray diffraction technique prior to sample deformation. The data reduction procedure to convert near-field x-ray detector images to three-dimensional orientation maps of grains is summarized in Section 4.2.2. Section 4.2.4 outlines a novel data reduction process to measure the magnitude of misorientation within each grain from far-field data without the need to fit diffraction peaks.

4.2.1 Combined near-field, far-field experiment on pure copper

X-ray diffraction experiments were performed at the F-2 beamline at the Cornell High Energy Synchrotron Source (CHESS). The sample was electrical discharge machined from quarter inch diameter commercially pure copper rod. The samples gauge region had a cross-section measuring 1 mm by 1 mm. After manufacturing, the sample was heat treated in a nitrogen environment at 750 °C for two hours.

The experiment was conducted in two parts. During the first beamtime, x-ray diffraction images necessary to generate the orientation grain map using the near-field technique were collected. Whereas the far-field experimental geometry enables sensitivity to measure orientation distributions and lattice strains for individual grains, the near-field is highly sensitive to grain positions. This sensitivity to position is what enables the generation of the 3-D grain maps. Near-field data at CHESS is acquired using a Retiga 4000DC detector with a sensor containing 2048 x 2048 pixels. Each pixel has a 7.4 x 7.4 micron physical size. The typical setup utilizes a 5x Mitutoyo infinity objective optic which

creates an effective pixel size of 1.48 microns. A 100 micron thickness LuAG:Ce scintillator converts the x-rays to the visible light measured by the detector. The detector for this experiment was placed at a distance of about 8 mm from the rotation axis at an x-ray energy of 61.332 keV. A total of four, 125 micron tall layers were measured, effectively enabling the creation of a 1 mm x 1 mm x 0.5 mm reconstruction of the spatial grain orientation map. The beam width is wider than the sample during the x-ray measurements. The sample was marked with a platinum wire so that the mapped volume could be subsequently scanned in the far-field experimental geometry.

During a subsequent beamtime, the sample was mechanically deformed in combination with far-field x-ray measurements The GE area detector was utilized with an x-ray energy of 61.332 keV and a sample to detector distance of about 850 mm. During this experiment, a total of five, 125 micron tall layers were scanned at each load step, such that the previously mapped volume was contained within the far-field data. The sample was deformed for a total of 256 tension-compression cycles at a fixed strain amplitude of 0.3%. Detailed scans around the stress-strain hysteresis loops were measured for cycle numbers 2 and 256 as shown in Figure 4.1. The macroscopic strain was monitored using digital image correlation (DIC). Cycling of the sample was performed under displacement control. The displacement endpoints at the hysteresis loop tips were periodically, manually adjusted to maintain a consistent strain amplitude based on the DIC data.

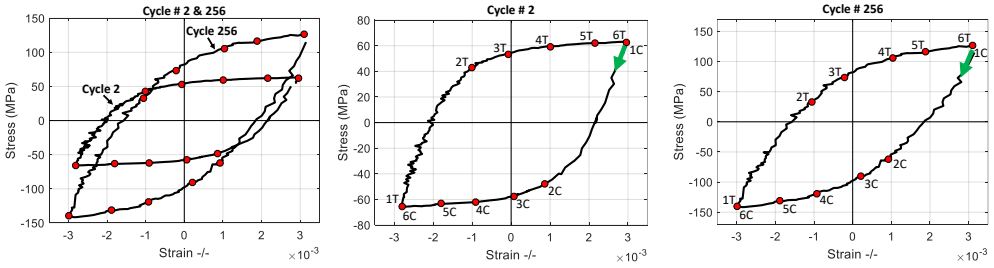

Figure 4.1: Stress-strain history of a cyclic experiment performed on commercially pure copper. The hysteresis loops are plotted for cycle numbers 2 and 256 of the experiment. Corresponding x-ray diffraction measurement points are labeled as numbers 1 through 6. The accompanying letters ″C″ and ″T″ denote excursions from maximum tension to compression and maximum compression to tension respectively. The green arrow identifies the starting point for each hysteresis loop.

4.2.2 3-D grain map data reduction

Generating three-dimensional orientation maps is not a new technique. Electron backscatter diffraction (EBSD) is a commercially available technique utilized to measure two-dimensional orientation grain maps of the surface of a sample. EBSD combined with serial sectioning is one method to obtain a 3-D orientation map of a polycrystal. The major disadvantage of such a system is that the sample is destroyed during the measurement process. Nondestructive X-ray measurement techniques have also been utilized to obtain three-dimensional orientation maps of polycrystals. One example is a line beam technique implemented at the Advanced Photon Source. The x-ray beam is focused such that the beam height is 1 micron with a width larger than the sample [72]. Such a technique provides good spatial resolution ($\sim 1\ \mu^3$), however, consumes a large amount of experimental time since each layer only measures 1 micron of material thickness.

Data contained in this work was reduced using original Matlab-based data reduction code. The current data reduction technique requires a combined far-field and near-field data set to generate the three-dimensional orientation grain maps. Data reduction begins by indexing the far-field data to identify all of the grain orientations contained within the diffraction volume. These grain orientations become the seed orientations for the near-field data reduction algorithm.

Similar to the far-field experiments, the sample rotates continuously as diffraction images are collected. The rotation is synchronized to the detector triggering such that each detector image corresponds to a 0.25 degrees of rotation. Thus across a full 360 degrees of rotation a total of 1440 images are acquired. A median dark image is first created from the image stack by calculating the median pixel intensity for each pixel across all 1440 images. The median dark is then subtracted from each image in the image stack to remove the background. The next step requires that each image is thresholded and converted to a binary image. Pixels below the threshold are set to zero in the new binary image stack while pixels with intensity values above the threshold are set to unity. The binary image stack is utilized in subsequent analysis.

A virtual 3-D voxelated volume is instantiated in Matlab. The size of this volume is chosen to have a height equal to the beam height (125 microns in this case) and a cross-section which is about 10% larger than the sample cross section. For this experiment, the sample's cross-section measured 1 x 1 mm, thus a virtual volume with cross-sectional size of 1.1 x 1.1 mm was instantiated. Each voxel is assigned a centroid position consisting of an X, Y, and Z coordinate. Each of these points acts as a diffraction center in subsequent data reduction steps.

Approaching the reconstruction, we do not know the position of each grain, however, we do know the possible grain orientations within the volume. Seeding the reconstruction algorithm with a small subset of orientations from the far-field data eliminates the need to search all of orientation space for possible grain orientations. The algorithm begins by choosing one grain orientation and assigning it to all the centroid positions within the virtual volume. The position combined with this orientation is input into the virtual diffractometer. The virtual diffractometer predicts the pixel position and image number within the image stack of 1440 images for each diffraction peak. The process is repeated for each grain orientation on the search list provided by the far-field data. Essentially each voxel within the volume under reconstruction is systematically assigned every orientation measured in the far-field experiment. Each voxel and orientation combination generates a series of predicted diffraction events which are recorded in a database.

The list of pixel positions and image numbers is then compared to the binary image stack. A completeness parameter is defined as the ratio of the number of experimentally observed diffraction events to the number of predicted diffraction events. This completeness is defined for each voxel for every possible grain orientation. The final grain map assigns the grain orientation with the highest completeness to every voxel. Figure 4.2 provides a reconstructed layer of a copper sample containing about 1200 unique grain orientations.

The current implementation of the near-field data reconstruction ignores any intensity information since the image stack is converted to binary data prior to reconstruction. Additionally, each grain is assumed to contain only a single orientation, meaning gradients of orientation across a grain are not extracted

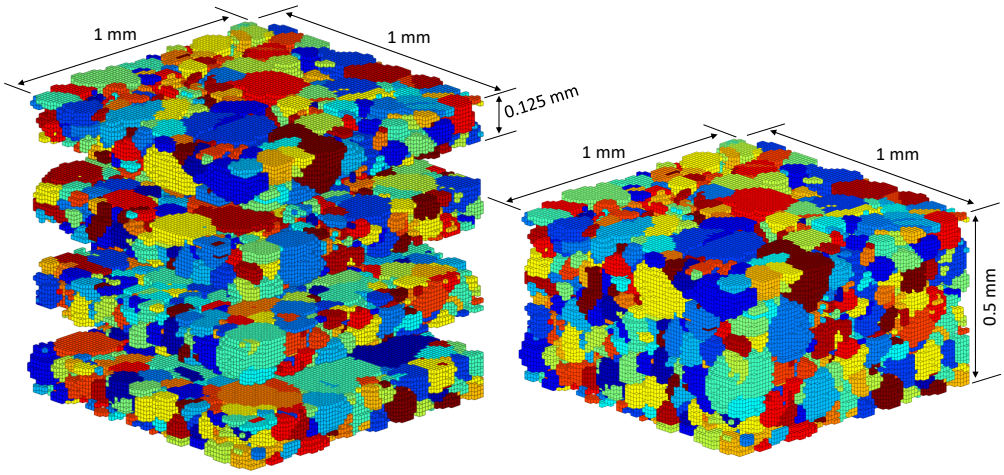

Figure 4.2: Orientation grain map measured nondestructively using high energy x-rays and a near-field detector placed about 8 mm from the sample. (Left) Each individual layer measured using x-ray diffraction and (Right) the layers stitched together. Each color represents a different grain; grains can span multiple layers. Colors are reused for different orientations.

from the x-ray measurements.

4.2.3 X-ray diffraction far-field data analysis

Each x-ray diffraction peak contains a multitude of information. The positions of every peak collectively from one grain is used to calculate a grain's orientation and lattice strain. The profile of each diffraction peak additionally contains insight into the heterogeneity of lattice orientation along with the heterogeneity of lattice plane spacing. The data reduction process highlighted here focuses on extracting the heterogeneity of orientation within each grain. Monitoring the radial peak widths during deformation provides a means of tracking strain heterogeneity, while the azimuthal peak widths provide a measure of orientation heterogeneity. Chapter 2 of this dissertation focused on only four grains within

a polycrystal. The diffraction peak widths for the four grains were visualized as ”quilt” plots - graphically representing the magnitude of each peak width for every diffraction peak at every load step. Examples of these data were shown in Figures 2.7 and 2.8.

Plotting and visually interpreting the quilt style plots for a large number of grains was not feasible, thus heterogeneity metrics were developed to condense the quilt plots into scalar metrics. These metrics, described in Chapter 3 effectively averaged the changes in diffraction peak widths across all diffraction peaks for a single grain. The values of Θ and ζ could then be plotted for each grain within the diffraction volume as the sample underwent deformation.

Both of these approaches to monitor the grain-scale lattice heterogeneity require fitting of the diffraction peaks. Typically peak shape functions such as the Gaussian, Voigt, or Split Pseudo-Voigt profiles are used to approximate the peak shape. These functions fit the peak profiles relatively well when plastic strain remains small. Increasing plastic strain causes peaks to broaden and often become asymmetric, increasing the difference between the measured diffraction peak and the fit profile. Large plastic strains can also result in peak overlap, once again limiting the ability to fit diffraction peaks with predefined functions. Section 4.2 describes a novel methodology to monitor the orientation heterogeneity within each grain through a method utilizing forward projection. This new method which produces three-dimensional orientation ”clouds” eliminates the need to fit peaks and can be used on data sets measured at large plastic strains.

4.2.4 Generating single crystal orientation "clouds"

Orientation space indexer

This work has focused on monitoring orientation and strain heterogeneity within grains as a polycrystal is deformed. This section provides a new means of quantitatively measuring the misorientation within each grain. The approach produces single crystal orientation "clouds", which represent the distribution of orientation within each grain. Tracking the changes of the size of these clouds in orientation space provides a new metric which is analogous to ζ defined in Chapter 3. The following outline starts by describing a newly implemented grain indexing algorithm which is adapted to generate the single crystal orientation clouds.

The subsequent indexing algorithm is specifically described for the FCC crystal structure since this project has focused on copper. The algorithm has been successfully implemented for the hexagonal crystals as well.

Indexing begins by preparing the far-field x-ray diffraction images. The procedure largely mirrors the image preparation outline provided in Section 4.2.2. A median dark image is generated from the image stack and subtracted from each image. The images are then thresholded and finally converted to a binary image stack. The threshold can be quite low for this process, producing successful results for thresholds ranging from 7-15 counts after median dark subtraction for the GE area detector.

The next step in the data reduction process involves populating the FCC fundamental region with a grid of points - each point representing a unique crystal

orientation. At the moment, a uniformly spaced grid of points is implemented, but there is no restriction on the pattern of points implemented in this algorithm. An example of a coarsely populated fundamental region is provided in Figure 4.3. The fundamental region is subdivided into octants to minimize the required computational resources. The density of points within each octant determines the thoroughness of the orientation search and also the amount of time required to index a set of x-ray diffraction images. Grains will be missed if the grid is too course, however, indexing will take a very long time if the grid is too fine. Experience has shown that a grid of 180x180x180 points across one each octant will identify approximately 70-90% of the grains in the data set A grid of 360x360x360 points across each octant typically results in a comprehensive search of the orientation space.

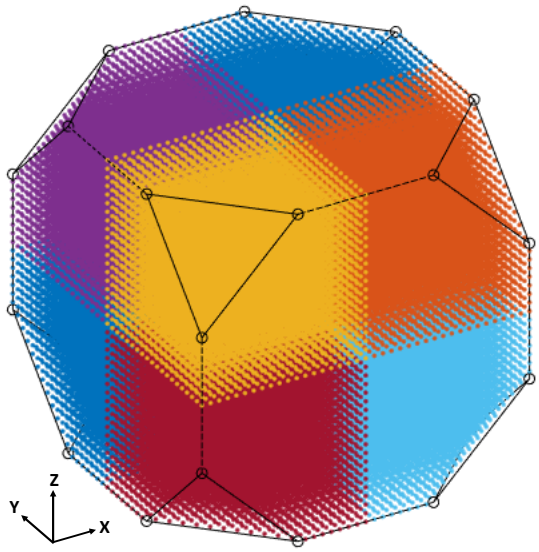

Figure 4.3: The cubic fundamental region populated with a grid of points representing unique crystal orientations. The current grid is relatively coarse - 20 points in each direction across each octant of the fundamental region. Each octant is colored differently for visual purposes. Each of these points represents a trial orientation during grain indexing.

Each grid point (orientation) is then input into the virtual diffractometer. Scattering is assumed to originate at the sample origin, however, this is not a restriction. The virtual diffractometer produces a list of pixel positions and image numbers for each grid point corresponding to locations where diffracted intensity is anticipated. A completeness threshold is defined, typically over 80%, which defines a successful observation of an orientation in the data. This completeness threshold is expressed as the ratio of number of observed diffraction peaks versus predicted diffraction peaks.

The results of indexing a commercially pure copper diffraction volume is shown in Figure 4.4. The next step is to cluster observed orientations since each grain can be potentially observed multiple times, especially when a fine grid spacing is utilized. The clustered orientations correspond to unique grains within the diffraction volume. Clustered orientations for the pure copper are shown in Figure 4.5.

One of the primary advantages of this methodology is that it does not rely upon peak fitting. Peak overlap due to large deformation or texture can make indexing difficult with approaches such as fiber indexing. The virtual diffraction experiment for each trial orientation produces anywhere from about 50 to 100 diffraction events depending on the number of rings on the detector and the sample rotation angles during the experiment. The completeness threshold defines whether or not a trial orientation is observed within the sample. Due to this redundancy of needing to observe many diffraction events for each trial orientation, even a few overlapped peaks for a grain will not adversely effect the ability to identify a grain. In fact, this indexing methodology can be used to process data sets which exhibit powder type patterns due to large plastic strains

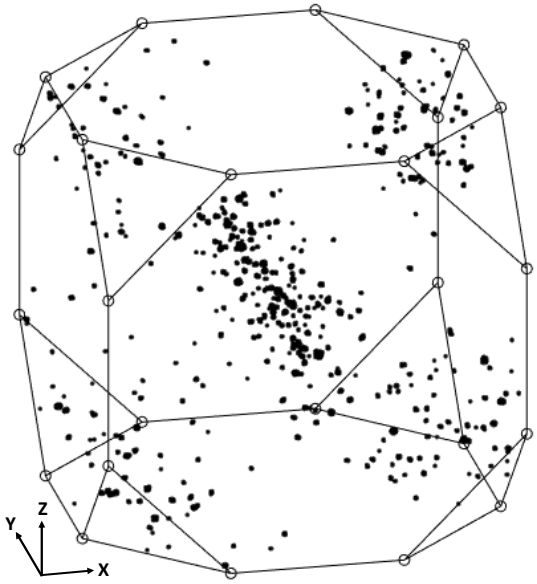

Figure 4.4: Indexed orientations within a volume of commercially pure copper. Each point represents an observed trial orientation in the experimental data using a grid of 220 x 220 x 220 trial orientations across each octant. Groups of clustered trial orientations represent a grain in the sample.

by increasing the intensity threshold when converting the raw detector images to a binary data stack. Such an approach can help identify whether the diffraction volume contains very small grains with sharp texture versus few grains with large amounts of plastic deformation.

As a side note, indexing a polycrystal which has undergone a small amount of plastic deformation (less than 1% plastic strain) can provide a more comprehensive indexing results with a coarser grid. This is due to the fact that diffraction peaks will spread on the detector with plastic deformation, increasing their volume in orientation space. The procedure above assumes that the position of each crystal is at the center of the diffraction volume. If a sample's cross sectional dimension are large relative to the size of each detector pixel, predicted locations of diffracted intensity versus observed locations on the detector could

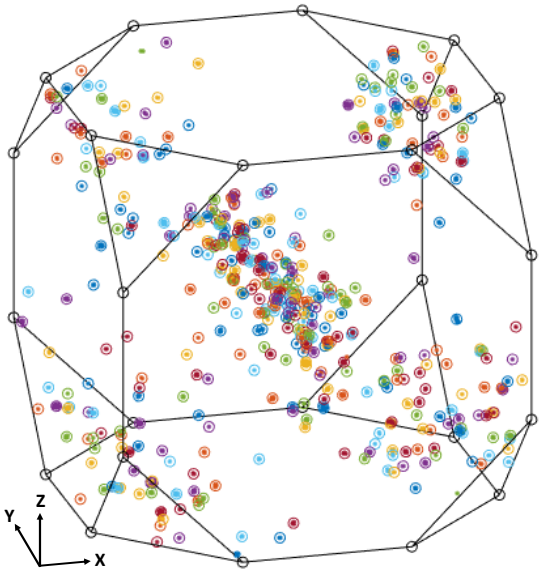

Figure 4.5: Groups of observed trial orientations are clustered to identify grains within the diffraction volume. The observed trial orientations within each cluster are averaged to determine the average orientation of each grain.

differ significantly for grains near the edges of the sample. In this scenario, the orientation space indexer can be modified such that the position of each grain is no longer the centered at the origin, but rather, closer to the edges of the sample. Intensity on currently used x-ray detectors such as the GE detector generally bleeds to adjacent pixels at reduced intensity. A point spread function is implemented in the virtual diffractometer to capture this spreading of intensity. This tendency for intensity to spill over to adjacent pixels is advantageous when it comes to indexing grains using the algorithm described above.

Modification to generate single crystal orientation "clouds"

The orientation space indexing algorithm is modified to index local regions of orientation space to build the single crystal orientation "clouds." An observed

grain orientation originating from the indexer is used to seed a sub-volume of orientation space surrounding the average grain orientation. In the current implementation, a cube is drawn with this seed orientation at the center of the cube. This cube is then populated with a grid of points. This grid is a local region of orientation space surrounding a known grain orientation. Once again, each of the orientations within this cube are input into the virtual diffractometer and predicted intensity is compared to observed intensity. After thresholding a cloud emerges which, represents the distribution of orientations observed within the particular grain of interest. Figure 4.6 provides an example of a cloud prior to deformation. The average position of the cloud represents the average orientation while the size represents the distribution of orientation within a grain. Both these quantities can evolve with deformation. Figure 4.7 plots the change in the orientation cloud for one grain as the sample is deformed. The cloud's position, size, and shape changes with plastic deformation, signifying changes in the distribution of orientation within the grain.

The distribution of orientation within each cloud is convoluted with characteristics of the x-ray beam and detector such as divergence and the point spread function, thus we look at the changes in the cloud shape as a function of deformation. The angular extent of misorientation within each grain is quantified following the approach in [68]. The average orientation is calculated as the center of mass position of the cloud as a Rodrigues vector and designated as $\bar{\mathbf{r}}$. The difference between the Rodrigues vector for each point in the cloud, $\mathbf{r}^{\alpha}$, and the average orientation, $\bar{\mathbf{r}}$, is designated as $\mathbf{w}^{\alpha}$.

$$\mathbf{w}^{\alpha} = \mathbf{r}^{\alpha} - \bar{\mathbf{r}} \tag{4.1}$$

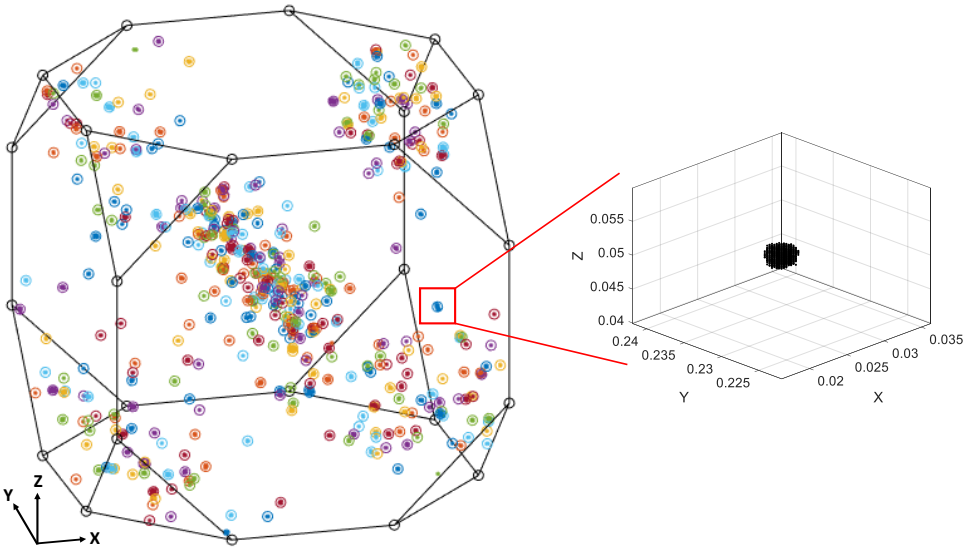

Figure 4.6: (Right) Enlarged view of a single crystal orientation cloud generated after grain indexing. The average position of the cloud represents the average orientation of the grain while the size of the cloud is linked to the distribution of orientations within the grain.

The average misorientation angle, $\bar{\zeta}$, is given by,

$$\bar{\zeta} = 2 \sum_{i=1}^{N} \phi^{\alpha} \arctan|\mathbf{w}^{\alpha}| \tag{4.2}$$

The weighting value, ϕ^{α}, used here is one over the total number of points in the cloud. The average misorientation is computed for each grain within the aggregate as it deforms. The final step is to quantify the change in average misorientation from the initial state is to remove the effects of beam divergence and the point spread function. This is accomplished by subtracting the initial value of, ϕ^{α}, for the undeformed material from all subsequent measurements. This final value defines the change in misorientation from the original state for every grain and will be labeled as ”misorientation” within subsequent figures.

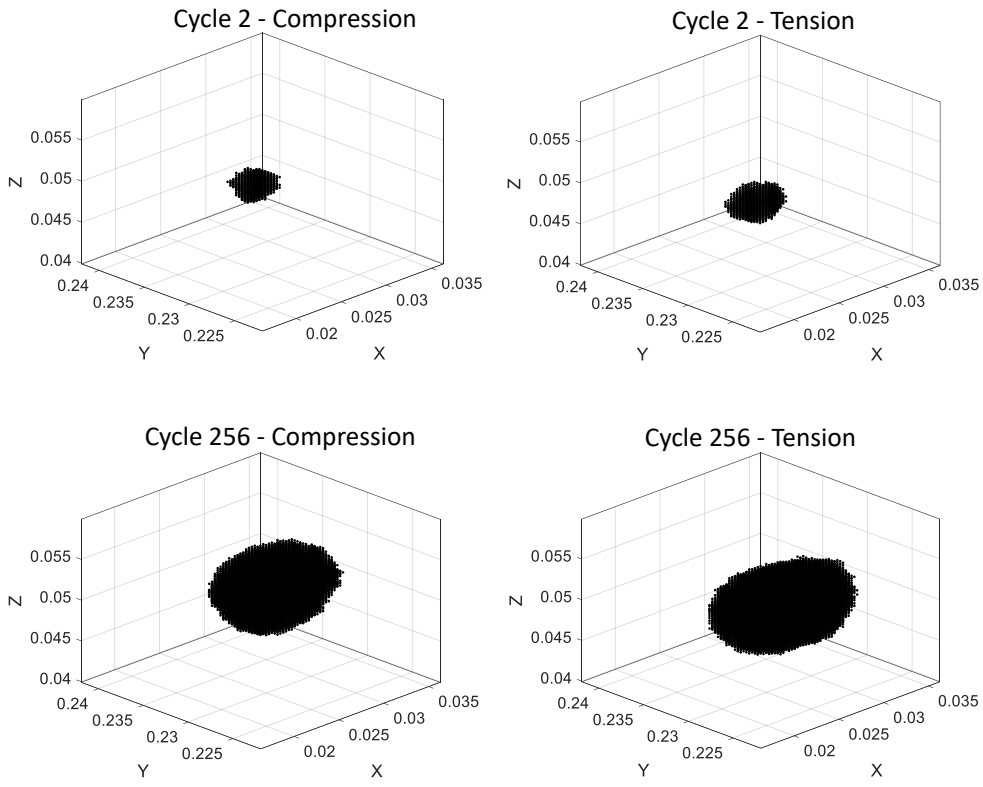

Figure 4.7: Orientation clouds for one grain at the compression and tension loop tips of the experiment for cycle numbers 2 and 256. Note the change in position, size, and shape of the cloud with deformation.

4.3 Results

4.3.1 Utility of the orientation grain map

Figure 4.8 shows the orientation grain map for the OFHC copper sample. The individual layers remain separated to highlight the three-dimensional character of the data. A total of about 1200 grain orientations were utilized to construct the grain map. A voxel size of 12.5 microns cubed was chosen for this reconstruction. Quantities can be superimposed over this grain map to reveal spatial

trends. As an example, the colors shown in Figure 4.8 correspond to the volume of each grain within the reconstructed aggregate. Previously, the grain volume could not be extracted from the far-field data alone. The average grain position and information regarding neighboring grains is available within the data as well.

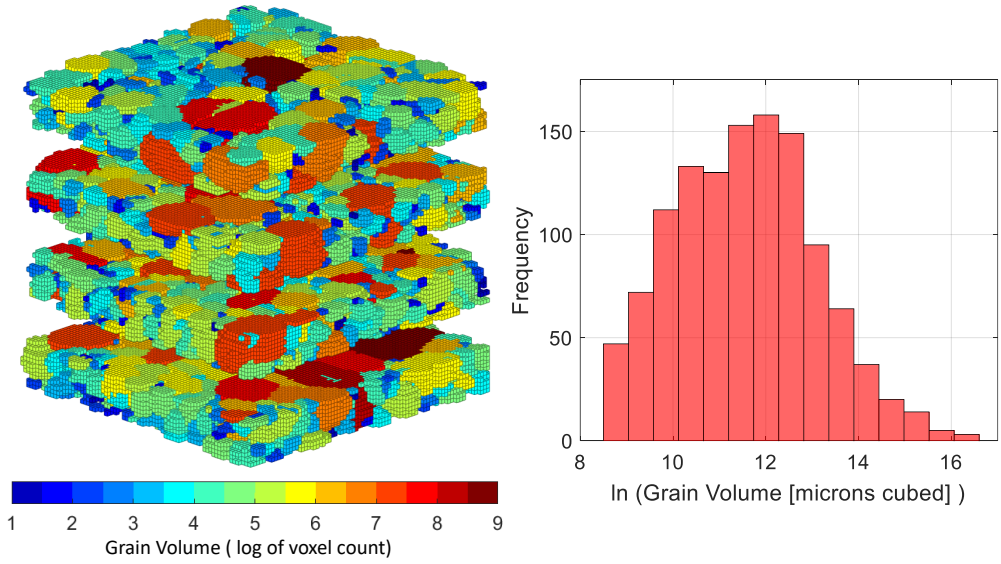

Figure 4.8: (Left) Each grain's volume is plotted over the spatial grain map. Color corresponds to the natural log of each grain's volume in voxels. Each voxel's physical size within the sample is 12.5 microns cubed. (Right) Histogram plotting the natural log of grain volumes calculated in microns cubed. Grains under three voxels are omitted in both plots

4.3.2 Intra-cycle misorientation evolution for 2 and 256 cycles

X-ray measurements were performed at specified macroscopic strain values at cycle numbers 2 and 256 as shown in Figure 4.1 The evolution of misorientation is track using the methodology described in Section 4.2.4. The distribution of intensity for each of the measurement points is plotted in Figures 4.9 and 4.10.

Figures 4.9 plots the the misorientation evolution for cycle number 2 in two parts. First the excursion from the tension loop tip along the elastic-plastic transition down to the compression loop tip is plotted. Next the excursion from the compression loop tip up to tension loop tip is plotted in the same figure. Figure 4.10 repeats these plots for cycle number 256. Note the differences in scales for Figures 4.9 and 4.10.

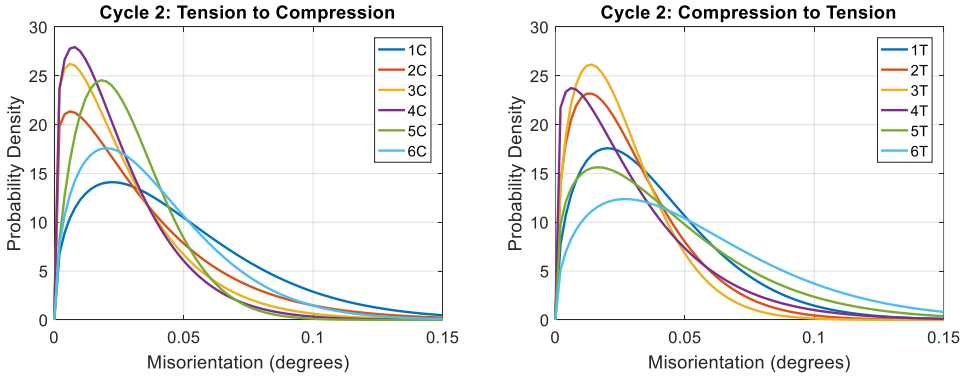

Measurement Point	Mean (degrees)	STD (degrees)
1C	0.047	0.034
2C	0.034	0.030
3C	0.027	0.023
4C	0.025	0.020
5C	0.028	0.017
6C	0.038	0.026

Measurement Point	Mean (degrees)	STD (degrees)
1T	0.038	0.026
2T	0.029	0.021
3T	0.026	0.017
4T	0.030	0.026
5T	0.043	0.033
6T	0.054	0.038

Figure 4.9: Misorientation evolution plotted as a Weibull distributions during excursions from (Left) tension to compression and (Right) compression to tension for cycle 2 on pure copper. The accompanying mean and standard deviation of each distribution are provided. Data was measured at points labeled along the stress-strain history in Figure 4.1.

The spatial distribution of misorientation at the compression and tension loop tips for cycles 2 and 256 is plotted in Figures 4.11 and 4.12 overlayed on top of the grain map.

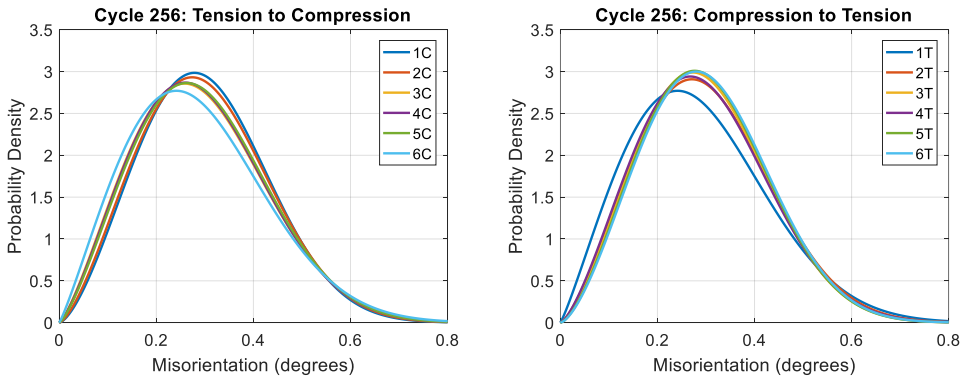

Measurement Point	Mean (degrees)	STD (degrees)
1C	0.302	0.128
2C	0.301	0.131
3C	0.293	0.135
4C	0.294	0.135
5C	0.296	0.135
6C	0.287	0.141

Measurement Point	Mean (degrees)	STD (degrees)
1T	0.287	0.141
2T	0.300	0.132
3T	0.298	0.128
4T	0.296	0.131
5T	0.300	0.127
6T	0.303	0.128

Figure 4.10: Misorientation evolution plotted as a Weibull distributions during excursions from (Left) tension to compression and (Right) compression to tension for cycle 256 on pure copper. The accompanying mean and standard deviation of each distribution are provided. Data was measured at points labeled along the stress-strain history in Figure 4.1.

4.4 Discussion

4.4.1 Misorientation evolution at low vs high cycle counts

The evolution of misorientation for both cycle numbers 2 and 256 was monitored through high energy x-ray diffraction measurements on a pure copper sample subjected to cyclic deformation at a fixed macroscopic strain amplitude of 0.3%. Figures 4.9 and 4.10 plot the distribution of misorientation across all of the 1200 grains during these two cycles. Figure 4.9 reveals the dynamic evolution of misorientation evolution for all the grains during cycle 2. First off, comparison of the tension loop tip (1C) versus the compression loop tip (6C) reveals a larger distribution of misorientation across the aggregate in tension

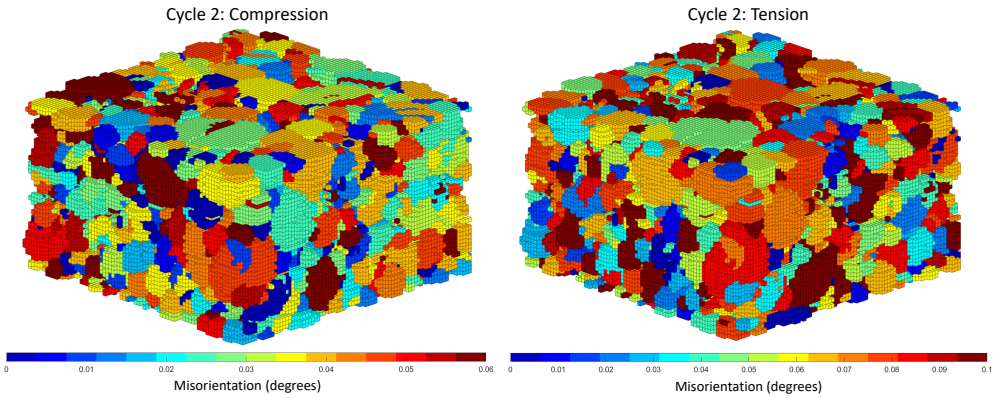

Figure 4.11: Misorientation plotted across the spatial grain map at the loop tips of cycle number 2. A single color, representing the magnitude of misorientation, is plotted across each grain.

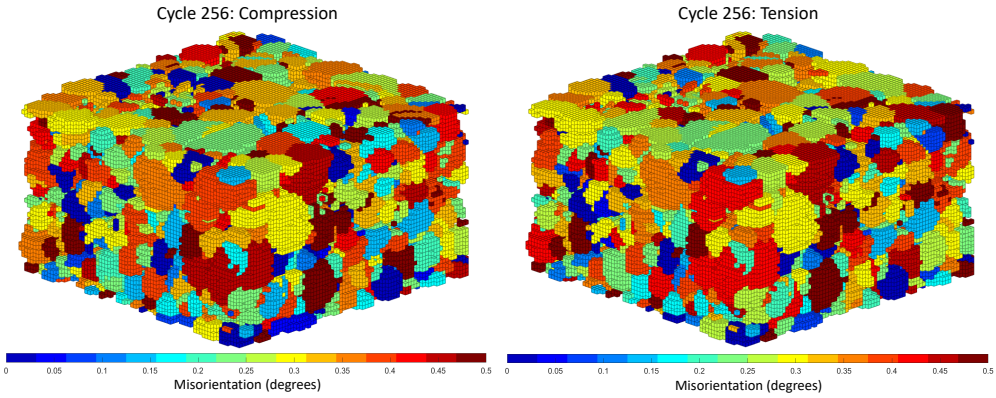

Figure 4.12: Misorientation plotted across the spatial grain map at the loop tips of cycle number 256. A single color, representing the magnitude of misorientation, is plotted across each grain.

when compared to compression. Between these two points, we observe a drastic evolution in the distribution of misorientation during the transition from tension to compression. The average misorientation initially decreases and the distribution of misorientation across the aggregate decreases as well. Continued inelastic deformation eventually increases the average value and breadth of the distribution. A similar trend is observed in the excursion from compression to tension in Figure 4.9 for cycle 2. Figure 4.10 plots the misorientation evo-

lution for cycle number 256. This figure reveals that the misorientation within the grains has increased significantly in magnitude and much less evolution is observed during a cycle. A misorientation bias in compression is still observed after 256 cycles by comparing the locations of the profile peaks between tension and compression.

Figures 4.11 and 4.12 plot the spatial distribution of misorientation across the grain map at the tension and compression loop tips of cycles 2 and 256. Comparing the compression and tension loop tips at cycle 2 in Figure 4.11 shows that individual grains which exhibit a large amount of misorientation in compression, do not always show a large amount of misorientation in tension as well. Conversely, Figure 4.12 reveals that generally a grain exhibiting a large misorientation in compression also exhibits a large misorientation in tension. Comparing grains across cycles 2 and 256 shows that a large misorientation value at a low cycle number does not necessarily imply a large misorientation at a higher number of cycles.

Analysis of the misorientation distribution did not reveal any correlation between misorientation and grain orientation. Additionally, grains near the surface were not statistically more likely to exhibit higher misorientation. A lack of obvious trends in the misorientation data points toward the importance of grain to grain interactions. The experimental data implies that the character of a grains neighborhood plays a much more significant role in the development of grain-scale orientation heterogeneity than factors such as its orientation or spatial position.

4.4.2 Interpretation of orientation clouds

The single crystal orientation clouds represent the distribution of orientation within each grain. During the data reduction process the intensity information from the detector is discarded, so there is no intensity data connected to each point within the orientation clouds. In reality observing certain orientations within these clouds would be statistically more probable. One way to take the intensity into account would be to calculate the single crystal orientation distribution function (SCODF) for each grain. Calculation of the SCODFs would take into account the intensity of each diffraction peak. The intensity observed on the detector is actually the integrated intensity of a fiber through the SCODF. The orientation clouds provide a simplified metric which does not require inversion of the data.

Another important comment to make is that the misorientation calculated for each grain is a single, average value for the grain. In reality, there is a spatial gradient of orientation across every grain within the aggregate. Currently we are unable to calculate this spatial distribution experimentally. Ideally the misorientation distributions plotted in Figures 4.11 and 4.12 would contain spatial misorientation information across each grain. Often times, larger lattice rotations are observed near grain boundaries. Knowing the exact location within grain where misorientation is largest could help in identifying regions where heterogeneous deformation leads to crack initiation.

4.4.3 Challenges measuring crystal stresses

Using the far-field high-energy x-ray diffraction methodology, typically the average lattice strain tensor can be calculated by monitoring the radial shift of diffraction peaks upon loading. These strain tensors are readily converted to stresses through Hooke's Law. The magnitude of the radial shift for each diffraction peak with the current experimental equipment is only a fraction of a pixel size. Thus we are required to fit the diffraction peaks profile to accurately measure the peak's shift in radial direction. Unfortunately for the pure copper, lattice strains have a very small magnitude. Because of this reason, the signal to noise ratio is relatively low, producing large errors in the lattice strain measurements. Additionally, the relatively large value of misorientation within each grain once the sample is deformed for 256 cycles provides relatively poor results during diffraction peak fitting. For these reasons, average crystal stresses are not presented for this data set.

4.5 Summary

This final experiment promoted the development of advanced data reduction tools and provided new insights into the cyclic deformation of ductile metals using the high energy x-ray diffraction methodology. Data reduction capabilities have advanced to a point where literally every crystal within an aggregate can be monitored as a sample deforms. The misorientation was measured by introducing a novel technique to generate single crystal orientation "clouds," which do not require diffraction peak fitting. The x-ray diffraction data in this final chapter represents the first successful attempt to correlate the distribution

of misorientation within each grain to a three dimensional grain map of an aggregate.

During this experiment a copper sample was deformed for a total of 256 cycles in conjunction with x-ray diffraction measurements. The experimental results did not reveal any strong correlations between the misorientation within grains and their average orientation or spatial position in the aggregate, pointing to the importance of grain to grain interactions. The results did however reveal the dynamic evolution of misorientation across the aggregate as the material was cycled. The character of this intra-cycle misorientation distribution was significantly different when comparing cycles 2 and 256. Correlating the misorientation measures with the three dimensional grain maps revealed that the distribution of misorientation across the aggregate is much more similar between compression and tension at cycle number 256 versus cycle number 2. Stated another way, grains exhibiting large misorientation in tension at cycle 256 typically also exhibit a large misorientation in compression as well. This trend was not observed for cycle number 2. Additionally, large misorientation within a grain at an early cycle does not necessarily dictate that a grain will exhibit large misorientation after a significant number of cycles. This observation could imply that it may be difficult to predict which grain will experience a detrimental state leading to a failure mode such as crack initiation by only measuring the orientation heterogeneity at an early stage of a sample's life.

BIBLIOGRAPHY

[1] Amit Acharya, J. L. Bassani, and A. Beaudoin. Geometrically necessary dislocations, hardening, and a simple gradient theory of crystal plasticity. *Scripta Materialia*, 48(2):167–172, 2003.

[2] J Als-Nielsen McMorrow, Des.,. *Elements of modern X-ray physics*. Wiley, Hoboken, 2011.

[3] D.H Avery and W.A Backofen. Fatigue hardening in alloys of low stacking-fault energy. *Acta Metallurgica*, 11(7):653 – 661, 1963. ¡ce:title¿Mechanisms of fatigue in crystalline solids ¡/ce:title¿.

[4] Ma Bao-Tong and C. Laird. Overview of fatigue behavior in copper single crystals-II. Population, size distribution and growth kinetics of Stage I cracks for tests at constant strain amplitude. *Acta Metallurgica*, 37(2):337–348, 1989.

[5] S J Basinski, Z S Basinski, and A Howie. Early stages of fatigue in copper single crystals. *Philosophical Magazine*, 19(161):899–924, May 1969.

[6] Z S Basinski. Fundamental aspects of low amplitude cyclic deformation in face-centered cubic crystals. *Prog. Mater. Sci. (UK)*, 36(vi):89–148, 1992.

[7] Z S Basinski and S J Basinski. Fundamental aspects of low amplitude cyclic deformation in face-centred cubic crystals. *Prog. Mater. Sci. (UK)*, 36:89–148, 1992.

[8] Z. S. Basinski and S. J. Basinski. Surface-related phenomena in low amplitude fatigue of fcc metals. *Scripta Metallurgica et Materiala*, 26(10):1505–1510, 1992.

[9] Z S Basinski, R. Pascual, and S J Basinski. Low Amplitude Fatigue of Copper Single Crystals - 1. The Role of the Surface in Fatigue Failure. *Acta Metallurgica*, 31(4):591–602, 1983.

[10] Z. S. Basinski, R. Pascual, S. J. Basinski, S N S K R Pascual, and S. J. Basinski. Low amplitude fatigue of copper single crystals-I. The role of the surface in fatigue failure. *Acta Metallurgica*, 31(4):591–602, 1983.

[11] M Bayerlein and H Mughrabi. The Formation of Either Tongue- or Ribbon-Like Extrusions in Fatigued Copper Polycrystals. *Acta Metallurgia et Materialia*, 39(7):1645–1650, jul 1991.

[12] C. J. Bayley, W. A M Brekelmans, and M. G D Geers. A comparison of dislocation induced back stress formulations in strain gradient crystal plasticity. *International Journal of Solids and Structures*, 43(24):7268–7286, 2006.

[13] J V Bernier, N R Barton, U Lienert, and M P Miller. Far-field high-energy diffraction microscopy: a tool for intergranular orientation and strain analysis. *The Journal of Strain Analysis for Engineering Design*, 46(7):527–547, July 2011.

[14] T. R. Bieler, P. Eisenlohr, F. Roters, D. Kumar, D. E. Mason, M. A. Crimp, and D. Raabe. The role of heterogeneous deformation on damage nucleation at grain boundaries in single phase metals. *International Journal of Plasticity*, 25(9):1655–1683, sep 2009.

[15] Nicola Bonora, Domenico Gentile, A. Pirondi, and Golam Newaz. Ductile damage evolution under triaxial state of stress: Theory and experiments. *International Journal of Plasticity*, 21(5):981–1007, 2005.

[16] G. Cailletaud. A micromechanical approach to inelastic behaviour of metals. *International Journal of Plasticity*, 8(1):55 – 73, 1992.

[17] William D Callister , Rethwisch, David G.,. *Materials science and engineering : an introduction*. John Wiley & Sons, Hoboken, NJ, 2010.

[18] B D Cullity Stock, Stuart R.,. *Elements of x-ray diffraction*. Prentice Hall, Upper Saddle River, NJ, 2001.

[19] Paul R Dawson and Donald E Boyce. FEpX Finite Element Polycrystals Theory, Finite Element Formulation, Numerical Implementation and Illustrative Examples. *arXiv [cond-mat.mtrl-sci]*, pages 1–42, 2015.

[20] F. Delaire, J. L. Raphanel, and C. Rey. Plastic heterogeneities of a copper multicrystal deformed in uniaxial tension: Experimental study and finite element simulations. *Acta Materialia*, 48(5):1075–1087, 2000.

[21] B Devincre, T Hoc, and L Kubin. Dislocation Mean Free Paths and Strain Hardening of Crystals. *Science*, 320(5884):1745–1748, 2008.

[22] B. Devincre, L. Kubin, and T. Hoc. Physical analyses of crystal plasticity by DD simulations. *Scripta Materialia*, 54(5):741–746, 2006.

[23] J A Ewing and J C W Humfrey. The fracture of metals under repeated alternations of stress. *Proceedings of the Royal Society of London*, 71(467-476):79, 1902.

[24] J.M. Finney and C. Laird. Strain localization in cyclic deformation of copper single crystals. *Philosophical Magazine*, 31(2):339–366, 1975.

[25] P J E FORSYTH. Exudation of Material from Slip Bands at the Surface of Fatigued Crystals of an Aluminium-Copper Alloy. *Nature*, 171(4343):172–173, jan 1953.

[26] P Franciosi, M Berveiller, and A Zaoui. Latent Hardening in Copper and Aluminum Single-Crystals. *Acta Metallurgica*, 28(3):273–283, 1980.

[27] Jobie M. Gerken and Paul R. Dawson. A crystal plasticity model that incorporates stresses and strains due to slip gradients. *Journal of the Mechanics and Physics of Solids*, 56(4):1651–1672, 2008.

[28] Tong-Seok Han and Paul R Dawson. A two-scale deformation model for polycrystalline solids using a strongly-coupled finite element methodology. *Computer Methods in Applied Mechanics and Engineering*, 196(13-16):2029–2043, 2007.

[29] J R Hancock and J C Grosskreutz. Mechanisms of fatigue hardening in copper single crystals. *Acta Metallurgica*, 17(2):77–97, 1969.

[30] W F Hosford. *The Mechanics of Crystals and Textured Polycrystals*. Oxford Science Publications, 1993.

[31] William F Hosford. *The mechanics of crystals and textured polycrystals*. Oxford University Press, New York, 1993.

[32] A Hunsche and P Neumann. Quantitative measurement of persistent slip band profiles and crack initiation. *Acta metallurgica*, 34(2):207–217, 1986.

[33] B. Jakobsen, H.F. Poulsen, U. Lienert, X. Huang, and W. Pantleon. Investigation of the deformation structure in an aluminium magnesium alloy by high angular resolution three-dimensional X-ray diffraction. *Scripta Materialia*, 56(9):769–772, May 2007.

[34] A F Joffe and M V Kirpitcheva. XVIII. R{ö}ntgenograms of strained crystals. *Philosophical Magazine Series 6*, 43(253):204–206, 1922.

[35] K. Katagiri, A. Omura, K. Koyanagi, J. Awatani, T. Shiraishi, and H. Kaneshiro. Early Stage Crack Tip Dislocation Morphology in Fatigued Copper. *Metallurgical Transactions A (Physical Metallurgy and Materials Science)*, 8 A(11):1769–1773, 1977.

[36] K. Katagiri, A. Omura, K. Koyanagi, J. Awatani, T. Shiraishi, and H. Kaneshiro. Early stage crack tip dislocation morphology in fatigued copper. *Metallurgical Transactions A*, 8(11):1769–1773, 1977.

[37] D.S Kemsley and M.S Paterson. The influence of strain amplitude on the work hardening of copper crystals in alternating tension and compression. *Acta Metallurgica*, 8(7):453 – 467, 1960.

[38] Charles Kittel. *Introduction to Solid State Physics*. John Wiley and Sons, Inc., 2005.

[39] U. F. Kocks, P. Franciosi, and M. Kawai. A Forest Model of Latent Hardening and its Application to Polycrystal Deformations. *Textures and Microstructures*, 14(C):1103–1114, 1991.

[40] U F Kocks, Y Nakada, and B Ramaswami. Compression Testing of Fcc Crystals. *Transactions of the Metallurgical Society of Aime*, 230(5):1005–&, 1964.

[41] Mitsutoshi Kuroda and Viggo Tvergaard. On the formulations of higher-order strain gradient crystal plasticity models. *Journal of the Mechanics and Physics of Solids*, 56(4):1591–1608, 2008.

[42] Campbell Laird. The fatigue limits of metals. *Materials Science and Engineering*, 22:231–236, 1976.

[43] Campbell Laird. The fatigue limits of metals. *Materials Science and Engineering*, 22(C):231–236, jan 1976.

[44] E. M. Lauridsen, S Schmidt, R. M. Suter, and H F Poulsen. Tracking: a method for structural characterization of grains in powders or polycrystals. *Journal of Applied Crystallography*, 34(6):744–750, dec 2001.

[45] J H Lee, J Almer, C Aydıner, J Bernier, K Chapman, P Chupas, D Haeffner,

K Kump, P L Lee, U Lienert, A Miceli, and G Vera. Characterization and application of a GE amorphous silicon flat panel detector in a synchrotron light source. *Nuclear Instruments and Methods in Physics Research Section A: Accelerators, Spectrometers, Detectors and Associated Equipment*, 582(1):182–184, November 2007.

[46] U Lienert, M C Brandes, J V Bernier, J Weiss, S D Shastri, M J Mills, and M P Miller. In situ single-grain peak profile measurements on Ti–7Al during tensile deformation. *Materials Science and Engineering: A*, 524(1-2):46–54, October 2009.

[47] W Ludwig, P Reischig, a King, M Herbig, E M Lauridsen, G Johnson, T J Marrow, and J Y Buffière. Three-dimensional grain mapping by x-ray diffraction contrast tomography and the use of Friedel pairs in diffraction data analysis. *The Review of scientific instruments*, 80(3):033905, March 2009.

[48] P. Lukáš, M. Klesnil, and J. Krejčí. Dislocations and persistent slip bands in copper single crystals fatigued at low stress amplitude. *physica status solidi (b)*, 27(2):545–558, 1968.

[49] P. Lukáš and L. Kunz. Role of persistent slip bands in fatigue. *Philosophical Magazine*, 84(3-5):317–330, 2004.

[50] E B Marin and P R Dawson. Elastoplastic finite element analyses of metal deformations using polycrystal constitutive models. *Computer methods in applied mechanics and and engineering*, 7825(98), 1998.

[51] E B Marin and P R Dawson. On modelling the elasto-viscoplastic response of metals using polycrystal plasticity. *Computer methods in applied mechanics and and engineering*, 7825(98), 1998.

[52] D.L. McDowell. Experimental study of the structure of constitutive equations for nonproportional cyclic plasticity. *Journal of Engineering Materials and Technology, Transactions of the ASME*, 107(4):307 – 315, 1985.

[53] D.L. McDowell. Two surface model for transient nonproportional cyclic plasticity: Part 1. development of appropriate equations. pages ASME, New York, NY, USA; ASCE, New York, NY, USA –, Albuquerque, NM, USA, 1985.

[54] M P Miller, R M Suter, U Lienert, A J Beaudoin, E Fontes, and J C Schuren. High-energy needs and capabilities to study multiscale phenomena in crystalline materials. *Synchrotron Radiation News*, 25(6):18–26, 2012.

[55] N F Mott. A theory of the origin of fatigue cracks. *Acta Metallurgica*, 6(3):195–197, March 1958.

[56] H Mughrabi. The Cyclic Hardening and Saturation Behaviour of Copper Single Crystals. *Mater.Sci.Eng*, 33(2):207–223, may 1978.

[57] H. Mughrabi. Dislocation wall and cell structures and long-range internal stresses in deformed metal crystals. *Acta Metallurgica*, 31(9):1367–1379, 1983.

[58] P. Neumann. Coarse Slip Model of Fatigue. *Acta Metallurgica*, 17(9):1219–1225, 1969.

[59] J F Nye. Some geometrical relations in dislocated crystals. *Acta Metallurgica*, 1(2):153–162, 1953.

[60] Mark Obstalecki, Su Leen Wong, Paul R. Dawson, and Matthew P. Miller. Quantitative analysis of crystal scale deformation heterogeneity during cyclic plasticity using high-energy X-ray diffraction and finite-element simulation. *Acta Materialia*, 75:259–272, aug 2014.

[61] Jette Oddershede, Sø ren Schmidt, Henning Friis Poulsen, Henning Osholm Sø rensen, Jonathan Wright, and Walter Reimers. Determining grain resolved stresses in polycrystalline materials using three-dimensional X-ray diffraction. *Journal of Applied Crystallography*, 43(3):539–549, April 2010.

[62] Darren C. Pagan and Matthew P. Miller. Connecting Heterogeneous Single Slip to Diffraction Peak Evolution in High-Energy Monochromatic X-Ray Experiments. *Journal of Applied Crystallography*, 47(3):887–898, jun 2014.

[63] Darren C Pagan and Matthew P Miller. Determining heterogeneous slip activity on multiple slip systems from single crystal orientation pole figures. *Acta Materialia*, 116:200–211, 2016.

[64] W. Pantleon, H.F. Poulsen, J. Almer, and U. Lienert. In situ X-ray peak shape analysis of embedded individual grains during plastic deformation of metals. *Materials Science and Engineering: A*, 387-389:339–342, December 2004.

[65] Henning Friis. Poulsen. Three-dimensional X-ray diffraction microscopy mapping polycrystals and their dynamics, 2004.

[66] R. Quey. Neper, March 2014.

[67] R. Quey, P.R. Dawson, and F. Barbe. Large-scale 3D random polycrystals for the finite element method: Generation, meshing and remeshing. *Computer Methods in Applied Mechanics and Engineering*, 200(17-20):1729–1745, April 2011.

[68] R. Quey, J. H. Driver, and P. R. Dawson. Intra-grain orientation distributions in hot-deformed aluminium: Orientation dependence and relation to deformation mechanisms. *Journal of the Mechanics and Physics of Solids*, 84:506–527, 2015.

[69] J.R. Rice and D.M. Tracey. On the ductile enlargement of voids in triaxial stress fields. *Journal of the Mechanics and Physics of Solids*, 17(3):201–217, 1969.

[70] J. Schuren and M. P. Miller. Quantifying the uncertainty of synchrotron-based lattice strain measurements. *The Journal of Strain Analysis for Engineering Design*, 46(7):663–681, 2011.

[71] S Suresh. *Fatigue of Materials*. Cambridge University Press, Cambridge, U.K., second edition, 1998.

[72] R M Suter Hennessy, D, Xiao, C, Lienert, U,. Forward modeling method for microstructure reconstruction using x-ray diffraction microscopy: Single-crystal verification. *Review of scientific instruments.*, 77(12):123905, 2006.

[73] N Thompson, N Wadsworth, and N Louat. Xi. The origin of fatigue fracture in copper. *Philosophical Magazine*, 1(2):113–126, February 1956.

[74] H. S. Turkmen, M. P. Miller, P. R. Dawson, and J. C. Moosbrugger. A Slip-Based Model for Strength Evolution During Cyclic Loading. *Journal of Engineering Materials and Technology*, 126(4):329, 2004.

[75] T. Ungár, H. Biermann, and H. Mughrabi. Dislocation distributions as seen by X-ray line profiles. *Materials Science and Engineering A*, 164(1-2):175–179, 1993.

[76] T Ungar, O Castelnau, G Ribárik, M Drakopoulos, J L Béchade, T Chauveau, A Snigirev, I Snigireva, C Schroer, and B Bacroix. Grain to grain slip activity in plastically deformed Zr determined by X-ray micro-diffraction line profile analysis. *Acta Materialia*, 55(3):1117–1127, 2007.

[77] T Ungar, M G Glavicic, L Balogh, K Nyilas, A A Salem, G Ribárik, and S L Semiatin. The use of X-ray diffraction to determine slip and twinning activity in commercial-purity (CP) titanium. *Materials Science and Engineering: A*, 493(1–2):79–85, 2008.

[78] T Ungar, H Mughrabi, D Ronnpagel, and M Wilkens. X-ray line-broadening study of the dislocation cell structure in deformed [001]-orientated copper single crystals. *Acta Metall. (USA)*, 32(3):333–342, 1984.

[79] T Ungar, G Ribárik, G Zilahi, R Mulay, U Lienert, L Balogh, and S Agnew. Slip systems and dislocation densities in individual grains of polycrystalline aggregates of plastically deformed CoTi and CoZr alloys. *Acta Materialia*, 71(0):264–282, 2014.

[80] N.J Wadsworth. Work hardening of copper crystals under cyclic straining. *Acta Metallurgica*, 11(7):663 – 673, 1963.

[81] M Wilkens. The determination of density and distribution of dislocations in deformed single crystals from broadened x-ray diffraction. *Physical Status Solidi (A)*, 2:359–370, 1970.

[82] M Wilkens, K Herz, and H Mughrabi. An X-Ray Diffraction Study of Cyclically and of Unidirectionally Deformed Copper Single Crystals. *Zeitschrift für Metallkunde*, 71(6):376–384, jun 1980.

[83] M Wilkens, K Herz, and H Mughrabi. An X-Ray Diffraction Study of Cyclically and of Unidirectionally Deformed Copper Single Crystals. *Zeitschrift fur Metallkunde*, 71(6):376–384, June 1980.

[84] M Wilkens, T Ungár, and H Mughrabi. X-ray rocking-curve broadening of tensile-deformed [001]-orientated copper single crystals. *physica status solidi (a)*, 104(1):157–170, 1987.

[85] Su Leen Wong, Mark Obstalecki, Matthew P. Miller, and Paul R. Dawson. Stress and deformation heterogeneity in individual grains within polycrystals subjected to fully reversed cyclic loading. *Journal of the Mechanics and Physics of Solids*, 79:157–185, 2015.

[86] Su Leen Wong, Jun-Sang Park, Matthew P Miller, and Paul R Dawson. A framework for generating synthetic diffraction images from deforming polycrystals using crystal-based finite element formulations. *Computational Materials Science*, 77:456–466, September 2013.

[87] Su Leen Wong, Jun-Sang Park, Matthew P. Miller, and Paul R. Dawson. A framework for generating synthetic diffraction images from deforming polycrystals using crystal-based finite element formulations. *Computational Materials Science*, 77:456–466, 2013.

[88] W A Wood. Formation of fatigue cracks. *Philosophical Magazine*, 3(31):692–699, July 1958.

[89] W A Wood. Some basic studies of fatigue in metals, Fracture. In Hahn Thomas Averbach Felbeck, editor, *Technology Press of MIT*, page 412. MIT Technology Press, 1959.

[90] W. A. Wood, S. M. K. Cousland, and K. R. Sargant. Systematic microstructural changes peculiar to fatigue deformation. *Acta Metallurgica*, 11(7):643–652, 1963.

[91] T Y Wu, J L Bassani, and C Laird. Latent Hardening In Single-Crystals .1. Theory And Experiments. *Proceedings Of The Royal Society Of London Series A-Mathematical Physical And Engineering Sciences*, 435(1893):1–19, 1991.